The Pennsylvania State University
The Graduate School

HIGH-ENERGY NEUTRINO TRANSIENTS AS A PROBE OF NEUTRINO PHYSICS

A Dissertation in
Physics
by
Jose Alonso Carpio Dumler

Submitted in Partial Fulfillment
of the Requirements
for the Degree of

Doctor of Philosophy

August 2023

The dissertation of Jose Alonso Carpio Dumler was reviewed and approved by the following:

Kohta Murase
Associate Professor of Physics and Astronomy & Astrophysics
Dissertation Advisor
Chair of Committee

Peter Mészáros
Eberly Family Chair Professor, Emeritus

Luiz de Viveiros
Assistant Professor of Physics

Doug Cowen
Professor of Physics

Nitin Samarth
George A. and Margaret M. Downsbrough Department Head
Professor of Physics

Abstract

In this dissertation, we will look at neutrino production in astrophysical environments and how we can use these environments to probe neutrino physics. Neutrinos carry information about the particle physics processes occurring inside the source. As these neutrinos have energies much larger than those from terrestrial sources and travel cosmological distances to reach us, they can also be used to look for new physics.

We look at neutrino production in gamma-ray bursts and magnetars in a semi-analytical way. In both cases, we explore the source parameters that favor neutrino production and its implications for IceCube and future neutrino detectors. Then, we present the neutrino time delay approach to explore Beyond Standard Model interactions. This technique is suitable in multimessenger astrophysics, where we can measure neutrino delay with respect to a photon signal. We look at the time delay distributions obtained from Monte Carlo simulations, which can then be used for statistical analyses. We show an application of this technique in the context of supernova neutrinos and neutrino-dark matter interactions.

Table of Contents

List of Figures

List of Tables

Acknowledgments

Reaching this stage in my life is the culmination of years of study and sacrifice. When I got my Masters degree, I held back on the acknowledgments as my true goal was to obtain the Doctoral degree. At long last, I can properly recognize the impact that so many people have had on my life and how they shaped who I am today.

It goes without saying that my parents have provided tremendous support throughout the years, allowing me to pursue my dream of physics. At the same time, the sacrifices they made to ensure I had all the options available to me is beyond admirable. I can only hope that one day I will be able to pay them back for everything they have done for me. My brother Adolfo and my sister Sandra have always been attentive of my career path. They are very understanding when I appear visibly stressed due to hard times at work. The same applies to my brother-in-law Nino and sister-in-law Karem who care for me as if I were their own sibling. My uncle Francis, a great role model, and my amazing tía Debra have cheered me on during my PhD and I am very excited that my new workplace will be closer to California. I consider myself very lucky to be part of such a supportive family.

There are several professors, teacher and mentors that have motivated me and provided support when necessary to achieve my goal of becoming a physicist. For starters, my interest in physics began in high school. My physics classes with Steve Fagan were instrumental in cementing the basics of science and getting into the mindset that physics is more about thinking and less about memorizing. He kept believing in me and has followed my academic progress every step of the way. I always look forward to having a beer with him in Perú and share my experiences. During my last years in high school, I got to thoroughly enjoy mathematics with Luis Sánchez, who showed me the wonders of abstract algebra and gave me a glimpse of the mathematical tools used by physicists. By the time I was sixteen years old, I had decided to pursue physics as a career. To this day, I have not looked back.

When I started college, I was not entirely sure which field of physics I wanted to study. This changed after taking the particle physics course with Alberto Gago. I will always remember when he gave the students the Feynman rules for quantum electrodynamics to compute interaction cross sections. In the back of my head, I asked myself why these factors made physical sense. While trying to satisfy my own curiosity, I was driven to join Alberto's research group, where I started doing neutrino physics and astrophysics. During this time, I learned more about the Standard Model of particle physics, the basics

of quantum field theory and astroparticle physics. I then learned more about two of his students at the time: Carlos Argüelles and Mauricio Bustamante. To this day I continue to regard them as role models and I am truly grateful for the advice they have given me over the years. I also want to extend my gratitude to Francis Halzen, Carlos, Donglian Xu and Ali Kheirandish for the assistance they provided during my visit at UW Madison.

While doing my PhD at Penn State, I met lots of people that I could connect with at a professional level. Naturally, one of them is my advisor, Kohta Murase, who I have worked with since joining Penn State in 2017. He has provided me substantial advice on how to proceed with my career and actions I could take to increase my success chances for a postdoctoral position. I would also like to thank the (then) postdocs Mukul and Ali for their mentor roles during the program. From them, I have received very useful advice on manuscript writing, postdoc applications and life as a postdoc. Thanks to them, I am prepared to move to the next stage in my career. I am grateful to my other collaborators Sajad Abbar, Mary Hall Reno, Ina Sarcevic, Anna Stasto, Zahra Tabrizi, Ian Shoemaker, Nick Ekanger and Shunsaku Horiuchi for their contributions to our research projects.

It is also pertinent to thank the committee members Peter Mészáros, Doug Cowen and Luiz de Viveiros for all their feedback during the dissertation process and suggestions for postdoc applications. In particular, I truly appreciate Dr. de Viveiros' detailed feedback on the dissertation draft. I am grateful to Radu Roiban for teaching me so much about quantum field theory, significantly strengthening my particle physics knowledge. Furthermore, I want to express my deep appreciation for all the help provided by staff members Melissa, Juli and Karin. Sometimes it is difficult to navigate through paperwork and administrative procedures, but they were always willing to help me out. Whenever I had a question, I received valuable information and advice from them via email communications.

Beyond my academic growth, I want to acknowledge the people who have provided emotional support and express my appreciation for the cherished friends I have made throughout my life who helped me grow as a person. My greatest high school friends Carola and Sebastian, who have seen me through all the highs and lows of my adult life, have helped me out greatly during the first years in college. I remember with fondness how Sebastian and I hanged out during my last year of high school. It is always great to talk to Carola and catch up on what we've been doing. She is one of the few people I can talk to without feeling judged. I also want to mention my college friends Elmer, Sandro, Alfredo, Roberto, Eduardo, Pamela and Dante for the great times we had. I'm very comfortable sharing my struggles with Elmer because we share similar viewpoints. The times that Sandro, Elmer, Dante and I have shared during the undergrad and beyond are moments that I treasure very much. Being such a great motivator, Eduardo always knew what to say when I didn't feel well and helped me a lot during training.

I'm very grateful for the time we've spent connecting on a personal level and for them to accept me as a friend despite my character flaws. I am truly blessed to have these dear friends in my life. Even though we have all grown up and went our separate ways to pursue our own goals, I always keep you in my thoughts and look forward to the next time we get to meet, whether it is during vacations, travel or online. Your absence was

overwhelming during the pandemic and I'm glad I got to see some of you during my summer 2022 tour through Europe.

During my studies, I had the privilege of making valuable friends within my year group with whom I shared a lot of my struggles during my doctoral studies. These include my fellow physicists and friends Wilson, Tyler, Jackson, Kallan, Meghan, Nathan, Arnab, Neev, Ish and Aviral. Wilson has helped me to be less introverted and his cheerfulness is always appreciated, specially during stressful moments. Tyler is very approachable and his commitment to his values is commendable. His advice in troubling times helps me think outside the box.

Outside the friends I made in the Physics department, I also want to thank James and Laura for their support. Their friendship, trustworthiness and reliability are very hard to come by. I am glad to have met María, Camila, Samira, Juliana and Wouter during the last years of the program. The time I have spent with them is invaluable and hopefully we will keep in contact after I leave State College. María's stories are the best and talking to Camila and Juliana always brightens up my day.

During my last years in the PhD program, as the pandemic subsided, I could attend more conferences, visit more institutions and meet new people. In particular, I met fellow PhD students Po-Wen Chang, Nick Ekanger and Varun Mathur who I keep in contact with. Hopefully we will continue having both scientific and non-scientific discussions in the future.

Some of the people that I have mentioned here are sadly no longer with us. I am sorry that I could not reach my goal fast enough for you to be able to share this moment with me. I know how much you were looking forward to this moment. However, I have not forgotten about you and continue to live on in my memories.

Once again, to all the people mentioned here, from the bottom of my heart, thank you! As I move on to the next stage in my career, it would be my pleasure to share my future experiences with you all.

The work presented here has been supported by the Fermi GI program 111180. It was also supported by NSF Grant No. AST-1908689 and No. AST-2108466. The findings and conclusions in this work do not necessarily reflect the view of the funding agencies.

Chapter 1
Introduction

1.1 Neutrino physics

The Standard Model (SM) of particle physics is the theory that describes three of the fundamental forces: electromagnetic, weak and strong interactions. These forces are described in the context of quantum field theory, arising from the local SU(3) $\times$ SU(2) $\times$U(1) gauge symmetry. Among the fundamental particles that form the SM, the neutrino holds a special place as the only fermion with zero electric charge. Neutrinos are only allowed to interact via the weak force and as such they are known to interact very weakly with ordinary matter. Furthermore, SM neutrinos are purely left-handed (antineutrinos are purely right-handed) and massless.

The neutrino was first hypothesized by Wolfgang Pauli in 1930, as a way to explain beta decay, where a neutron seemingly decays into a proton and an electron. Per the kinematics of two-body decays, the electron would always come out carrying the same energy, but experimental observations clearly showed that the electrons were not monoenergetic. This obvious violation of energy conservation could be avoided if a third particle carried away the missing energy. The first evidence for the neutrino was not observed until 1956, as they were so weakly interacting. The neutrino family, consisting of ν_e, ν_μ and ν_τ was finally completed by the DONUT experiment in 2000.

Neutrino physics has made significant progress since its initial discovery. Originally believed to be massless, it was even built as such in the SM. In 1957/1958 Bruno Pontecorvo first proposed the idea that neutrinos could oscillate into antineutrinos, inspired by the $K^0 \rightleftharpoons \overline{K}^0$ oscillations proposed by Gell-Mann and Pais one year prior [33]. Pontecorvo's second paper in 1967 introduced the possibility of neutrino oscillations between different flavors, provided that they had mass and lepton number was not a conserved quantity [34]. He also predicted that the observed solar neutrino flux would

be smaller than the theoretical prediction. This so-called "solar neutrino problem" was confirmed in 1970.

Definitive proof for neutrino oscillations was obtained by the Super-Kamiokande detector in 1998 [35] and the Sudbury Neutrino Observatory in 2001 [36]. The discovery implies that neutrinos have mass, which is clear evidence that they exhibit Beyond Standard Model (BSM) behavior. At this point in time, we are in the precision era, where we progressively narrow down the values of the oscillation parameters. In the future, next-generation neutrino experiments such as DUNE and Hyper-Kamiokande (HK) will continue to improve on the current status of oscillation measurements, particularly the measurement of the CP-violation phase and determining the neutrino mass hierarchy [37].

1.2 Astrophysical neutrinos and multimessenger astronomy

Neutrinos can be produced on Earth via radioactive decays, such as reactor neutrinos or geoneutrinos. We can also use particle accelerators to force collisions between protons and nuclei to create pions, which subsequently decay into neutrinos. These neutrino sources have limited energies, as they do not go past a few tens of GeV. Atmospheric neutrinos, created from cosmic ray air showers in the atmosphere, reach higher energies, up to $\mathcal{O}$ (10) TeV. However, the atmospheric neutrino flux is known to fall steeply with neutrino energy. These neutrino fluxes are shown in Fig. 1.1.

We can look at even more energetic neutrinos by looking at faraway sources. Our closest source of extraterrestrial neutrinos is the Sun. They are produced in the Sun's core as a result of nuclear fusion processes. These neutrinos peak in the $\mathcal{O}(100)$ keV range and then quickly decrease with energy, extending to $\sim$ 10 MeV. Besides solar neutrinos, the supernova explosion SN1987A became the first event which showed coincident photon and neutrino emissions, the latter being in the $\sim$ 10 MeV range [38, 39].

Extreme astrophysical environments provide the strongest particle accelerators, able to accelerate cosmic rays up to $\sim 10^{20}$ eV, as observed by the Pierre Auger Observatory and the Telescope Array. Some examples of these environments include gamma-ray bursts (GRBs), active galactic nuclei (AGNs) and magnetars. Similar to terrestrial experiments, we expect these nuclei to create pions via interactions with their environments, leading to high-energy neutrino production. Within these sources, neutrinos can be produced with energies up to $\sim$ 10 PeV. At these high energies, these neutrinos are essentially

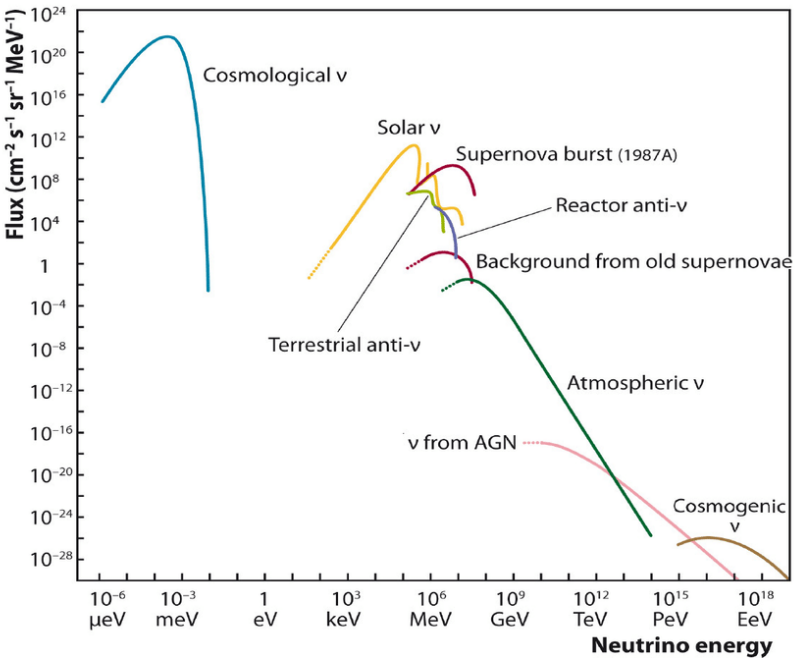

Figure 1.1. Measured and expected neutrino fluxes from various sources as a function of neutrino energy.

background free as they overtake the atmospheric neutrino flux. However, the flux is quite low and thus requires ~ 1 km^3 detectors to observe.

The discovery of these high-energy astrophysical neutrinos by the IceCube detector [40, 41] ushered the era of neutrino astronomy. The result of a recent analysis using six years of cascade data is shown in Fig. 1.2. Here, we observe that the atmospheric neutrino events, which is the sum of the expected conventional and prompt neutrino neutrino events shown in the figure, is insufficient to explain the neutrino events above $\sim$ 30 TeV. The diffuse flux, the cumulative contribution from all neutrino sources, appears largely isotropic, evenly distributed between the three neutrino flavors, and its energy spectrum is well-described by a power law from $\sim$ 10 TeV up to PeV energies [1,10,42,43]. The actual origin of these neutrinos remains unresolved. The observation of the neutrino event IceCube-170922A coincident with the flaring blazar TXS 0506+056 [44] provided us with an example of multimessenger observations triggered by a neutrino observation [45]. There is also correlation of IceCube neutrinos with a catalog of gamma-ray emitters, with a significance of 3.3σ [46]. One of these emitters, the nearby active galaxy NGC1068, provided the first direct evidence of an AGN as a neutrino source at a significance of 4.2σ [47].

Astrophysical neutrinos provide unique opportunities to study sources that are

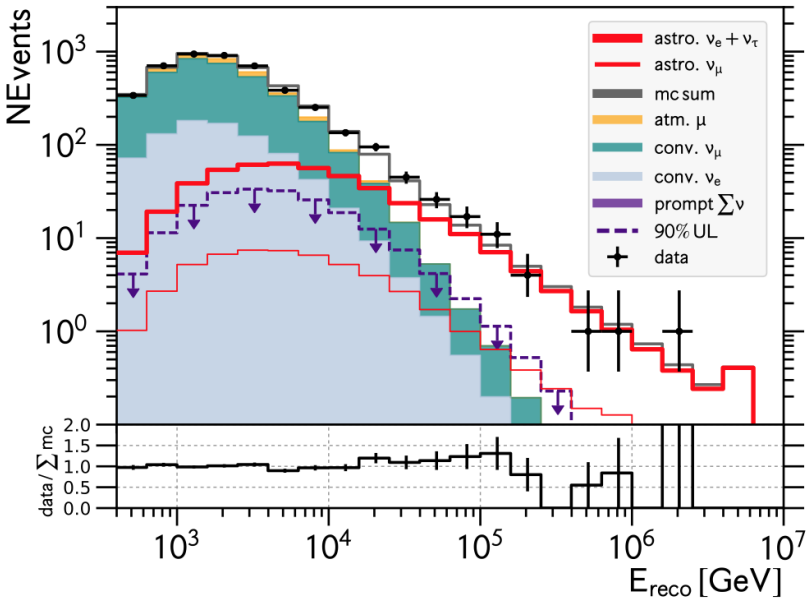

Figure 1.2. Number of neutrino events in IceCube as a function of reconstructed cascade energy, as shown in [1]. The dataset consists of neutrinos with reconstructed energies above 400 GeV that were collected in 2010-2015. The Monte Carlo event distribution from the sum of all neutrino fluxes is shown as a solid gray histogram.

otherwise invisible in the electromagnetic spectrum, or behave differently at certain wavelengths. Neutrinos and gamma-rays are expected to be emitted in tandem from meson decays, with comparable luminosities. In the case of NGC1068, its neutrino luminosity is found to be significantly higher than its gamma-ray luminosity as measured by Fermi-LAT [47], which shows that this source has to be gamma-ray opaque. This information can then be used to better understand the source (e.g. [48]).

Neutrinos also serve as one of the astrophysical messengers, together with cosmic rays, photons and gravitational waves. The case of NGC1068 is an example of the use of photons and neutrinos. The use of two or more of these messengers is the principle of multimessenger astronomy.

Each messenger possesses its own strengths and drawbacks. Cosmic rays are able to be detected at extremely high energies, but the highest energy cosmic rays must be within ~ 50 Mpc due to attenuation with the cosmic microwave background (CMB). As they are charged particles, they get deflected by the Galactic magnetic field and will not point back to its original source. This makes the other three messengers better at locating sources. Photons interact electromagnetically, so they can be attenuated in the interstellar medium by dust, the extragalactic background light and the CMB. The

latter two place a gamma-ray horizon of ~ 10 Mpc for photons above 1 TeV. However, they have the best angular resolution among all the messengers. Gravitational waves have angular resolution of tens of square degrees and their horizon is mostly set by the detector's sensitivity.

In the case of neutrinos, the main source of attenuation would be the cosmic neutrino background (CνB). However, the very small weak-scattering cross section makes the Universe essentially transparent to neutrinos. Their weak interaction with ordinary matter also means that they carry information from deep within the source. The limitation of this particle is that only ν_μ, which produce muon tracks in the detector, have a moderate angular resolution of a few degrees. At the same time, the small cross section also means that the neutrino source has to be nearby and highly luminous to detect a few events.

1.3 Neutrino physics as a probe of Beyond Standard Model physics

We showed that astrophysical neutrinos can be used as studying tools of their sources. Applications of this kind mostly focus on the astrophysical side. A natural question is if they can also be used for particle physics purposes, as they probe an energy scale that is not accessible by terrestrial neutrino sources.

The IceCube Collaboration reported in 2021 that one of its cascade events was created as a result of the Glashow resonance [43]. This resonance consists of the on-shell production of the 80 GeV W^- boson via $e^-\bar{\nu}_e$ annihilation. For an electron at rest, this requires a 6.7 PeV $\bar{\nu}_e$. An event of this kind is important as it provides further validation of the SM. As neutrinos contain BSM physics by virtue of their mass, it is natural to also study BSM models that can be tested with high-energy neutrinos.

The most immediate issue is generating a mass for the neutrino. In the SM, fermion masses are generated through Yukawa couplings with the Higgs doublet (after electroweak spontaneous symmetry breaking), which requires the presence of right handed fermion fields. On top of this, we also want to explain why neutrinos are so light compared to their charged lepton counterparts; this disparity between masses is not seen in the quark sector. Several types of seesaw mechanisms have been proposed as phenomenological explanations for the smallness of the neutrino mass, but generally require a new physics scale, mostly through the introduction of a very heavy right-handed neutrino.

We also do not know whether the active neutrinos are Dirac or Majorana fermions,

and the neutrino is the only elementary particle that may be a Majorana fermion, which motivates the construction of next generation double beta decay experiments such as nEXO [49]. In the neutrino oscillation front, the LSND experiment claimed a $\bar{\nu}_e$ excess over the expected background, which provided a hint towards a sterile neutrino which does not interact via the weak force [50]. This so-called LSND anomaly was further reinforced by the MiniBooNE experiment at Fermilab, which found a 4.7σ excess of events in ν_e and $\bar{\nu}_e$ channels [51]. Moreover, it turns out that both of these anomalies cannot be simulatenously explained by a 3 active + 1 sterile neutrino scenario.

While several models have been presented to tackle the problems presented above, this thesis will focus on the class known as neutrino self-interactions (νSI), also known as secret neutrino interactions. In this class of models, new mediators allow neutrino-neutrino couplings beyond the weak force. Laboratory limits on these models rely mostly on meson-decay experiments [22] and allows for νSI to have large effects. The introduction of a new mediator allows for modifications of the neutrino oscillations in matter [52] and enable sterile neutrino decays [53, 54], which can potentially explain the short baseline neutrino anomalies. Vector mediators can explain the muon $g-2$ anomaly [55] by introducing additional Feynman diagrams contributing to the calculation of the anomalous magnetic moment via the gauged $L_\mu - L_\tau$ model [56–59]. The νSI model has deep implications in cosmology, due to its ability to alter the CMB power spectrum, providing limits on the model parameters [22, 60–62].

Astrophysical neutrinos can be used to study νSI through their effect on the diffuse neutrino flux. As neutrinos propagate from the source to the observer, they will move through the CνB. Although the weak interaction cross section would normally be too small for high-energy neutrinos to interact, new physics can change this. A way to create a significant impact on the $\nu - \nu$ cross section is to produce new particles via resonances. In resonant interactions, the cross section spikes, which would create significant neutrino attenuation at energies close to resonance. This has been applied in the context of IceCube in several studies [63–67].

Another approach we can take is to study neutrino interactions with dark matter (DM). DM is clear evidence that the particle content of the Universe is not fully known. Despite the overwhelming evidence for its, such as Galaxy rotation curves [68, 69] and gravitational lensing [70–73], its particle nature remains unknown [74, 75]. Weakly Interacting Massive Particles (WIMPs) are one of the most studied DM candidates and direct and indirect DM searches have extensively probed the WIMP parameter space. Stringent limits on DM exist via WIMP interactions with SM particles as well as DM

decay or annihilation to SM particles. Direct-detection searches have not found evidence for WIMPs [76–78], but are not sensitive to DM masses below 10 GeV. On the other hand, DM phase-space distribution in dwarf spheroidal galaxies suggests a lower bound for fermionic DM mass of $\sim$ 1 keV, while the mass range of 1 keV – 1 MeV remains poorly constrained. Within this mass range, keV sterile neutrinos may be a suitable DM candidate via the seesaw mechanism [79–81].

Neutrino couplings to dark matter can also be used to shed some light on the nature of DM, as such a model allows both νSI and DM self-interactions to take place. DM self-interactions [82–87] were introduced to alleviate problems with the standard cosmological model, such as the "too big too fail" problem [88] and the "missing satellite" problem [89, 90]. Neutrino-DM interaction has been extensively considered in cosmology context [91–103]. In addition, an ongoing neutrino-DM scattering would damp the power spectrum of primordial fluctuations (see e.g. [100]). Observation of high-energy cosmic neutrinos provided further power to probe for DM-neutrino interaction [40, 41]. Neutrino-DM interactions were studied in this context [65, 104–106], which bestowed competitive limits with cosmological studies. These searches utilize features induced by DM-neutrino interaction in energy spectrum [65], energy spectrum and arrival direction [104], and arrival time [106] of high-energy cosmic neutrinos. The latter has become possible with recent progress in identification of coincident high-energy neutrinos with transient astrophysical phenomena [107, 108].

In order to probe BSM interactions, we also want to exploit multimessenger astronomy to extract more information. One of the most recent examples is GRB221009A, which has the brightest observed prompt emission, located at redshift $z = 0.15$ and isotropic-equivalent energy of $E_{\rm iso} \sim 10^{54}$ erg [109]. Even more striking is that LHAASO observed gamma-rays up to 10 TeV in energy, which should not happen due to photon attenuation through $e^+ - e^-$ pair production. Among the several explanations that were proposed, we focus on the ones involving neutrinos. For example, sterile neutrinos produced at the source can decay into photons via the neutrino magnetic moment [110, 111], or radiative decays into active neutrinos and photons [112]. Naturally, any of these explanations should also be consistent with IceCube's non-observation of neutrinos coincident with this GRB [113]. The ability to observe different particles and their arrival times will prove useful to our study of νSI.

1.4 Outline

In this dissertation I will present the results from my work on neutrino production in astrophysical environments. The neutrino sources considered are gamma-ray bursts and magnetars. In both cases, we will look at source parameters that favor neutrino production and its implications for IceCube and future neutrino detectors.

Afterwards, I will present the neutrino time delay approach to explore BSM interactions. As neutrinos propagate between source and observer, scatterings with other particles will naturally elongate the trajectory length. Even if the scattering angle is small, the large distances are enough to cause a measurable time delay between a scattered and unscattered neutrino. This technique is suitable in multimessenger astrophysics, where we can measure neutrino delay with respect to a photon signal. Time delay has been suggested as a method to constrain the cross section [106] by using the characteristic time delay of neutrinos at a given energy. We will expand on this by considering the time delay distribution for a given neutrino spectrum at the source, which can then be used to perform a detailed statistical analysis in neutrino experiments.

The thesis is structured as follows: in Chapter 2 we will go over the basic theoretical tools used in this work, such as neutrino oscillations and cosmological features relevant to neutrino propagation. Chapter 3 discusses neutrino production from cosmic rays and outline the particle interactions involved in the process. In chapter 4, we look at neutrino oscillations in choked GRB jets, based on [114]. In chapter 5, we look at neutrinos originating from charm production in magnetars, which constitutes the work done in [115]. We discuss a few BSM neutrino interaction models in chapter 6, which will be used in later chapters. We present the code I developed to simulate neutrino echoes in chapter 7, with applications to high-energy neutrino spectra [116]. In chapter 8 we introduce an application of this code in the context of neutrino-dark matter interactions, its effect on neutrino emission from supernovae and prospects for Hyper-Kamiokande [117].

Chapter 2
Theoretical Background

2.1 Introduction

In this section, we will discuss the theoretical tools used throughout the work. The purpose of this section is not to include extensive details of neutrino physics, instead focusing on the theory that is applied directly to this work, as well as a brief introduction of the concepts. Here we will also introduce terminology, parameters and notation frequently used throughout the discussion of neutrino secret interactions. First, we will briefly mention the role of neutrinos in the Standard Model, to then set up the stage for neutrino oscillations. The oscillation phenomenon is vital in particle propagation and will also play an important role in BSM interactions. As the bulk of this work deals with astrophysical neutrinos, we will encounter sources located at cosmological distances, which necessitates an introduction to the basics of Big Bang cosmology, namely expansion of the Universe and redshift.

Before discussing the theory, we will first point out the units used throughout this work. For the particle physics content, which includes field theory, Lagrangians, cross sections and neutrino oscillations, we use natural units, i.e. $\hbar = c = 1$. When an exception arises, the units will be shown explicitly. For Einstein summation, we adopt the Minkowski metric tensor $\eta^{\mu\nu} = \text{diag}(1, -1, -1, -1)$. The zeroth component of our four-vectors are our timelike components (e.g. time, energy).

For astrophysical parameters, such as luminosities or ejecta speeds we will use cgs units. When using cgs units, mostly in Section 3, we will often use the notation $Q_x = Q/10^x$, where Q is the parameter in question, in cgs units. The only exception to this rule is the mass of astrophysical objects, in which case we use $M_x = M/10^x M_\odot$.

2.2 Massless neutrinos in the Standard Model

Within the Standard Model of Particle Physics, we have three neutrinos: ν_e, ν_μ and ν_τ, each with its own antiparticle. They belong to the family of leptons, where the neutrinos are the neutral leptons, while the others are the charged leptons: e, μ and τ. Leptons are spin 1/2 fermions, where the charged leptons ℓ are known to be Dirac fermions, with free Lagrangian

$$\mathcal{L}_{\text{free}} = i\bar{\ell}\gamma^\mu\partial_\mu\ell - m_\ell\bar{\ell}\ell, \tag{2.1}$$

where m_ℓ is the lepton mass and γ^μ ($\mu = 0, 1, 2, 3$) are the gamma matrices, with the defining property $\{\gamma^\nu, \gamma^\nu\} = 2\eta^{\mu\nu}$. The first term in the Lagrangian is called the kinetic term and the second one the mass term. The important feature of spin 1/2 fermions is that we can introduce the chirality matrix $\gamma^5 = i\gamma^0\gamma^1\gamma^2\gamma^3$ and define

$$P_L = \frac{1}{2}(1 - \gamma^5) \qquad\qquad P_R = \frac{1}{2}(1 + \gamma^5), \tag{2.2}$$

where $P_L(P_R)$ is the left (right) chirality projection operator. For a given Dirac field Ψ, we can thus define the left-handed field $\Psi_L = P_L\Psi$ and the right-handed field $\Psi_R = P_R\Psi$. By splitting a field into its left and right components, we can write the free Lagrangian as

$$\mathcal{L}_{\text{free}} = i\overline{\ell_L}\gamma^\mu\partial_\mu\ell_L + i\overline{\ell_R}\gamma^\mu\partial_\mu\ell_R - m_\ell(\overline{\ell_R}\ell_L + \overline{\ell_L}\ell_R). \tag{2.3}$$

Due to the presence of γ^μ in the kinetic term, left-handed fields couple to left-handed fields and similarly for the right-handed fields. In the mass term, however, we see that the left-handed field couples to the right-handed field. This is relevant to neutrinos because, in the SM, neutrino fields are left-handed: we only have left-handed neutrinos and right-handed antineutrinos. Therefore, by construction, neutrinos are massless in the SM, even after electroweak symmetry breaking.

Neutrinos are unique fermions in the SM because they only interact via the weak force. Through the weak force, neutrinos may only couple to other leptons. Neutrino interactions with charged leptons are mediated by the W-boson, described by the charged-current (CC) interaction Lagrangian

$$\mathcal{L}_{\text{CC}} = -\frac{g_W}{2\sqrt{2}}\sum_{\ell=e,\mu,\tau}\overline{\nu_\ell}\gamma^\mu(1 - \gamma^5)\ell W_\mu + \text{h.c.}, \tag{2.4}$$

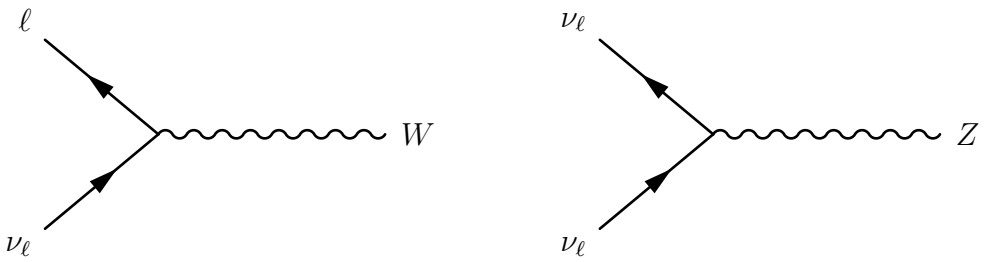

Figure 2.1. Left panel: CC vertex for neutrino interactions with charged leptons. Right panel: NC vertex for neutrino-neutrino interactions

where W_μ is the W-boson vector field and g_W is the coupling constant for the weak interaction. Similarly, neutrino interactions with other neutrinos are mediated by the Z-boson, described by the neutral-current (NC) interaction Lagrangian

$$\mathcal{L}_{\rm NC} = -\frac{g_W}{4\cos\theta_W}\sum_{\ell=e,\mu,\tau}\overline{\nu_\ell}\gamma^\mu(1-\gamma^5)\nu_\ell Z_\mu + \text{h.c.}, \tag{2.5}$$

where θ_W is the weak mixing angle. From these SM interactions, whose fundamental vertices are shown in Fig. 2.1, there are two important observations about these Lagrangians

1. The fundamental vertex does not allow couplings between different lepton families. For example, a CC vertex between ν_e and μ is forbidden.

2. The respective coupling strengths for CC and NC interactions are the same for all lepton generations.

Both of these arise from the way in which the SM is built. In general, couplings between different lepton generations are allowed in BSM models, with strengths constrained only through symmetries of the chosen model or experimental observations.

2.3 Vacuum Neutrino Oscillations

Here, we discuss the main aspects of neutrino oscillations in vacuum, which will be used for the purpose of neutrino propagation. For a more complete review, of this phenomenon, see for example [118] and references therein.

Nowadays, it is known that the neutrino flavor eigenstates, which are the ones involved in weak interactions, are not the same as the neutrino mass eigenstates, which have definite mass. Since neutrino production and detection necessarily use weak interactions, we can only make measurements on flavor eigenstates. From a quantum mechanical

perspective, the flavor eigenstates $|\nu_\alpha\rangle$ ($\alpha = e, \mu, \tau$) are related to the mass eigenstates $|\nu_i\rangle$ ($i = 1, 2, 3$) by the Pontecorvo-Maki-Nakagawa-Sakata (PMNS) matrix [119], also known as the neutrino mixing matrix U, which is unitary. Explicitly, a flavor eigenstate $|\nu_\alpha\rangle$ is written as

$$|\nu_\alpha\rangle = \sum_{k=1}^{3} U^*_{\alpha k} |\nu_k\rangle. \tag{2.6}$$

or, in matrix notation,

$$\begin{pmatrix} \nu_e \\ \nu_\mu \\ \nu_\tau \end{pmatrix} = \begin{pmatrix} U_{e1} & U_{e2} & U_{e3} \\ U_{\mu 1} & U_{\mu 2} & U_{\mu 3} \\ U_{\tau 1} & U_{\tau 2} & U_{\tau 3} \end{pmatrix} \begin{pmatrix} \nu_1 \\ \nu_2 \\ \nu_3 \end{pmatrix}. \tag{2.7}$$

The matrix notation will come in handy when switching neutrino fields in the Lagrangian between the mass and flavor basis.

Here we point out that we are assuming that only three neutrino generations exist, which are known as active because they interact via the weak force. It is possible that more neutrino states exist, that do not interact via the weak force and are known as sterile neutrinos, but this case is beyond the scope of this work. We adopt the standard parametrization of the PMNS matrix with three mixing angles ($\theta_{12}, \theta_{13}, \theta_{23}$) and one CP violation phase $\delta_{\rm CP}$

$$U = \begin{pmatrix} 1 & 0 & 0 \\ 0 & c_{23} & s_{23} \\ 0 & -s_{23} & c_{23} \end{pmatrix} \begin{pmatrix} c_{13} & 0 & s_{13} e^{-i\delta_{\rm CP}} \\ 0 & 1 & 0 \\ -s_{13} e^{i\delta_{\rm CP}} & 0 & c_{13} \end{pmatrix} \begin{pmatrix} c_{12} & s_{12} & 0 \\ -s_{12} & c_{12} & 0 \\ 0 & 0 & 1 \end{pmatrix}, \tag{2.8}$$

where $c_{ij} = \cos\theta_{ij}$ and $s_{ij} = \sin\theta_{ij}$. This PMNS matrix applies to Dirac neutrinos; if the active neutrinos were Majorana, we would multiply the right hand side of Eq. (2.8) by Diag$(e^{i\eta_1}, e^{i\eta_2}, 1)$ (multiplication from the right), where η_1 and η_2 are the Majorana phases.

Assuming that neutrinos are ultrarelativistic, the Hamiltonian for neutrino evolution in a vacuum is

$$H = \frac{M^2}{2E_\nu} \tag{2.9}$$

where E_ν is the neutrino energy, M^2 is the squared mass matrix (diagonal in the mass basis), and the momentum term is proportional to the identity and is not relevant in neutrino oscillations. The mass eigenstates $|\nu_k\rangle$ are eigenstates of H with eigenvalue $m_k^2/2E_\nu$. By solving the time-independent Shcrödinger equation to evolve our initial

Parameter	Best fit value
θ_{12}	33.44°
θ_{13}	8.57°
θ_{23}	49.0°
$\delta_{\rm CP}$	195°
Δm^2_{21}	7.42×10^{-5} eV^2
Δm^2_{31}	2.51×10^{-3} eV^2

Table 2.1. Best fit values of neutrino oscillation parameters that are will be used in this work, as reported in [29]. NO is assumed.

states, and using $t = l$ for ultrarelativistic neutrinos and a propagation distance l, the probability of a $\nu_\alpha \to \nu_\beta$ transition is (in natural units)

$$P(\nu_\alpha \to \nu_\beta) = |\langle \nu_\beta | e^{-iHt} | \nu_\alpha \rangle|^2 = \sum_{j,k} U^*_{\alpha k} U_{\beta k} U_{\alpha j} U^*_{\beta j} \exp\left(-i \frac{\Delta m^2_{kj} l}{2E_\nu}\right), \tag{2.10}$$

where $\Delta m^2_{kj} = m^2_k - m^2_j$ is the squared mass difference. This formula applies whether neutrinos are Dirac or Majorana. An alternative form of Eq. (2.10) is

$$P(\nu_\alpha \to \nu_\beta) = \sum_k |U_{\alpha k}|^2 |U_{\beta k}|^2 + 2\mathrm{Re} \sum_{k>j} U^*_{\alpha k} U_{\beta k} U_{\alpha j} U^*_{\beta j} \exp\left(-2\pi i \frac{l}{l^{\rm osc}_{kj}}\right), \tag{2.11}$$

where we have defined the oscillation lengths

$$l^{\rm osc}_{kj} = \frac{4\pi E_\nu}{\Delta m^2_{kj}} = 2.47 \frac{E_\nu[\mathrm{GeV}]}{|\Delta m^2_{kj}|[\mathrm{eV}^2]} \mathrm{km}. \tag{2.12}$$

The oscillation formula for antineutrinos can be obtained from Eq. (2.10) and replacing $U \to U^*$ or, alternatively, $\delta_{\rm CP} \to -\delta_{\rm CP}$.

From Eq. (2.11), we see that oscillation probabilities depend on squared mass differences, so this phenomenon does not provide information on the absolute neutrino mass. The mass eigenstates are labeled such that $m_1 > m_2$, but this leaves us with two possible mass orderings: the normal ordering (NO) $m_1 < m_2 < m_3$ and the inverted ordering (IO) $m_3 < m_1 < m_2$. With the latest neutrino oscillation experimental data, there is no significant preference for either ordering. For this dissertation, we will use the most recent global fit results under the NO assumption [29], which are summarized in Table 2.1.

It is important to point out that the oscillation phenomenon requires interference

between the mass eigenstates. The formulas above are derived under the plane wave approximation, where the wave extends over all of space, such that interference is always guaranteed. A more formal approach is to use the wave packet treatment (see e.g. [120]), where interference only occurs if the different wave packets, corresponding to different mass eigenstates, overlap. Since neutrino are massive, each mass eigenstate propagates at slightly different speeds, just under the speed of light. Given a sufficiently large propagation length, the separation between these wave packets will exceed the width of the packet, effectively killing all oscillations. For wave packets of size σ_x, there is a coherence length

$$l_{kj}^{\text{coh}} = \frac{4\sqrt{2}E^2}{|\Delta m_{kj}^2|}\sigma_x \tag{2.13}$$

beyond which the oscillation between ν_k and ν_j becomes suppressed. If we have $l \gg l_{kj}^{\text{coh}}$, then Eq. (2.11) becomes

$$P(\nu_\alpha \to \nu_\beta) = \sum_k |U_{\alpha k}|^2 |U_{\beta k}|^2, \tag{2.14}$$

describing the suppression known as wave packet decoherence. The formula above is simply a sum of the probability that ν_α propagates as ν_k and that ν_k is detected as ν_β. On the other hand, if $l \gg l_{kj}^{\text{osc}}$, then oscillations are averaged out and we would also arrive at Eq. (2.14).

2.4 Neutrino oscillations in matter

If neutrinos propagate through matter, the Hamiltonian has to be modified, leading to the Mikheyev-Smirnov-Wolfenstein (MSW) effect [121, 122]. Ordinary matter consists of protons, neutrons and electrons. All three neutrino flavors can scatter off electrons via NC interactions. However, electron neutrinos may also interact through CC interactions with ordinary matter. For these interactions, the typical energy scales involved are such that we may reduce the Hamiltonian to its effective low-energy expression. Furthermore, we will consider the case of coherent forward scattering, which allows us to treat the effect of the medium as an effective potential that is added to the vacuum Hamiltonian.

Working through the calculations, which are done in detail in [123] for example, one finds that the contributions from the NC potential depends on the number density of neutrons alone and is the same for all three neutrino flavors. If we were to add this potential to the Hamiltonian, it would be a 3×3 matrix proportional to the identity and

would only lead to global phase shifts on the neutrino states. On the other hand, the CC contribution does result in an observable effect on the oscillation pattern described by the Hamiltonian (in the vacuum mass eigenstate basis)

$$H = \frac{1}{2E_\nu}\begin{pmatrix} 0 & 0 & 0 \\ 0 & \Delta m^2_{21} & 0 \\ 0 & 0 & \Delta m^2_{31} \end{pmatrix} + \frac{1}{2E_\nu} U^\dagger \begin{pmatrix} A_{\rm CC} & 0 & 0 \\ 0 & 0 & 0 \\ 0 & 0 & 0 \end{pmatrix} U \tag{2.15}$$

where $A_{\rm CC} = 2\sqrt{2}E_\nu G_F n_e$, n_e is the electron number density, G_F is the Fermi constant and we have removed a term proportional to the identity in the mass term, corresponding to m^2_1. Notice that the overall expression for this Hamiltonian is still of the form $H = X/2E_\nu$ for some Hermitian matrix X. This means that the Hamiltonian can be diagonalised by some unitary matrix, different from the PMNS matrix U, which would require some new *effective* mixing angles and CP violating phase. The eigenvalues of the Hamiltonian will thus lead to three effective neutrino masses in matter and the oscillation probabilities can still be described by the formulas in the vacuum case, but substituting the oscillation parameters by its effective values. While this substitution works for a constant density profile, neutrinos generally will propagate through a variable density. In such cases, we resort to numerical methods to solve the time-dependent Hamiltonian given by Eq. (2.15), where the time dependence is implicit in n_e.

For illustrative purposes, it is worthwhile to highlight the main feature of neutrino oscillations in matter for two flavors. In the 2-flavor scenario, the only oscillation parameters are Δm^2 and a single mixing angle θ and we label the flavors ν_e and ν_x. The transition probability formula in this case is

$$P(\nu_e \to \nu_x) = \sin^2(2\theta_{\rm eff}) \sin^2\left(\frac{\Delta m^2_{\rm eff} D}{4E_\nu}\right). \tag{2.16}$$

When matter effects are considered, the effective squared-mass difference $\Delta m^2_{\rm eff}$ is given by

$$\Delta m^2_{\rm eff} = \sqrt{(\Delta m^2 \cos 2\theta - A_{\rm CC})^2 + (\Delta m^2 \sin 2\theta)^2)}, \tag{2.17}$$

while the effective mixing angle $\theta_{\rm eff}$ is determined by solving

$$\tan 2\theta_{\rm eff} = \frac{\tan 2\theta}{1 - \dfrac{A_{\rm CC}}{\Delta m^2 \cos 2\theta}}. \tag{2.18}$$

By looking at the equations above, we see that there is a resonance energy $E_{\nu,\rm res} =$

$\Delta m^2 \cos 2\theta / 2\sqrt{2} G_F n_e$ which minimizes Δm^2_{eff} and leads to $\theta_{\text{eff}} = \pi/4$, which implies maximal neutrino mixing.

In reality, astrophysical neutrinos will typically propagate through a progenitor, which has a non-constant density profile. If the density profile changes slowly, in the sense that θ_{eff} (now time-dependent) changes slowly as the neutrino propagates, then the adiabatic approximation may be used. Within this regime, each mass eigenstate in matter evolves independently, which leads to the survival probability

$$\begin{aligned} P(\nu_e \to \nu_e) &= \frac{1}{2} + \frac{1}{2}\cos(2\theta^{(i)}_{\text{eff}})\cos(2\theta^{(f)}_{\text{eff}}) \\ &\quad + \frac{1}{2}\sin(2\theta^{(i)}_{\text{eff}})\sin(2\theta^{(f)}_{\text{eff}})\cos\left(\int_0^x \frac{\Delta m^2_{\text{eff}}(x')}{2E_\nu} dx'\right), \end{aligned} \tag{2.19}$$

where $\theta^{(i)}_{\text{eff}}$ is the effective mixing angle at the initial position and $\theta^{(f)}_{\text{eff}}$ at the final position. This approximation is suitable for solar neutrinos and supernova neutrinos.

Outside the adiabatic regime, we have additional effects. Here, we summarize the results in [124]. For three generations, there are two resonance energies

$$E^R_L \approx \frac{\Delta m^2_{21}}{2\sqrt{2} G_F n_e} \cos 2\theta_{12} \qquad\qquad E^R_H \approx \frac{\Delta m^2_{31}}{2\sqrt{2} G_F n_e} \cos 2\theta_{13} \tag{2.20}$$

.

When the neutrino energy is below E^R_L, we remain in the vacuum oscillation regime. Between E^R_L and E^R_H the $\nu_1 - \nu_2$ mixing is important. Above E^R_H, all eigenstates can mix and the interference between the mass eigenstates creates wiggles in the oscillation probability, as a function of energy. These wiggles will also be revisited in Chapter 4. In this regime, we have non-adiabatic oscillations, which continues until you reach an energy where the mass separation grows so large that all mass eigenstates are decoupled.

Having discussed the more fundamental results of neutrino oscillations, we discuss some of the differences that arise between the normal and inverted mass orderings. In the context of vacuum propagation, we are dealing with propagation over cosmological distances where Eq. (2.14) applies and does not depend on Δm^2. We do point out that there are minor differences between the NO and IO oscillation fits for θ_{23} and δ_{CP}, but overall the effect on the oscillation formula is small. For θ_{23}, both NO and IO fits are close to the maximal mixing $\theta_{23} \approx \pi/4$; for δ_{CP} the effect between the different values is suppressed by the small value of θ_{13}. By virtue of Eq. (2.17), IO uses $\Delta m^2_{32} < 0$, which would change the effective masses in matter and would have an impact on the oscillation

patterns. This would also be true for adiabatic oscillations.

2.5 Cosmology

To describe the evolution of the Universe, general relativity is required. Here we discuss the relevant portions, with a more in-depth approach presented in e.g. [125]. The starting point is a metric tensor that describes a homogenous, isotropic and expanding universe (at large scales). The metric that satisfies these conditions is known as the Friedmann-Robertson-Walker (FRW) metric, with line element

$$ds^2 = c^2dt^2 - a^2(t)\left(\frac{dr^2}{1-kr^2} + r^2(d\theta^2 + \sin^2\theta d\phi)\right), \tag{2.21}$$

where $a(t)$ known as the scale factor and k is a parameter that describes the curvature of the universe and has dimensions of length^{-2}. The convention for the scale factor is that $a(t_0) = 1$, where t_0 is the present time. Notice that the line element would be identical to that of spherical coordinates in the case of $k = 0$ (flat universe) and $a(t)$=1 (static universe). The metric is derived from geometrical considerations, but the time dependence of $a(t)$ must be determined by solving the Einstein equations. For this particular metric, the Einstein equations are reduced to two Freidmann equations:

$$\left(\frac{\dot{a}}{a}\right)^2 = \frac{8\pi G}{3}\rho - \frac{k}{a^2} + \frac{\Lambda}{3} \qquad \frac{\ddot{a}}{a} = -\frac{4\pi G}{3}\rho + \frac{\Lambda}{3}, \tag{2.22}$$

where Λ is the cosmological constant and ρ is the energy density of the universe. The density ρ can be separated into matter and radiation densities, labeled as ρ_M and ρ_R respectively. Define the Hubble parameter

$$H(t) = \frac{\dot{a}}{a}, \tag{2.23}$$

as well as the following parameters

$$\Omega_M = \frac{8\pi G\rho_{M,0}}{3H_0^2} \qquad \Omega_R = \frac{8\pi G\rho_{R,0}}{3H_0^2} \qquad \Omega_k = -\frac{k}{a_0^2H_0^2} \qquad \Omega_\Lambda = \frac{\Lambda}{3H_0^2}, \tag{2.24}$$

where the subscript 0 means that the quantity is evaluated at the present time, t_0. H_0 is known as the Hubble constant. The parameters Ω are named density parameters and are nonnegative dimensionless quantities. We assert that $\rho_M \propto a^{-3}$ and $\rho_R \propto a^{-4}$ (see e.g. [125] for the proof and assumptions made), which lets us write the first Friedmann

equation as

$$H(t) = H_0\sqrt{\Omega_R a^{-4} + \Omega_M a^{-3} + \Omega_k a^{-2} + \Omega_\Lambda}, \tag{2.25}$$

which, by definition of H_0, is subject to the constraint

$$\Omega_R + \Omega_M + \Omega_k + \Omega_\Lambda = 1. \tag{2.26}$$

Eq. (2.25) allows us to solve for $a(t)$ by separation of variables. For our purposes, we will be using the parameters $\Omega_M = 0.3$ and $\Omega_\Lambda = 0.7$ as measured by the Planck collaboration, which corresponds to a flat Universe that is dominated by matter (rather than radiation) today [126].

We can use Eq. (2.21) to describe cosmological redshift by relating the redshift z to the scale factor a. For a light wave moving in the radial direction, we impose $ds^2 = 0$ which leads to

$$c^2 dt^2 = a^2(t)\frac{dr^2}{1 - kr^2} \tag{2.27}$$

If a crest leaves the source at r_1 at a time t_1 and reaches the observer at $r = 0$ at t_2, we have

$$\int_{t_1}^{t_2} \frac{dt}{a(t)} = \int_0^{r_1} \frac{dr}{\sqrt{1 - kr^2}} \tag{2.28}$$

If a second crest leaves the source at $t_1 + \Delta t_1$ and reaches the observer at $t_2 + \Delta t_2$, we have the above equation, where the right hand side remains unchanged. By splitting the integration interval into subintervals, we get

$$\int_{t_1}^{t_1+\Delta t_1} \frac{dt}{a(t)} = \int_{t_2}^{t_2+\Delta t_2} \frac{dt}{a(t)} \tag{2.29}$$

Since Δt is many orders of magnitude smaller than the timescales in which a changes, we can take a to be constant along the interval, leaving us with

$$\frac{\Delta t_1}{a(t_1)} = \frac{\Delta t_2}{a(t_2)} \tag{2.30}$$

Notice that Δt is the period, so we can rewrite this equation in terms of emitted and observed frequencies or wavelengths. For an observer in the present, we then have

$$\frac{\lambda_2}{\lambda_1} = 1 + z = \frac{a(t_2)}{a(t_1)}. \tag{2.31}$$

From this equation, it follows that photons are redshifted as space itself expands, which

makes this redshift different from the usual Doppler redshift. By definition, the scale factor today is $a(t_2) = 1$, so we end up with

$$a(t) = \frac{1}{1 + z(t)}. \tag{2.32}$$

Keep in mind that z is a quantity that can be measured, by comparing spectral lines from a distant source against those on Earth. As redshift is an observable, it is preferable to write equations in terms of redshift, rather than a. For instance, we can rewrite H as

$$H(t) = \left|\frac{\dot{z}}{1+z}\right| = H_0\sqrt{\Omega_R(1+z)^4 + \Omega_M(1+z)^3 + \Omega_k(1+z)^2 + \Omega_\Lambda}, \tag{2.33}$$

and we can also relate time and redshift by solving the differential equation

$$\frac{dt}{dz} = -\frac{1}{(1+z)H_0\sqrt{\Omega_R(1+z)^4 + \Omega_M(1+z)^3 + \Omega_k(1+z)^2 + \Omega_\Lambda}}, \tag{2.34}$$

where the negative sign accounts for the fact that as redshift increases we are looking further into the past.

In an expanding Universe, the distance between two objects is not constant, so there are multiple ways to define distance between two points. In our case, there are two relevant distances: comoving distance and light-travel distance. As the neutrino propagates at speeds $\sim c$, space itself is expanding, such that the distance between neutrino and observer increases over time. For a source at redshift z, the distance travelled by the neutrino is given by the light-travel distance

$$D = c\int_0^z \frac{dz'}{H_0(1+z')\sqrt{\Omega_R(1+z)^4 + \Omega_M(1+z)^3 + \Omega_k(1+z)^2 + \Omega_\Lambda}}. \tag{2.35}$$

This is the distance that we will be using to propagate neutrinos. Finally, the expansion of the Universe will also cause particles to lose energy as they travel. Just as the photon is redshifted and has its frequency reduced by a factor $1/(1+z)$, so do the neutrinos lose energy according to

$$\frac{\varepsilon_\nu(z_2)}{\varepsilon_\nu(z_1)} = \frac{1+z_2}{1+z_1}. \tag{2.36}$$

In this equation, we point out that ε_ν is the energy in the comoving frame, a special frame which moves with the Hubble flow and perceives the CMB as isotropic. Thus, a

neutrino with energy ε_ν at redshift z will be observed with an energy

$$E_\nu = \frac{\varepsilon_\nu}{1+z}. \tag{2.37}$$

We use E_ν for observed energy on Earth, to distinguish it from energy in the source frame which has yet to experience expansion losses. In the limit $z \ll 1$, $\varepsilon_\nu \approx E_\nu$, which is suitable for sources closer than $\mathcal{O}(100)$ Mpc.

2.6 Optical Depth

Both in neutrino propagation and general astrophysical scenarios, the concept of optical depth is important to assess whether a certain interaction is likely to take place and, if so, how severely it may attenuate particle fluxes. Consider a flux ϕ of monoenergetic particles crossing a material with target number density n over a distance D. The optical depth τ is defined as

$$\tau = \int_0^D n(x)\sigma dx, \tag{2.38}$$

where σ is the cross section. If σ describes an absorption process, τ is useful to determine the flux as the particles propagate through the material, which is given by

$$\phi(x) = \phi(0)e^{-\tau}. \tag{2.39}$$

For a uniform slab of length D, the flux would thus be reduced by a fraction $\exp(-\tau)$, with $\tau = n\sigma D$.

It is also possible that particles are injected at different locations inside the material, such that each one propagates a different lengths before exiting. In such a situation, it is more suitable to use an averaged attenuation factor

$$\frac{1}{D}\int_0^D \exp[-n\sigma(D-x)]dx = \frac{1-\exp(-\tau)}{\tau}, \tag{2.40}$$

with $\tau = n\sigma D$. Even if $\tau \gg 1$, the overall flux would be reduced by a factor of $1/\tau$ instead of being fully depleted. This factor is a result of the particles closest to the end of the slab which manage to escape with little attenuation.

In a more general sense, σ can describe other processes, such as scattering. In this broader context, when $\tau \gg 1$ we say that the environment is optically thick and when $\tau \ll 1$ it is optically thin. In the optically thin case, the probability for a scattering

to take place is $\tau + \mathcal{O}(\tau^2)$. As the probability for multiple scatterings to take place is negligible, we can also call this case the one-scattering limit.

2.7 Supernova neutrinos

Here we discuss the neutrino production mechanism in supernova. Supernova neutrinos have a typical energy of ~ 10 MeV and are produced during the core-collapse process. This production mechanism is inherently different from the photopion production process that we will discuss in the next chapter.

A supernova (SN) is a powerful, transient event that occurs when massive stars reach the end of their lifetime. SNe are classified according to the presence or absence of spectral lines. Type I SNe show no hydrogen in their spectra, while type II does. Type Ibc supernovae (SNe) are characterized by the lack of hydrogen (type Ib) or hydrogen and helium (type Ic) spectral lines (see [127] for a review). The absence of these lines indicates that these dying stars have stripped their H/He envelopes prior to explosion. For this reason, they are classified as stripped-envelope supernovae (SESNe). Type Ibc and II SNe are of particular interest to us, as their explosions occur as a result of the core-collapse mechanism.

While the progenitors for Type Ibc SNe are not known, they are likely to be Wolf-Rayet (WR) stars with an initial mass larger than $25 M_\odot$ and lost a significant amount of mass through strong stellar winds [128]. Among Type Ic SNe we also have broad-line (BL) Type Ic SNe, with broad features in their electromagnetic spectra.

BL SNe Ic are the only type of CCSNe associated with GRB emissions [129–132]. However, observations suggest that only a small fraction ($\sim 10^{-3}$) of CCSNe are powered by jets and form GRBs, (e.g [133, 134]). This motivates the possibility that the majority of these jets are choked, providing a unified picture of the GRB-SNe connection [135–137]. Another alternative is that the jet is off-axis.

The core-collapse mechanism is complex and not fully understood, although the neutrino-driven mechanism of a supernova explosion is a popular candidate. Here we describe the process of neutrino production in the core-collapse supernova (CCSN) and how it is expected to drive the explosion. Underlying details are beyond the scope of this work and would require a three-dimensional SN hydrodynamical simulation.

The progenitor consists of a core with an existing iron and nickel core. As the iron core grows and the star begins to collapse, the temperature in the core increases until the thermal photons have enough energy to allow the photodisintegration of iron, breaking

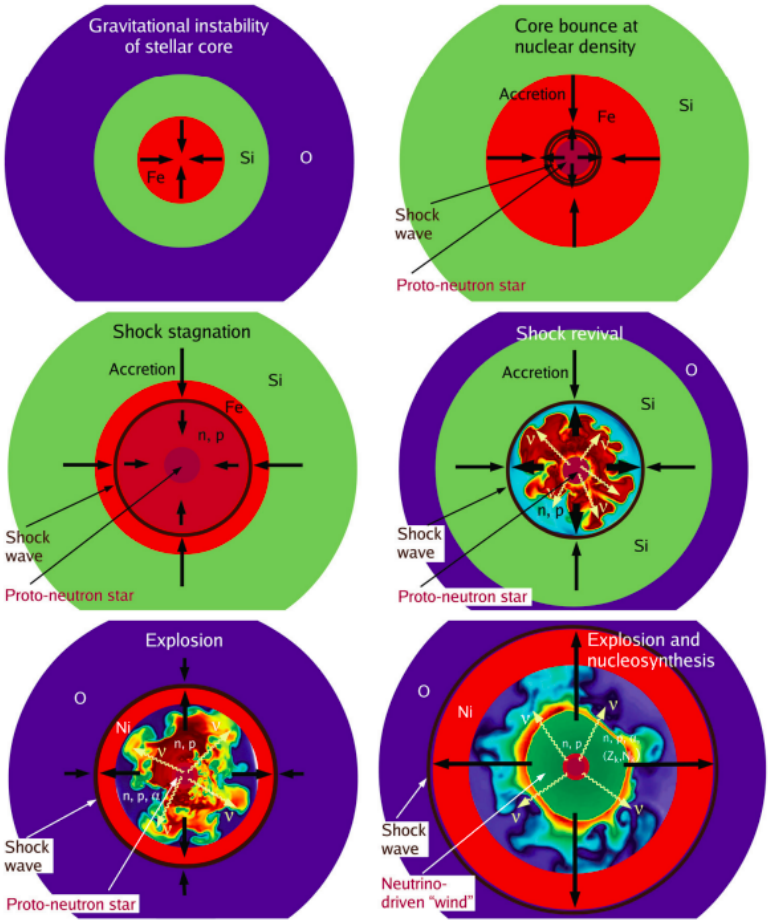

Figure 2.2. Schematic setup of core-collapse supernova, starting with the core collapse (top left), followed by core bounce (top right), shock stagnation (middle left), shock revival (middle right), explosion (bottom left) and formation of neutrino-driven winds (bottom right). Figure from Ref. [2].

the iron nuclei into helium nuclei. Once this happens, the star becomes gravitationally unstable, meaning that its adiabatic index has fallen to the point where hydrostatic equilibrium cannot be mantained and the collapse forces protons and electrons to combine to neutrons via electron capture, producing ν_es.

As the core continues to collapse, densities are large enough to capture neutrinos through neutral-current neutrino scattering with nucleons. Eventually the core reaches nuclear density and the core stops collapsing due to the repulsive effects of the nuclear force. This repulsion causes the inner core to bounce back, generating a shock. Behind the shock, electron capture takes place, creating additional neutrinos. At the same time, photodisintegration of iron nuclei continues, so the outward propagation of the shock is halted at 100-200 km [2]. A stalled shock would cause the explosion to fail, so a

mechanism to revive the shock is needed. Colgate and White [138] suggested that from the gravitational binding energy released by the gravitational collapse, which is about a hundred times larger than the kinetic energy $\sim 10^{51}$ erg of traditional SN ejecta, a small fraction could be reabsorbed by the star for shock revival. One of the methods is the delayed neutrino-driven explosion [139], where neutrinos can deposit energy ~ 100 ms after core bounce and lead to a successful explosion. The schematic setup is shown in Fig. 2.2.

The simulated supernova spectrum $dN_\nu/dE_\nu dt$ is not well-described by a purely thermal spectrum. Instead, we use the fit suggested in Ref. [140]

$$\frac{dN_\nu}{dE_\nu dt} = \frac{L_\nu}{\langle E_\nu \rangle^2} \frac{(\alpha+1)^{\alpha+1}}{\Gamma(\alpha+1)} \left(\frac{E_\nu}{\langle E_\nu \rangle} \right)^\alpha \exp\left(-\frac{(\alpha+1)E_\nu}{\langle E_\nu \rangle} \right), \tag{2.41}$$

where $\langle E_\nu \rangle$ is the average neutrino energy, α is a pinching parameter, L_ν is the neutrino luminosity, and Γ is the Euler Gamma function. The neutrino luminosity is a time-dependent quantity, which depends on how the SN explosion was simulated (e.g. [141, 142]).

Chapter 3
High-energy neutrino production

3.1 Introduction

While supernova neutrinos have been briefly mentioned in the previous section, high-energy neutrino sources have a different production mechanism, which warrants further discussion. In this section, we cover the generic mechanism of high-energy neutrino production and how it applies to gamma-ray bursts and magnetars. We then give an overview of IceCube, how it detects neutrinos and what the measurements tell us about the neutrino sources.

3.2 Neutrino production channels

The generic mechanism for high-energy neutrino production begins with cosmic rays (CRs). Within astrophysical sources, we typically expect some CR acceleration mechanism which varies from source to source. One of the more prevalent mechanisms is the Fermi acceleration mechanism, which generically predicts an ε^{-2} CR spectrum [143] (see also [144] for a review on particle acceleration at shocks).

As CRs continue to propagate in the source, they will undergo scattering with either protons (pp), or with the ambient photons ($p\gamma$). For more complete models, one may also include interactions involving nuclei instead of protons. Whether the interaction is pp or $p\gamma$, we expect pion production, which leads to neutrinos.

We first analyze the case of $p\gamma$ interactions. For a proton at rest, the photon energy threshold is

$$\epsilon_{r,\mathrm{thres}} = m_\pi + \frac{m_\pi^2}{2m_p}, \tag{3.1}$$

which is about 145 MeV for π^0. In the case of $p\gamma$, resonant production of $\Delta^+(1232)$

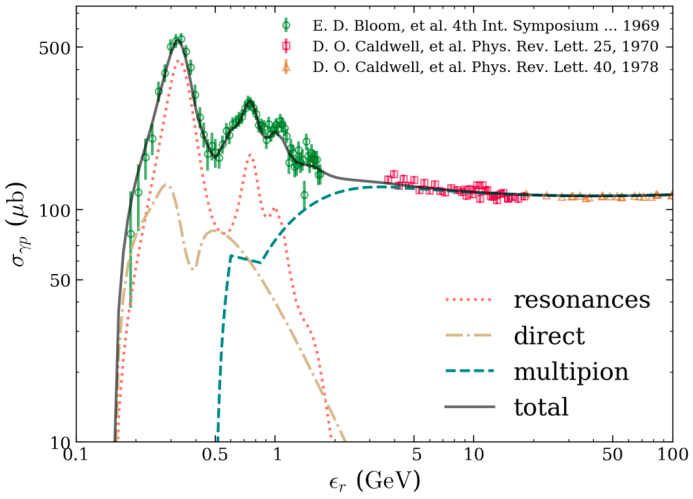

Figure 3.1. $p\gamma$ photopion production cross section as a function of photon energy ϵ_r with a target proton at rest. The total cross section is given by the solid black curve. The resonant, direct and multipion production channels are shown as orange, yellow and teal curves, respectively. From Ref. [3]

is also possible and occurs slightly above threshold. Assuming such a resonance, the outgoing particles can be either $n + \pi^+$ or $p + \pi^0$, with these two occurring at a ratio of 1:2. There are other more massive baryons that can be resonantly produced, such as $N^+(1440)$ and $\Delta^+(1700)$, but the cross section for these channels is not as large. Excluding resonance, direct pion production is dominant until $\epsilon_r \approx 1$ GeV and among these direct production channels, $p\gamma \to n\pi^+$ is almost entirely dominant. Once $\epsilon_r > 1$ GeV, multi-pion production is the dominant channel. This can be seen in the left panel of Fig. 3.1

Charged pions then follow the decay chain $\pi^+ \to \mu^+ + \nu_\mu$ and $\mu^+ \to e^+ + \nu_e + \bar{\nu}_\mu$. Neutrons decay via β decay $n \to p + e^- + \bar{\nu}_e$, while neutral pions decay into two photons. From these decay chains it follows that cosmic rays can produce photon and neutrino signals, which is main motivation for multimessenger astrophysics.

The energy correspondence between parent proton and daughter neutrino, based on the mean inelasticity of the pion production process, is $\varepsilon_p = 20\varepsilon_\nu$ ($\varepsilon_p = 25\varepsilon_\nu$) for $p\gamma(pp)$ interactions. For π^0 decay, each photon carries 1/2 the pion energy. To convert a proton injection spectrum $dN_p/d\varepsilon_p$ into a neutrino spectrum $dN_\nu/d\varepsilon_\nu$, we assume that all cosmic ray protons have been depleted due to pion production. Secondly, in the pion decay chain, each neutrino carries roughly 1/4 of the charged pion energy. Taking these considerations into account, we arrive at the formula for the spectrum for each neutrino

$$\varepsilon_\nu^2 \frac{dN_\nu}{d\varepsilon_\nu} = \frac{K}{4(1+K)} \varepsilon_p^2 \frac{dN_p}{d\varepsilon_p}, \tag{3.2}$$

where $K = 1 (K = 2)$ for $p\gamma (pp)$ interactions. Thus, for $p\gamma$ the overall factor is 1/8, where the extra factor 1/2 comes from the approximate $\pi^+ : \pi^0 = 1 : 1$ ratio for the pion production channels [145]. For pp the factor is 1/6. This formula is useful for its simplicity, as well as showing that the shape of the neutrino spectrum follows that of the CR spectrum.

If we want a more accurate depiction of neutrino production, we need to include energy distribution details of the $pp/p\gamma$ collisions and the meson decays. We use the notation $F_{i\to f}$ to indicate the energy distribution of the final particles f arrising from a single $i \to fX$ collision or decay. These distributions have units of energy^{-1} and are normalized so that its energy integrals are equal to particle multiplicity. We will be using this approach for pp interactions in magnetars, with $F_{pp\to h}$ given by

$$F_{pp\to h}(\varepsilon_h, \varepsilon_p) = \frac{1}{\varepsilon_p} \frac{1}{\sigma_{pp}(\varepsilon_p)} \frac{d\sigma}{dx_\varepsilon}(\varepsilon_h, \varepsilon_p), \tag{3.3}$$

where $\sigma_{pp}(\varepsilon_p)$ is the total inelastic pp cross section, and $x_\varepsilon = \varepsilon_h/\varepsilon_p$, where ε_h is the hadron energy and ε_p is the proton energy in the lab frame. The differential cross sections $d\sigma/dx_\varepsilon$ depends on the hadronic interaction models, which can be provided analytically or by software packages (e.g. SIBYLL, PYTHIA, GEANT4). As an example, we show in Fig.3.2 the inelastic cross sections for pp, $\pi^+ p$ and $K^+ p$ interactions, as given by SIBYLL 2.3 [146–148]. We see that the cross sections are of $\mathcal{O}(100)$ mb.

A more accurate depiction of meson decay will also be used for the magnetar scenario, so we include the formulas that convert a pion spectrum into a neutrino spectrum [149–151]. The same formulas can be applied to kaons, by substituting $m_\pi \to m_K$ and multiplying the resulting spectrum by the $K \to \mu\bar{\nu}_\mu$ decay branching fraction of 0.636.

For the two-body decay of ultrarelativistic pions, the spectrum of the final lepton ℓ is given by the convolution of the initial spectrum and the energy distribution of the interaction channel

$$\frac{dN_\ell}{d\varepsilon_\ell}(\varepsilon_\ell) = \int_{\varepsilon_{\pi\,\min}^\ell}^{\varepsilon_{\pi\,\max}^\ell} d\varepsilon_\pi \frac{dN_\pi}{d\varepsilon_\pi} F_{\pi\to\ell}(E_\ell, E_\pi)\,, \tag{3.4}$$

where $\ell = \mu,\ \nu$. In fact, the decay spectra for the 2-body pion decay are

$$F_{\pi\to\mu}(\varepsilon_\mu, \varepsilon_\pi) = F_{\pi\to\nu}(\varepsilon_\nu, \varepsilon_\pi) = \frac{1}{\varepsilon_\pi} \frac{1}{1-\lambda_\pi}. \tag{3.5}$$

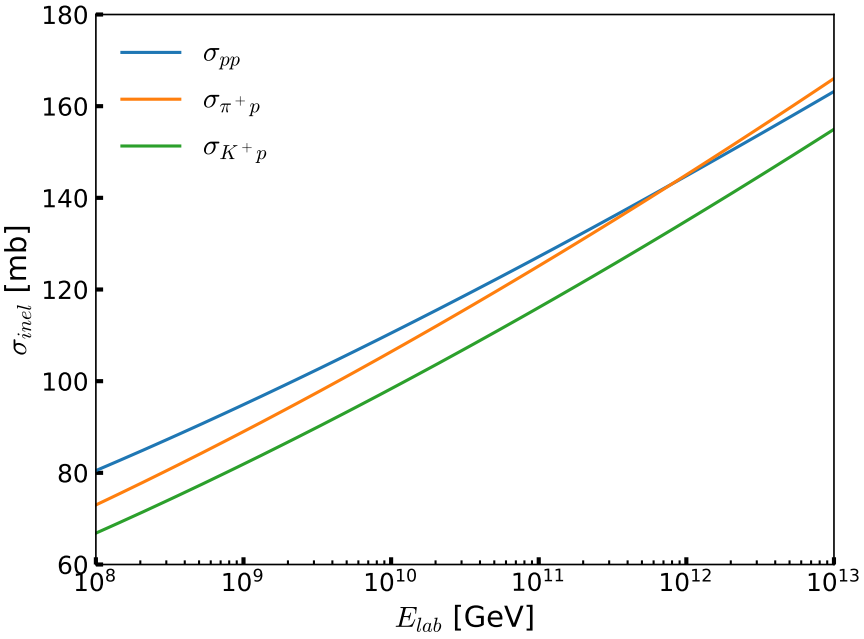

Figure 3.2. Inelastic cross section for pp, $\pi^+ p$ and $K^+ p$ collisions as a function of the target proton energy $E_{\rm lab}$ in the proton's rest frame. Cross sections are given by SIBYLL.

for $\lambda_\pi = (m_\mu/m_\pi)^2$. The flat spectrum for ultrarelativistic pions occurs because, as a scalar, the pion decays isotropically in its rest frame. An isotropic distribution, when boosted by a Lorentz transformation with a very large Lorentz factor, will give a flat energy distribution. The kinematic constraints are that $\varepsilon_\mu/\varepsilon_\pi > \lambda_\pi$ and $\varepsilon_\nu/\varepsilon_\pi < 1 - \lambda_\pi$, so the limits in Eq. (3.4) are

$$\varepsilon^\nu_{\pi\,\min} = \varepsilon_\nu/(1-\lambda_\pi) \tag{3.6}$$

$$\varepsilon^\nu_{\pi\,\max} = \varepsilon_p \tag{3.7}$$

$$\varepsilon^\mu_{\pi\,\min} = \varepsilon_\mu \tag{3.8}$$

$$\varepsilon^\mu_{\pi\,\max} = \varepsilon_\mu/\lambda_\pi \ . \tag{3.9}$$

The differential neutrino spectrum from the $\pi \to \mu \to \nu$ chain in the absence of muon energy loss processes is

$$\frac{dN_\nu}{d\varepsilon_\nu}(\varepsilon_\nu) = \int_{\varepsilon_\nu}^{\infty} d\varepsilon_\mu \int_{\varepsilon_\mu}^{\varepsilon_\mu/\lambda_\pi} d\varepsilon_\pi \frac{dN_\pi}{d\varepsilon_\pi} F_{\pi\to\mu}(\varepsilon_\mu, \varepsilon_\pi) F_{\mu\to\nu}(\varepsilon_\nu, \varepsilon_\mu) \tag{3.10}$$

where the muon three-body decay distribution is [149, 150]

$$F_{\mu\to\nu}(\varepsilon_\nu, \varepsilon_\mu) = \frac{1}{\varepsilon_\mu}\left[G_0\left(\frac{\varepsilon_\nu}{\varepsilon_\mu}\right) + h_{\pi\to\mu}\left(\frac{\varepsilon_\mu}{\varepsilon_\pi}\right) G_1\left(\frac{\varepsilon_\nu}{\varepsilon_\mu}\right)\right] \tag{3.11}$$

The factor $h_{\pi\to\mu}$ is the μ^- polarization in π^- decays, with

$$h_{\pi\to\mu}(x_\mu) = \frac{1+\lambda_\pi}{1-\lambda_\pi} - \frac{2\lambda_\pi}{(1-\lambda_\pi)x_\mu}\ , \tag{3.12}$$

When considering μ^+ decay, Eq. (3.11) needs the substitution $h_{\pi\to\mu} \to -h_{\pi\to\mu}$. However, Eq. (3.12) also requires the right hand side to be multiplied by -1, to account for the opposite polarization of μ^+ when compared to μ^-. Combining these sign changes, it follows that the ν_μ distribution from $\pi^- \to \mu^- \to \nu_\mu$ is identical to the distribution of $\bar{\nu}_\mu$ from $\pi^+ \to \mu^+ \to \bar{\nu}_\mu$. The same sign changes apply for ν_e, so ν_e and $\bar{\nu}_e$ distributions are identical to each other. The formulas for G_0 and G_1 for μ^- are summarized in Table 3.1.

$\mu \to \nu_\alpha$	$G_0(y)$	$G_1(y)$
ν_μ	$\frac{5}{3} - 3y^2 + \frac{4}{3}y^3$	$\frac{1}{3} - 3y^2 + \frac{8}{3}y^3$
$\bar{\nu}_e$	$2 - 6y^2 + 4y^3$	$-2 + 12y - 18y^2 + 8y^3$

Table 3.1. Functions used in Eq. (3.11) to calculate the neutrino spectrum from μ^- decay.

3.3 Interaction timescales and cooling

To properly account for neutrino production, we need to consider two important factors

- Particle production, in this case pions, is not always efficient. Even if the ambient photons or protons are such that we achieve threshold energy, target density may not be enough for a significant number of pions to be produced.
- Since particles at the source are propagating in dense media, interactions with the surrounding environment can initiate particle cooling. Here, it is important to know whether the particles in question lose a significant amount of energy before interacting or decaying.

Here we review some of the relevant processes which can cool particles. Within our framework, we are mostly interested in proton, pion and muon cooling. As these particles propagate in the plasma, they will move through magnetic fields, photon fields and

ambient protons and electrons. The processes reviewed here are also discussed extensively in textbooks (e.g. [152]).

Synchrotron radiation

As charged particles move through a uniform magnetic field, it will gyrate about the magnetic field direction. The centripetal acceleration experienced by the charged particle leads to radiation emission, known as synchrotron radiation. Consider a uniform magnetic field $\mathbf{B}$ and a particle moving with velocity $\mathbf{v}$. Let α be the angle between the vectors $\mathbf{B}$ and $\mathbf{v}$. The energy loss rate for an electron of energy ε is

$$-\frac{d\varepsilon}{dt} = 2\sigma_T c\beta^2 U_B \gamma^2 \sin^2\alpha, \tag{3.13}$$

where σ_T is the Thomson cross section, $\beta = v/c$, $U_B = B^2/8\pi$ is the magnetic field energy and γ is the particle's Lorentz factor. In the media of interest, the direction of the magnetic field is likely to be randomized, so we can average over an isotropic distribution of pitching angles, giving

$$-\frac{d\varepsilon}{dt} = \frac{4}{3}\sigma_T c\beta^2\gamma^2 U_B. \tag{3.14}$$

We can also define the synchrotron cooling rate for the electron

$$t_{e,\mathrm{syn}}^{-1} = \left|\frac{1}{\varepsilon}\frac{d\varepsilon}{dt}\right| = \frac{4}{3}\sigma_T c\beta^2 \frac{\varepsilon}{m_e^2} U_B. \tag{3.15}$$

The definition can also be extended to other charged particles. The constant $\sigma_T \propto e^4/m_e^2$ only appears for the purposes of simplifying the factors that appear in the general formula for $d\varepsilon/dt$. Hence, we should substitute $e \to Ze$ and $m_e \to m$ for a particle of charge Ze and mass m. With these changes, we have

$$t_{\mathrm{syn}}^{-1} = \frac{4}{3}\sigma_T Z^4 m_e^2 c\beta^2 \frac{\varepsilon}{m^4} U_B. \tag{3.16}$$

From this expression, we see that the cooling rate is proportional to ε. Secondly, the m^{-4} behavior shows that more massive particles have significantly slower cooling compared to light ones, such as the electron.

Inverse Compton scattering

Charged particles will also move through ambient photons. For the purposes of

producing high-energy neutrinos above 1 TeV, we will be typically working with protons > 1 TeV to initiate pp and $p\gamma$ interactions. Within dense environments such as GRB jets, we typically encounter thermal photons with temperatures in the 100 eV - 1 MeV range. The case of GRB jets will be analyzed further in Chapter 4.

As the charged particles are more energetic than the target photons, they can lose energy by upscattering the lower energy photons via the process known as Inverse Compton (IC) scattering. Assuming an isotropic radiation field, the electron energy loss rate in this process is

$$-\frac{d\varepsilon}{dt} = \frac{4}{3}\sigma_T c\beta^2\gamma^2 U_{\rm rad}. \tag{3.17}$$

Notice that this loss rate has the same form as (3.15), with $U_B \to U_{\rm rad}$. This result is only valid for low center-of-mass energies. In the case that the center-of-mass energy exceeds the electron's rest-mass energy, the Inverse Compton cross section $\sigma_{\rm IC}$, obtained from quantum electrodynamics, must be used instead of σ_T.

The Compton cross section is

$$\sigma_{\rm IC} = \frac{4}{3}\sigma_T \left(\frac{m_e}{m}\right)^2 \frac{1}{x}\left[\left(1 - \frac{4}{x} - \frac{8}{x^2}\right)\ln(1+x) + \frac{1}{2} + \frac{8}{x} - \frac{1}{2(1+x)^2}\right], \tag{3.18}$$

where $x = (s - m^2)/m^2$ and the Mandelstam variable s is the squared of the center of mass energy. In the non-relativistic limit, $s \approx m^2$ and from the Taylor expansion of $ln(1+x)$ for $x \ll 1$ we recover $\sigma_T(m_e/m)^2$. In the ultrarelativistic limit, $x \gg 1$ (Klein-Nishina regime) and the cross section scales as $\ln(1+x)/x$. This effect is the Klein-Nishina suppression, whereby the Compton cross section decreases with energy.

Proton-proton and photopion interaction timescales

In the previous section we established that protons undergo pp and $p\gamma$ interactions. For pp interactions, the case we consider is high-energy protons interacting with ambient protons which are assumed to be at rest, implicitly assuming that the surrounding environment is not hot enough to achieve $T \sim 1$ GeV.

The pp timescale t_{pp} is given by

$$t_{pp}^{-1} = \kappa_{pp} n_p \sigma_{pp} c, \tag{3.19}$$

where κ_{pp} is the proton's inelasticity, n_p is the target proton number density and σ_{pp} is the inelastic pp interaction cross section. For practical purposes, we take $\kappa_{pp} \sim 0.5$.

In the case of protons interacting with a photon field, we have to integrate over the

photon spectrum. We define the $p\gamma$ timescale $t_{p\gamma}$ from

$$t_{p\gamma}^{-1}(\varepsilon_p) = c \int_0^\infty d\varepsilon_\gamma \int d\Omega \frac{dn_\gamma}{d\varepsilon_\gamma}(\varepsilon', \Omega)(1 - \beta_p \cos\theta)\sigma_{p\gamma}\kappa_{p\gamma} \tag{3.20}$$

where $\sigma_{p\gamma}$ is the photopion production cross section, $\kappa_{p\gamma}$ is the proton's inelasticity, θ is the angle between the momenta of the proton and photon and $dn_\gamma/d\epsilon$ is the target photon density per unit energy per unit solid angle. Here, $\beta_p = 1 - 1/\gamma_p^2$ and $\gamma_p = \varepsilon_p/m_p$.

If the photon field is isotropic, like in the case of a thermal spectrum, the azimuthal angle can be integrated over. Using the photon energy in the proton's rest frame, $\bar{\varepsilon}_\gamma = \gamma_p \varepsilon_\gamma (1 - \beta_p \cos\theta)$, we get

$$t_{p\gamma}^{-1}(\varepsilon_p) = \frac{c}{2\gamma_p^2} \int_0^\infty \frac{d\varepsilon_\gamma}{\varepsilon_\gamma^2} \frac{dn_\gamma}{d\varepsilon_\gamma} \int_0^{2\gamma_p\varepsilon_\gamma} d\bar{\varepsilon}_\gamma \bar{\varepsilon}_\gamma \sigma_{p\gamma}(\bar{\varepsilon}_\gamma)\kappa_{p\gamma}. \tag{3.21}$$

Writing the equation in this form has the practical advantage that the target photon spectrum is in the outer integral. The inner integral only depends on the dummy parameter $\bar{\varepsilon}_\gamma$, so it can be precomputed numerically as a function of ε_γ.

Particle cooling

Combining all relevant cooling processes, we define

$$t_{\rm cool}^{-1} = \sum_i \frac{1}{t_i}, \tag{3.22}$$

where the summation runs over all cooling processes. To determine if cooling becomes important, we have to compare it against the typical time the particle remain susceptible to these processes. For example, it can be compared against the time the particle spends inside a region with strong radiation or magnetic fields. In the case of unstable particles, we are more interested in comparing its decay time against the cooling time. These situations are encountered in Chapter 4 and Chapter 5 in the context of GRB jets and magnetars, respectively.

3.4 High-energy neutrino detection

IceCube is currently the largest neutrino telescope. Since the 2013 detection of extraterrestrial neutrinos by IceCube [40], the collaboration has made several subsequent analyses on their collected data, as well as refining the algorithms used for their studies. Here we discuss what is the current status of high-energy neutrino measurements and what are

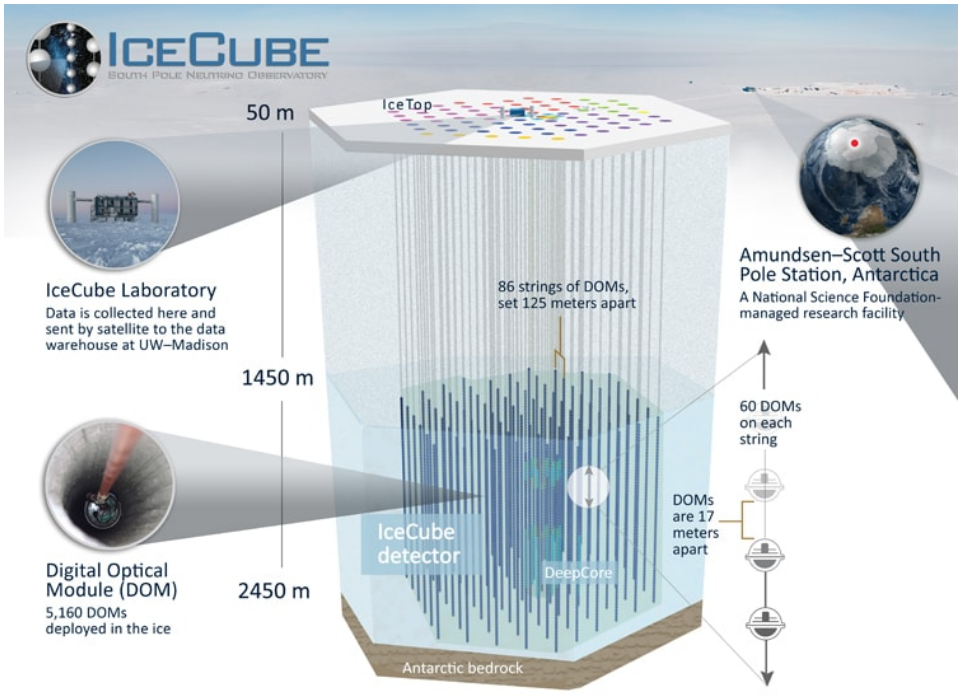

Figure 3.3. IceCube detector schematic. It currently consists of 86 strings, each one carrying 60 DOMs to detect light. Image from https://icecube.wisc.edu/science/icecube/.

the open questions remaining.

First, we look at how IceCube detects neutrinos. The detector consists of 86 strings that extend from 1450m to 2450m in depth, as shown in Fig. 3.3. Each string consists of 60 digital optical modules (DOMs). Incoming neutrinos interact with the nucleons in ice via deep inelastic scattering. The neutrino interaction channels with nucleons N can be divided into CC and NC (see Section 2.2):

$$\nu_\alpha N \rightarrow \ell_\alpha X \text{ (CC)} \tag{3.23}$$

$$\nu_\alpha N \rightarrow \nu_\alpha X \text{ (NC)}, \tag{3.24}$$

where X is typically a hadronic shower. The charged particles in the hadronic shower are highly relativistic and can easily move faster than the speed of light in ice. This motion results in Cherenkov radiation, which is emitted conically. The radiation is then picked up by the DOMs, which measure the energy deposited in the module and the arrival time of the signal, which allows a reconstruction of the neutrino event.

The hadronic shower initiated by the neutrino will typically be observed in a detector

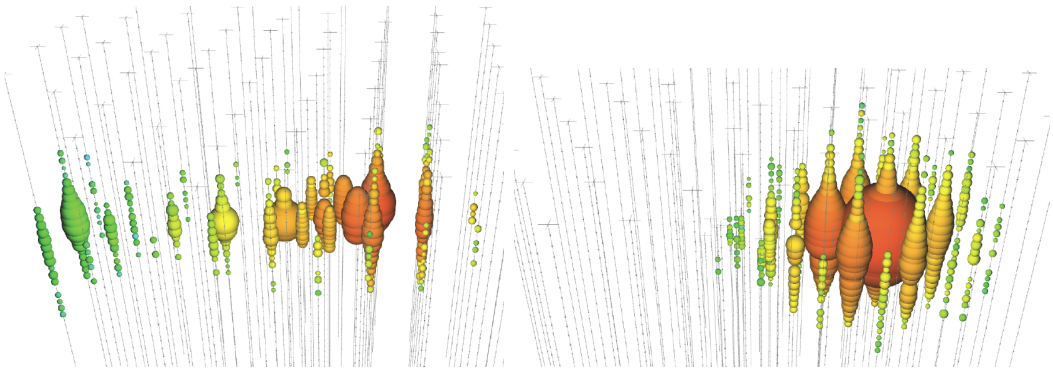

Figure 3.4. Left panel: Reconstruction of a muon track from a ν_μ event. Right panel: Reconstruction of neutral current events or ν_e and ν_τ events. Images from Ref. [4]. Large dots represent a larger amount of energy deposited into the detector.

as a blob, as shown in Fig. 3.4. The hadronic shower is the only component detected in NC interactions, as the outgoing neutrino is very unlikely to interact a second time within the detector's volume. In the case of ν_e CC interactions, the outgoing electron quickly deposits its energy inside the detector, so its signal would look similar to a hadronic shower. In the case of ν_μ CC interactions, the muon is highly penetrating and will leave a track. In some cases, the muon can also leave the detector.

The ν_τ CC interaction case is interesting, because the τ lepton created has a very short half-life. While the τ does leave a track, it decays so quickly that any signal from this track will be embedded inside the hadronic shower from the original ν_τ interaction.The tau predominately decays into a hadronic shower, which would also be indistinguishable from the initial shower. If the τ is highly energetic, then the τ track is long enough for two well-separated showers to be formed in the detector, a signal known as the "double bang".

The detector can distinguish between two broad topologies: cascades which correspond to NC interactions, ν_e and ν_τ CC interactions, and tracks which are initiated by ν_μ CC interactions. Each event topology has its own advantages and disadvantages. While track-like events have an angular resolution of $\sim 0.4^\circ$ at the highest energies, the muons do not deposit all their energy in the detector. On the other hand, ν_e and ν_τ CC cascades deposit all their energy in the detector which make them ideal for measuring the incident neutrino energy. Cascades induced by NC interactions have an outgoing neutrino, so the measured energy is only a lower limit for the neutrino energy.

The main background in IceCube comes from atmospheric muons entering the detector. This can be controlled by selecting upgoing muon tracks (i.e. muons that are coming from below the ground and are moving "up" into the detector) and produced by neutrino

interactions inside or close to the detector. After atmospheric muons, the remaining background consists of atmospheric neutrinos, which cannot be distinguished from astrophysical neutrinos on an event-by-event basis. Above ~ 300 TeV the atmospheric neutrino flux is very low, so most of those events are expected to be of astrophysical origin.

Now that we have discussed the background, we can move on to the detection of high-energy extraterrestrial neutrinos. The first result we will address is the measurement of the diffuse neutrino flux. The most common assumption is to take a single power-law hypothesis, where the flux normalization and the power-law index can be determined from a likelihood analysis. There are three basic questions of interest regarding the diffuse flux

- *What is the power-law index? Is the flux well-described by a single-power law?* While we should typically expect an E_ν^{-2} neutrino spectrum, this is not always the case. Other processes, including particle cooling, can modify the power-law index. Of course, the flux does not have to follow a power law, which indicates that models have to be refined to include more complete physical processes.

- *What is the flavor ratio of this flux?* IceCube is not able to distinguish between neutrinos and antineutrinos based on the topology, so the $\nu_\alpha + \bar{\nu}_\alpha$ flavor ratio is used instead. In the traditional setup, where neutrinos come from pion decay, the flavor ratio would be $\nu_e : \nu_\mu : \nu_\tau \approx 1 : 1 : 1$ on Earth after accounting for neutrino oscillations. Determining the ratio is important because it provides insight on what processes are occuring inside the source. If muons are cooled inside the source, then only ν_μ from the initial pion decay will leave the source. If the emission consists of mostly neutrons, which can be achieved in neutron-loaded outflows since neutrons do not cool via electromagnetic processes, then neutron decay leads to a flux of $\bar{\nu}_e$ leaving the source. These two alternatives would have a flavor ratio different from 1:1:1 after oscillations.

- *Is the diffuse flux truly isotropic?* Since neutrinos point back to their source, then the extragalactic neutrino flux should be fully isotropic. Anisotropy in the diffuse flux implies that there exist strong neutrino sources, which also points to the possibility of having a set of Galactic and nearby sources that account for a certain fraction of the flux.

We look at these points in order. The single-power law flux hypothesis assumes a

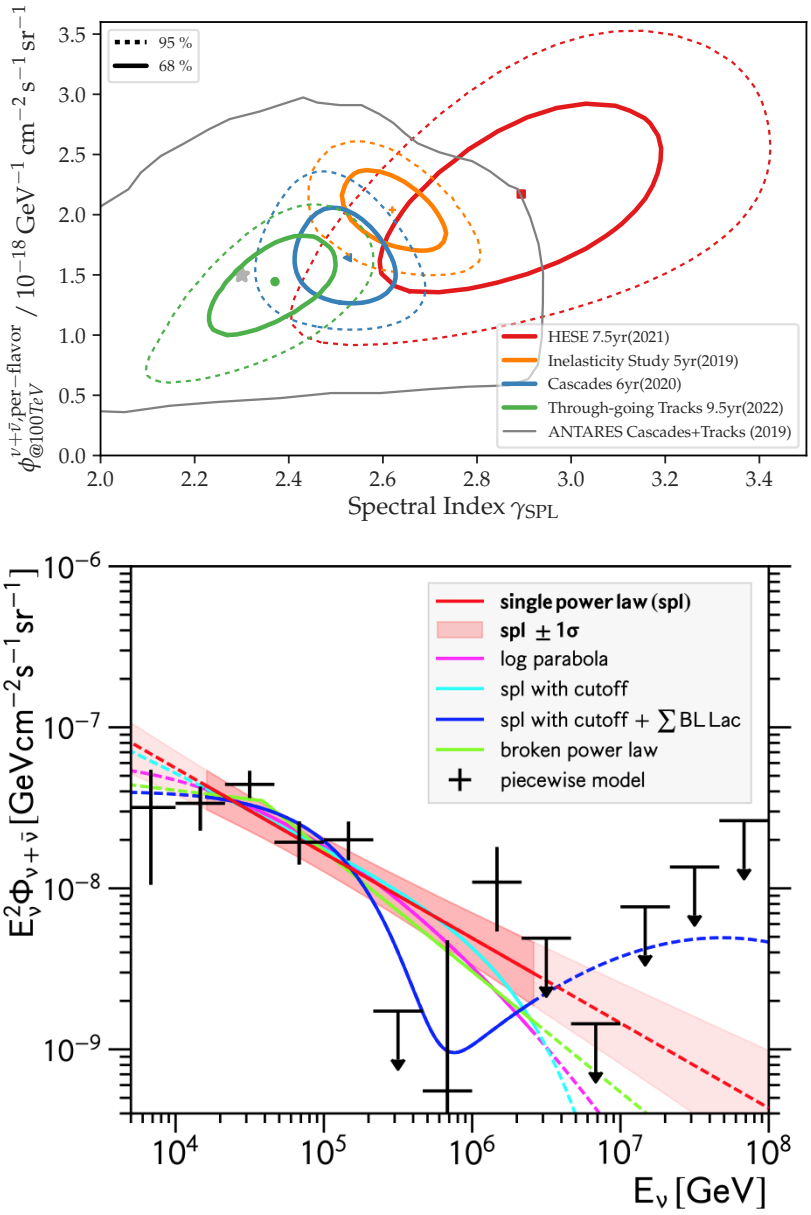

Figure 3.5. Top panel: Astrophysical diffuse neutrino flux single-power-law fits to date, assuming the fit given by Eq. (3.25). The green curve is the most recent best-fit using through-going tracks with 9.5 years of data [5]. The other fits use 7.5 years of high-energy starting events [6], 6 years of cascades [1] and 5 years of tracks [7]. ANTARES results for cascades and tracks are also included [8]. Panel from Ref. [9]. Bottom panel: Astrophysical neutrino flux per neutrino flavor given by the six-year cascade data [1]. The best-fit single-power-law fit is given by the red curve. Other astrophysical neutrino flux models shown by different colors. The curves are solid within the sensitive energy range of IceCube and dashed in the range outside of it. Panel from Ref. [10].

per-flavor flux of the form

$$\Phi(E_\nu) = \Phi^{\nu+\bar{\nu},\mathrm{per-flavor}}_{@100\mathrm{TeV}} \left(\frac{E_\nu}{100\mathrm{TeV}}\right)^{-\gamma_{\mathrm{SPL}}}, \tag{3.25}$$

where the normalization is taken to be the per-flavor flux at 100 TeV. The results are shown in the top panel of Fig. 3.5 for a variety of data sets. We see that the spectrum is softer than E_ν^{-2} in IceCube measurements. Moreover, there seems to be a slight tension between the different analyses. The flux parameters are derived from an assumption of a 1:1:1 flavor ratio, which does not have to be true, specially if cooling processes in the source are important. Secondly, each data set has its own event selection criteria and treatment of background events. In our case, it is interesting to consider the former explanation, as it pertains to astrophysical processes inside the source. Alternative flux models are shown in the bottom panel of Fig. 3.5 in the context of IceCube's six-year cascade data [10].

So far, IceCube measurements cannot exclude any of the traditional flavor ratio assumptions at a high confidence level. The current status is depicted in Fig. 3.6. In this case, a large majority of the flavor triangle is still contained within the 95% confidence level contour.

Regarding the distribution of neutrinos sources, IceCube carried several analyses looking for clustering of high-energy neutrino events. Two hotspots were reported in Ref. [46], one in the Northern and one in the Southern hermisphere, but were still found to be consistent with a background-only hypothesis (i.e. with the astrophysical diffuse flux plus atmospheric background). The search for neutrinos correlated to a catalog of sources found a neutrino excess in the direction of the galaxy NGC1068, with a significance of 2.9σ [46].

A subsequent analysis improved by new data processing, data calibration and event reconstruction method was carried out to search for neutrino sources [47]. There, NGC1068 was found to be the most significant source in the catalog, with a significance of 4.2σ. The neutrino excess from the direction of NGC1068 resulted in an expected 79^{+22}_{-20} neutrino events above the atmospheric and astrophysical neutrino backgrounds. The source flux follows an approximate $E^{-3.2}$ spectrum in the 1.5 TeV to 15 TeV energy range. One interesting result from this study is that, since neutrinos were detected in the TeV range, we should also expect TeV photons in light of $p\gamma$ interactions creating charged and neutral pions (see discussion in Section 3.2). However, the inferred TeV gamma-ray flux is more than an order of magnitude above the gamma-ray fluxes (and upper limits at

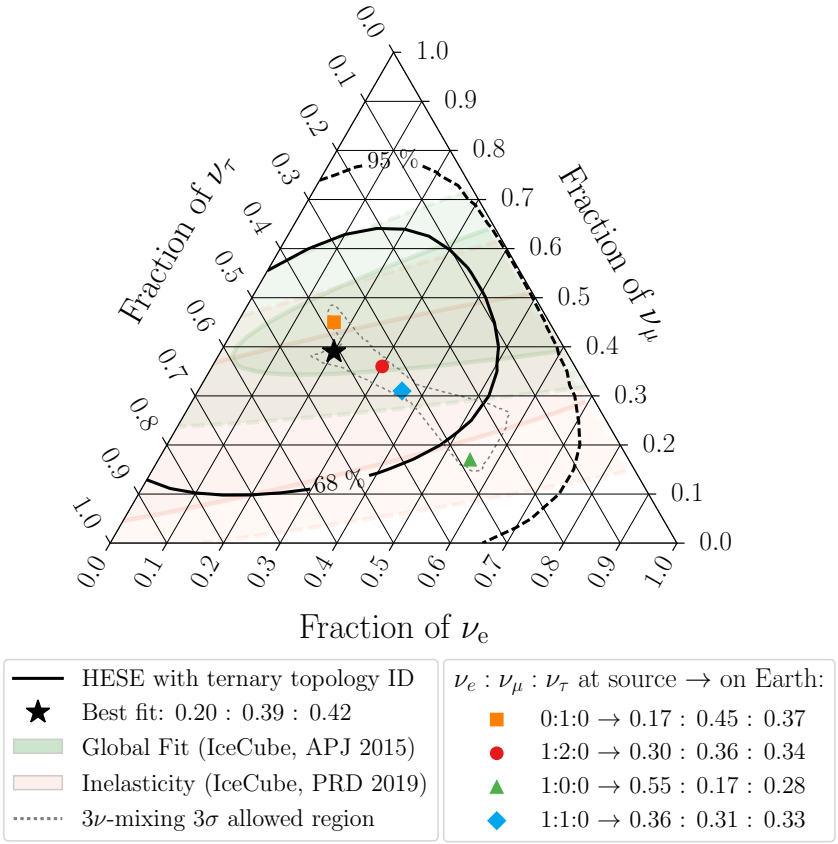

Figure 3.6. Flavor constraints on the astrophysical flavor ratio from different measurements. From [9].

the energies where no gamma-rays were observed) provided by Fermi-LAT and MAGIC. NGC1068 is therefore an example of a neutrino source that is opaque to gamma-rays.

Having discussed the status of IceCube measurements and how they correlate to multimessenger astrophysics, we can now develop neutrino source models and calculate their neutrino emissions. The associated fluxes will then be combined with IceCube data to extract information about their luminosities and event rates of specific types of neutrino sources.

Chapter 4
Oscillation of high-energy neutrinos from choked jets in stellar and merger ejecta

4.1 Introduction

Gamma-ray bursts (GRBs) are extremely luminous transients that are powered by compact objects, such as neutron stars or black holes. When a dying star collapses, the compact object launches relativistic jets that end up producing the GRB emission. The mechanism which keeps the central engine going varies. For example, black holes are powered by mass accretion, while neutron stars are powered by their fast rotation or their magnetic fields. These environments are expected to launch powerful relativistic jets.

For us to observe the jet's gamma-ray emission, the jet has to penetrate the stellar envelope first. If this occurs, we say that the jet breaks out of the progenitor. There is the natural possibility that the jet is stalled, in which case we observe no gamma rays due to photon attenuation within the stellar envelope. These choked jets lead to failed GRBs. Without an electromagnetic signal, the possibility of detecting a neutrino signal remains.

The production of relativistic ejecta in the jet is not expected to be steady. This means that the ejecta speed has some variability over time. Fast ejecta catches up to slower ejecta and the collision creates shock waves, which propagate into fast and slow jets. The jet's kinetic energy is converted into thermal energy, which is then radiated outwards via synchrotron radiation and IC scattering. This is the so-called internal shock

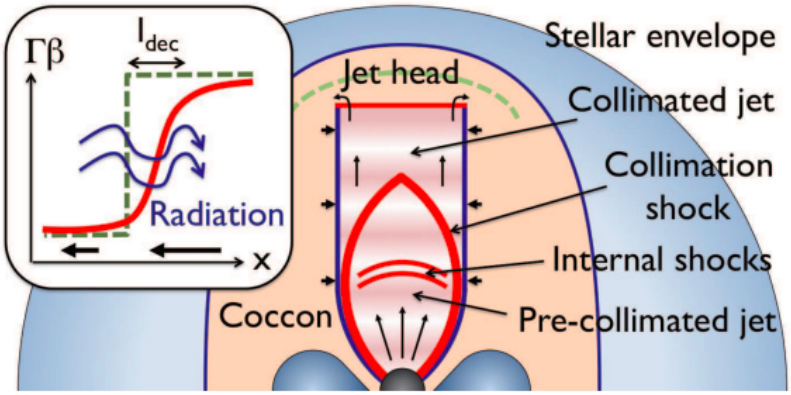

Figure 4.1. Graphical representation of GRB jet collimation within the stellar envelope. Cocoon pressure enables collimation and the jet becomes cylindrical. In the case of radiation mediated shocks, photons enter the upstream region. As a result, the shock now has a width determined by the deceleration scale $l_{\rm dec}$ and the strong shock jump which allows for efficient CR acceleration is lost. Figure from [11].

model [153,154]. The model provides an explanation for the short-scale time variability in GRB light curves, which is in the order of milliseconds, by connecting it to the variability time δt of the central engine itself.

We also have to account for the jet's propagation through different types of media, as their interaction determines the system dynamics, such as jet head velocity and collimation. There has been significant progress in understanding this physics, led by many analytical (e.g., [155–160]) and numerical (e.g., [11, 161–167]) studies. Here we outline the schematic picture for jet propagation as described in [160] and shown in Fig. 4.1. This will allow us to make more sophisticated models for particle production.

As the relativistic jet propagates outwards, it pushes the matter in front of it, creating a forward and reverse shock which is separated by a contact discontinuity. This region is called the jet head. As matter enters the head, it gets heated and flows sideways, creating a high pressure cocoon. If the cocoon pressure exceeds the jet's ram pressure (upstream momentum flux) then the jet becomes collimated, significantly reducing its opening angle. The collimation also forms oblique shocks at the base of the jet, which counteract the cocoon pressure at the expense of the unshocked jet being curved towards the jet's axis. The point where the unshocked jet converges is called the collimation shock radius. Beyond it, only the shocked jet remains and the flow is cylindrical. This scenario is illustrated in Fig. 4.1.

One way to characterize GRBs is via their isotropic-equivalent energy $E_{\rm iso}$, the

energy inferred from the GRB fluence assuming that the emission is isotropic. The total energy of the GRB can be $\sim 10^{53}$ erg. More recently, the most energetic GRB observed, GRB 221009 A, emitted an isotropic equivalent energy of $\sim 10^{54}$ erg [109]. As conical jets are expected to be formed, the GRB emission actually occurs over a given solid angle. Two jets are expected to be emitted in opposite directions, so for a jet opening angle θ_j the solid angle is $4\pi(1-\cos\theta_j)$. Since we only observe one of the jets, only half of the energy actually arrives to Earth. In the limit $\theta_j \ll 1$, the one-sided jet energy is $E_j = (\theta^2/4)E_{\rm iso}$. The examples presented here are low-luminosity GRBs (LLGRBs) [168, 169] with isotropic luminosities $\sim 10^{49}$ erg s^{-1}, and ultralong GRBs (ULGRBs) that last more than 1000s [170, 171]. Both are examples of low power (LP) GRBs.

GRBs are capable of producing neutrinos via photopion production. CRs accelerate inside internal shocks. The acceleration mechanism usually relies in the formation of plasma instabilities to obtain the isotropic particle momenta in the downstream, which is part of the Fermi first-order acceleration scenario. Shocks of this kind are called collisionless because they are not mediated by Coulomb scatterings between individual particles.

Ambient photons in the upstream region allow for pion production and leads to neutrinos, which escape the source. Afterwards, once the jet breaks out of the progenitor, photons and cosmic rays will propagate to the observer. Coincident production of photons and neutrinos means that if were to choose a group of GRBs, identified by their photon signal, we would expect neutrino emissions from those sources.

The IceCube collaboration looked at neutrinos coincident with sources from GRB catalogues, concluding that prompt neutrino emission from GRBs do not significantly contribute to the diffuse neutrino flux [172, 173]. Choked GRBs, where the jet does not escape the progenitor, are able to bypass constraints from such stacking analyses, because this type of burst emits neutrinos without an accompanying electromagnetic signal [174].

Having discussed the geometry of the jets, we can now address the parameters used for our studies. The rest of this chapter is the result of the work published in Ref. [114], showing how neutrino oscillation effects affect the GRB neutrino spectrum as it breaks out from the progenitor. We take a semi-analytic approach, where the particle physics for $p\gamma$ and pp interactions are handled via parametrizations and protons are assumed to lose a fixed fraction of its energy to the pions.

4.2 Choked LP GRB jets in a massive star

The schematic setup decribing how LP GRB jets propagate in a massive star follows Ref. [160]. A relativistic jet of luminosity L_j with an opening angle θ_j is injected into the surrounding medium, with ambient density ρ_a. As the jet pushes the matter in front of it, the jet head is formed, consisting of a forward and reverse shock. The jet head velocity β_h is [160]

$$\beta_h = \left(\frac{L_j}{c^5 t^2 \rho_a \theta_j^4}\right)^{1/5} \left(\frac{16\xi_a}{3\pi\xi_h\xi_c^2}\right)^{1/5} \tag{4.1}$$

where $\xi_a = 3/(3-\alpha), \xi_h = \xi_c = (5-\alpha)/3$ depend on $\alpha = -d\ln\rho_a/d\ln r$, where the derivative is evaluated at r, and $f_{\rm cc} \approx 0.01$ is a correction factor that is determined by numerical calculations [11]. One important feature of this analytical formula is that it cannot be applied when ρ_a falls faster than r^{-3}, where the parameter χ_a turns negative.

Matter is heated inside these shocks and will flow across the sides at a high pressure, creating a cocoon around the jet. If the pressure in the cocoon is sufficiently high, the jet will become collimated. Within the collimated regime, the cocoon's pressure reduces the jet opening angle, creating an oblique shock that exerts sufficient pressure to withstand the cocoon's pressure. This collimation shock will then separate the jet in a shocked and unshocked region, and has a Lorentz factor $\Gamma_{\rm cs} \sim 1/\theta_j$. The unshocked region eventually converges onto the jet's axis, and after that only the shocked jet remains, maintaining a constant cylindrical radius. The location where the jet becomes cylindrical is the collimation shock radius $r_{\rm cs}$ and its location at a time t is given by [11, 160]

$$r_{\rm cs} = \left(\frac{L_j^3 t^4}{c^5\theta_j^2\rho_a^3}\right)^{1/10} \left(\frac{6\xi_h\xi_c^2}{\pi^{3/2} f_{\rm cc}\xi_a}\right)^{1/5}. \tag{4.2}$$

The formula shown above is obtained for a constant cocoon pressure, but cases in which a pressure gradient exists are treated in Ref. [11]. As for the jet head, its velocity β_h is given by [11, 160]

$$\beta_h = \left(\frac{L_j}{c^5 t^2 \varrho_a \theta_j^4}\right)^{1/5} \left(\frac{16\xi_a}{3\pi\xi_h\xi_c^2}\right)^{1/5}, \tag{4.3}$$

which can be used to find the jet head's position r_h as a function of time.

We will assume that CR production and acceleration happens in the internal shocks, when a fast shell with Lorentz factor Γ_r collides with a slower one of Γ_s to form a merged shell of Γ_j. In the scenario shown by Fig. 4.1, the internal shock radius $r_{\rm is}$ is inside the

uncollimated jet ($r_{\rm is} \leq r_{\rm cs}$). We will assume that in LP GRB jet case $r_{\rm is} = r_{\rm cs}$

The internal shocks may be radiation mediated or radiation unmediated. When the shock is radiation mediated, photons in the downstream region may enter the upstream region. Inside this region, photons are thermalized by Compton scatterings with the thermal electrons and these electrons will then decelerate the ambient protons. If the protons decelerate over a distance that is shorter than the size of the upstream flow, then CR cannot be accelerated efficiently [14]. We quantify this condition by using the Thomson depth in the upstream region [14]

$$\tau_T^u = n_u \sigma_T l_u, \tag{4.4}$$

where n_u is the number density of the upstream region, σ_T is the Thomson cross section and l_u is the size of the upstream region. For the calculations, that follow, it is also useful to define the isotropic-equivalent total luminosity $L_{\rm tot} = 4L_j/\theta_j^2$, which is the luminosity of the source if its emission extended over all directions. Similarly, the isotropic-equivalent kinetic luminosity is $L_{\rm iso} = \Gamma_j L_{\rm tot}/\eta$, where η is the maximum Lorentz factor and Γ_j is the pre-collimated jet Lorentz factor.

Imposing the condition $\tau_T^u \lesssim 1$ to this region as the most conservative bound, we get $n'_u \sigma_T (r_{\rm is}/\Gamma_r) \lesssim 1$, where σ_T is the Thomson cross section and $n'_u \approx L_{\rm iso}/(4\pi r_{\rm is}^2 \Gamma_j^2 m_p c^3 \Gamma_{\rm rel-is})$ is the comoving upstream electron density, assuming an $e-p$ plasma. Here Γ_r is the Lorentz factor of the faster shell and $\Gamma_{\text{rel-is}} \approx \Gamma_r/(2\Gamma_j)$ is the relative Lorentz factor between the merged shell and the fast shell (assuming fast and slow shell both have the same mass). In terms of the LP GRB parameters, the radiation constraint [14] takes the form [1]

$$L_{\rm iso,52} r_{\rm is,10}^{-1} \Gamma_{j,2}^{-3} \lesssim 8.5 \times 10^{-3}\ \min[\Gamma^2_{\rm rel-is,0.5}, 0.32 C_1^{-1} \Gamma^3_{\rm rel-is,0.5}], \tag{4.5}$$

where $C \simeq 10$ is a numerical factor due to the generation of pairs at the shock. For this work, we ignore high-energy neutrino emission produced by CRs accelerated at collimation shocks, as these neutrinos would be more important in the GeV-TeV region [14].

Eq. (4.5) marks the location where efficient CR acceleration begins [14]. For successful CR injection, we need to ensure that the radiation constraint is satisfied before the jet ends at $t_{\rm dur}$ (that is the GRB duration). In general, $t_{\rm dur}$ is a free parameter; it becomes constrained by imposing the jet stalling (failed GRB) condition, namely that the breakout time $t_{\rm bo}$ (when the jet head reaches the stellar radius) is longer than $t_{\rm dur}$. For LP GRBs,

[1] There is a small difference in numerical values because $\sigma_T \sim 10^{-24}$ cm^2 is used in Eqs. (4) and (5) Ref. [14]. In this work we use $\sigma_T \approx 6.65 \times 10^{-25}$ cm^2.

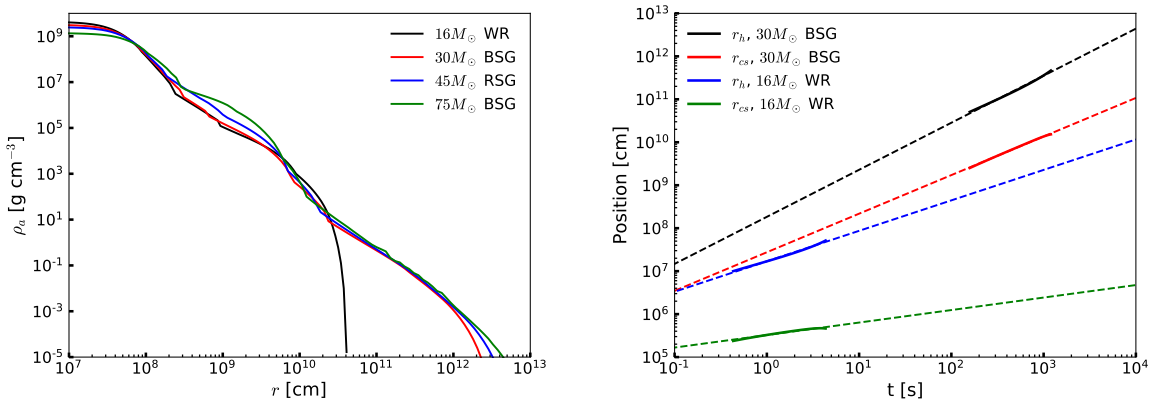

Figure 4.2. Left panel: Progenitor density profiles from [12]. Right panel: Jet head location r_h and collimation shock radius $r_{\rm cs}$ as a function of time. The solid lines correspond to the points obtained from Eq. (4.2) and Eq. (4.3), while the dashed lines are the associated extrapolations.

this is achieved for a nonrelativistic jet head; it will also move at a near constant velocity. We use these relations to verify that the chosen GRB parameters and density profile form bursts with the desired properties.

Results of the semianalytical jet propagation model are shown in Fig. 4.2. We choose three density profiles from [12]: a 30 $M_\odot$ and $75M_\odot$ blue supergiant (BSG) and a 45 $M_\odot$ red supergiant (RSG). We also include a 16 $M_\odot$ Wolf-Rayet (WR) profile from [175]. The radius r_h is calculated using Eq. (4.3) until we reach the point where the density profile falls off faster than r^{-3}. Beyond this point, we extrapolate to determine r_h. We then calculate $r_{\rm cs}$ in a similar fashion, using Eq. (4.2).

4.3 Choked SGRB jets in merger ejecta

For a neutron star merger, we follow the method outlined in Ref. [176] and consider the jet propagation in the merger ejecta with mass $M_{\rm ej}$ and speed $\beta_{\rm ej}$. For more detailed numerical studies see, e.g., Ref. [177]. Jets can be launched through the Blandford-Znajek mechanism [178] and can lead to neutrino emission by CRs accelerated at internal shocks.

We consider a time lag between the ejecta and jet production, which is given by $t_{\rm lag}$, such that the ejecta radius is

$$R_{\rm ej} = c\beta_{\rm ej}(t + t_{\rm lag}) \tag{4.6}$$

and the density profile of the ejecta is wind-like as

$$\varrho_{\rm ej} = \frac{M_{\rm ej}}{4\pi R_{\rm ej}^3}\left(\frac{r}{R_{\rm ej}}\right)^{-2}. \tag{4.7}$$

On the other hand, the jet head position is estimated to be

$$r_h \simeq 2.2\times10^{10}\ L_{\rm iso,51}^{1/3}\theta_{j,-0.52}^{-2/3}M_{\rm ej,-2}^{-1/3}\beta_{\rm ej,-0.48}^{1/3}t_{0.3}^{4/3}\chi_{\rm lag,0.18}\ {\rm cm}, \tag{4.8}$$

where $M_{\rm ej}$ is the ejecta mass and $\chi_{\rm lag} = 1 + t_{\rm lag}/t$. Again, CR acceleration occurs at the internal shock radius $r_{\rm is} \simeq 8.4\times10^9\ t_{\rm var,-4}\Gamma_{j,2.48}^2\Gamma_{\rm rel\text{-}is,0.6}^{-2}$ cm, where $t_{\rm var}$ is the variability time. Internal shocks can form either in the precollimated jet or the collimated jet; however, the Lorentz factor in the collimated jet is so low that the shock will be radiation mediated. For this reason, as in the LP GRB case, we assume that internal shocks occur in the unshocked jet ($r_{\rm is} \le r_{\rm cs}$) where the radiation constraint reads

$$L_{\rm iso,51}r_{\rm is,10}^{-1}\Gamma_{j,2.48}^{-3} \lesssim 2.3\ \min[\Gamma_{\rm rel-is,0.5}^2, 0.32C_1^{-1}\Gamma_{\rm rel-is,0.5}^3]. \tag{4.9}$$

Finally, the jet stalling condition is imposed by $r_h < R_{\rm ej}$.

4.4 CR injection, timescales and neutrino production

CRs are initially injected as an $dN_p'/d\varepsilon_p' \propto \varepsilon_p'^{-2}$ proton spectrum, where the primes indicate that the quantities are evaluated in the comoving frame of the injection site (i.e., in the rest frame of the jet). The minimum proton energy is $\Gamma_{\rm rel\text{-}is}m_pc^2$. Protons have a characteristic cooling time $t_{\rm cool}'$, which should not be shorter than the acceleration time $t_{p,\rm acc}' = \varepsilon_p'/(eBc)$. By setting $t_{p,\rm acc}' = t_{\rm cool}'$, we can determine the maximum proton energy $\varepsilon_{p,\rm max}'$. The energy injection rate is equal to $\epsilon_pL_{\rm iso}$, where ϵ_p is the fraction of $L_{\rm iso}$ carried by protons. We thus have

$$dN_p'/d\varepsilon_p' = \frac{\epsilon_pL_{\rm iso}}{\ln(\varepsilon_{p,\rm max}'/\varepsilon_{p,\rm min}')}\varepsilon_p'^{-2}\exp\left(\frac{\varepsilon_p'}{\varepsilon_{p,\rm max}'}\right). \tag{4.10}$$

Protons will create pions through $p\gamma$, with characteristic timescale $t_{p\gamma}$ given by Eq. (3.21). Additionally pp collisions may occur with a characteristic timescale $t_{pp}' = (\kappa_{pp}\sigma_{pp}n_{\rm j}'c)^{-1}$. We take $\kappa_{pp}\sim0.5$ as a constant, while the inelastic pp cross section σ_{pp} is parametrized by the formula given in Ref. [179].

To calculate both timescales, we need to specify the target photon (proton) density for $p\gamma(pp)$ timescales, with all quantities being calculated in the jet rest frame. In pp collisions, the target protons are at rest, with density $n'_j = L_{\rm iso}/(4\pi\Gamma_j^2 r_{\rm is}^2 m_p c^3)$.

For the target photons, we first consider the thermal component which is generated by the collimation shocks. For choked LP GRB jets, we use

$$kT'_{\rm cj} \simeq 0.70\ L_{\rm iso,49.5} r_{\rm cs,11.5}^{-1/2} (\theta_j/0.2)^{1/2} {\rm keV}. \tag{4.11}$$

In the case of choked SGRB jets, the thermal photons have a temperature

$$kT'_{\rm cj} \simeq 9.7\ \theta_{j,-0.52}^{1/2} M_{\rm ej,-2}^{1/4} \beta_{\rm ej,-0.48}^{-1/4} t_{\rm dur,0.3}^{-3/4} \chi_{\rm lag,0.18}^{-1/4} keV. \tag{4.12}$$

Note that in both cases, these temperatures are given in the collimation shock frame. To obtain the photon density in the jet frame where $p\gamma$ collisions take place, we apply a Lorentz boost of $\Gamma_{\rm rel-cs} \approx \Gamma_j/(2\Gamma_{\rm cs})$. In addition, the photons have to diffuse across a region with optical depth $\tau_{\rm cj} \sim n'_{\rm cj}\sigma_T r_{\rm cs}\Gamma_{\rm cj}$, where $n'_{\rm cj} \approx \Gamma_{\rm rel,cs} L_{\rm iso}/(4\pi\Gamma_j^2 r_{\rm cs}^2 m_p c^3)$ is the density in the collimated jet [14]. This modifies the target photon density by a factor $\Gamma_{\rm rel-cs}[1-\exp(-\tau_{\rm cj})]/\tau_{\rm cj}$. With these two modifications, we can obtain $dn'_\gamma/d\varepsilon'_\gamma$ to be used in Eq. (3.21).

We also have a non-thermal photon component. Non-thermal electrons are initially produced at the internal shock. A fraction ϵ_e of the thermal photon energy can be transferred to these electrons via photon-electron couplings and is then radiated as a non-thermal photon spectrum. We can describe this photon distribution by a broken power law $dn_\gamma/d\varepsilon_\gamma \propto \varepsilon_\gamma^{-\alpha_1}(\varepsilon_\gamma^{-\alpha_2})$ for $\varepsilon_\gamma < \varepsilon_{\gamma,\rm pk}(\varepsilon_\gamma > \varepsilon_{\gamma,\rm pk})$, normalized such that its total energy is $U_{\gamma,\rm NT} = \epsilon_e(\Gamma_{\rm rel\text{-}is}-1)n'_{\rm is}m_p c^2$, where $n'_{\rm is} \approx L_{\rm iso}/(4\pi\Gamma_j^2 r_{\rm is}^2 m_p c^3)$ is the downstream density of the internal shocks. We assume that the minimum (maximum) photon energy of the non-thermal component is 0.1 eV (1 MeV) and the spectral indices are $\alpha_1 = 0.2$ and $\alpha_2 = 2.0$ [176].

Using the interaction timescales $t_{pp/p\gamma}$, we can define the effective optical depth as

$$f_{p\gamma} + f_{pp} = t'_{\rm cool}(t'^{-1}_{p\gamma} + t'^{-1}_{pp}), \tag{4.13}$$

The calculation of $t'_{\rm cool}$ used to calculate $\varepsilon'_{p,\rm max}$ in Eq. (4.10) and the effective optical depth is done via Eq. (3.22). For protons, we consider adiabatic cooling with timescale $t'_{\rm ad} \approx t'_{\rm dyn} \approx r_{\rm is}/c\Gamma_j$ and synchrotron losses with timescale $t'_{\rm syn}$ given by Eq. (3.16). The calculation of $t'_{\rm syn}$ also requires the magnetic field strength B' in the comoving frame.

We assume that a fraction ϵ_B of the isotropic luminosity is converted to magnetic field energy, such that B' satisfies the relation

$$\epsilon_B = \left(\frac{B'^2}{8\pi}\right)\left(\frac{L_{\rm iso}}{4\pi r_{\rm is}^2 \Gamma_j^2 c}\right)^{-1}. \tag{4.14}$$

The expressions (4.10)-(4.13) provide the information about the initial proton spectrum and how efficient pp and $p\gamma$ are at producing pions. Pions produced from these processes will lose energy as they propagate and may not be able to decay into high-energy neutrinos. The same applies for muons. The relevant processes for these particles are adiabatic losses, synchrotron cooling and hadronic cooling. The first two are handled in the same way as the protons, but using their respective particle masses. For hadronic cooling, we use the timescale $t'^{-1}_{\pi p} = \kappa_{\pi p}\sigma_{\pi p} n'_j c$ where we take the values $\kappa_{\pi p} \sim 0.8$ and $\sigma_{\pi p} \sim 5 \times 10^{-26}$ cm^2 as constants for our energy range of interest. We assume that $t_{\mu p} = t_{\pi p}$.

The pion and muon cooling timescales are compares against their decay timescales $t'_{\rm dec} = \gamma \tau_{\rm dec}$, where γ is the Lorentz factor of the particle in the comoving frame, leading to a suppression factor $f_{\rm sup} = 1 - \exp(-t'_{\rm cool}/t'_{\rm dec})$. For neutrinos originating from muon decay, we require two suppression factors: one for pion cooling and another for muon cooling. The muon spectrum is therefore significantly suppressed with respect to the pion spectrum at high energies.

We assume that the correspondence between the parent proton and daughter neutrino is $\varepsilon'_p \approx 20\varepsilon'_\nu (\varepsilon'_p \approx 25\varepsilon'_\nu)$ for $p\gamma(pp)$ interactions. In reality neutrinos from a proton with ε'_p may have energies below $0.05\varepsilon'_p$ (or $0.04\varepsilon'_p$) due to meson and muon cooling. Meson and muon cooling modifies neutrino injection fluxes at high energies, while the production efficiency factors $f_{pp/p\gamma}$ modify the low-energy regions. Once we take these considerations into account, the generated neutrino spectrum "per flavor" in the jet frame is given by

$$\varepsilon'^{\,2}_\nu \frac{dN'_\nu}{d\varepsilon'_\nu} \approx \frac{K}{4(1+K)} \varepsilon'^{\,2}_p \frac{dN'_p}{d\varepsilon'_p} f_{\rm sup}(f_{p\gamma} + f_{pp}) \tag{4.15}$$

where $K = 1$ ($K = 2$) for $p\gamma$ (pp) interactions, $f_{\rm sup} = f^\pi_{\rm sup}$ for the ν_μ spectrum arising from pion decay and $f_{\rm sup} = f^\pi_{\rm sup} f^\mu_{\rm sup}$ for the neutrinos produced as a result of muon decay. After we obtain the neutrino fluxes in the jet comoving frame, we perform an appropriate Lorentz boost to switch to the observer frame. LP GRB neutrinos are injected at r_h, while SGRB neutrinos are injected at $r_{\rm is}$.

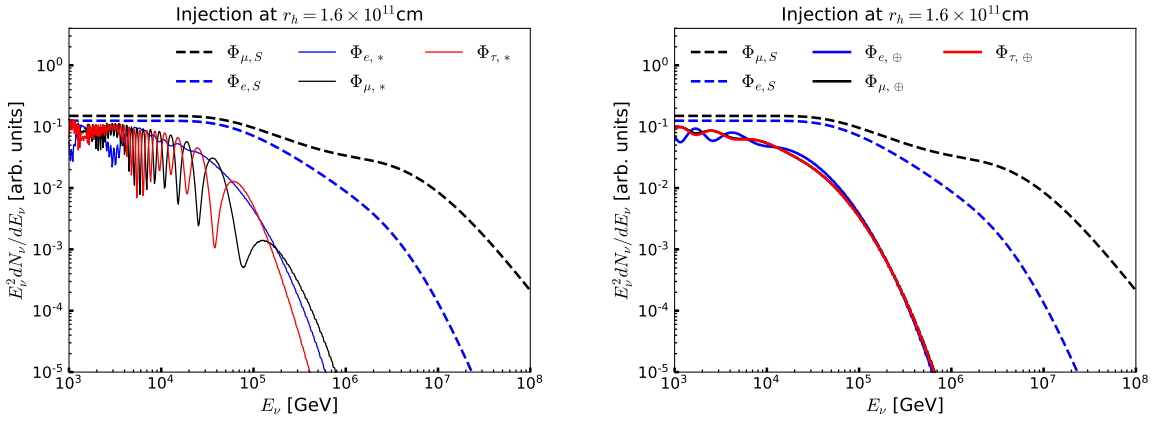

Figure 4.3. Neutrino energy spectrum from a choked LP GRB jet inside a BSG. Left panel: Neutrino spectrum after propagating from the injection site, $r_{\rm h} = 1.6 \times 10^{11}$ cm, to edge of the source. Right panel: Same as left panel, showing the flux arriving at Earth after averaging out due to long distance propagation. The proton flux is normalized such that $E_p^2 dN_p/dE_p = 1$. The $\nu_\alpha + \bar{\nu}_\alpha$ spectra at injection are represented by the dashed curves, combining contributions from π and μ decay after accounting for cooling.

4.5 Neutrino propagation

For neutrino propagation, we assumed the NuFIT 2019 NO oscillation fit values [180]. The effects of $\delta_{\rm CP}$ are expected to be nonsignificant compared to other considerations in neutrino production, namely the π^+/π^- ratio and kaon production [181, 182]. Without these considerations, there is little benefit in making a distinction between neutrinos and antineutrinos. We therefore treat the injection flux $\Phi_\nu + \Phi_{\bar{\nu}}$ as if it contained neutrinos and no antineutrinos and set $\delta = -\pi/2$ [183].

For resonance effects inside the source, we use the following estimate for the $\nu_1 - \nu_3$ resonance energy ε_R^H [124]:

$$\varepsilon_{\nu R}^H \approx \frac{\Delta m_{31}^2 \cos 2\theta_{13}}{2\sqrt{2} G_F n_e} = \frac{32\text{GeV}}{(\rho/\text{g cm}^{-3})} \tag{4.16}$$

The right hand side of Eq. (4.16) uses the best fit values of the oscillation parameters and $n_e = Y_e \rho / m_p c^2$, where ρ is the matter density, m_p is the proton mass and Y_e is the electron fraction. The electron fraction is assumed to be 1/2 both in Eq. (4.16) and our numerical simulations.

During propagation, NC interactions are considered as they contribute to neutrino attenuation, but not oscillations (see discussion above Eq. (2.15)). For CC interactions, we are not tracking the charged leptons formed in the process since they will have less

energy than the incident neutrino and will also be quickly cooled, particularly the electron. The propagation from the injection radius to R_* (or to $R_{\rm ej}$ for SGRBs) is handled by nuSQuIDS [184], giving the oscillated spectra $\Phi_{\nu_\alpha,*}$ at the progenitor's surface. In the SGRB case, we have to keep in mind that the ejecta radius and density profile are time dependent quantities, in the sense that both the location of the neutrino and time elapsed since injection have to be used to impose the neutrino escape condition.

After escaping the source, wave packet decoherence will cause subsequent vacuum oscillations to be suppressed as neutrinos make their way to Earth. The observed flavor flux $\Phi_{\nu_\alpha,\oplus}$ is found via

$$\Phi_{\nu_\alpha,\oplus} = \sum_i |U_{\alpha i}|^2 \Phi_{\nu_i,*}, \tag{4.17}$$

where $\Phi_{\nu_i,*}$ is the neutrino flux of the vacuum mass eigenstate i [124] at the edge of the progenitor. This expression is a variant of Eq. (2.14).

4.6 Results on neutrino oscillation and flavor ratios at Earth

The parameter set used for LP GRBs is shown in Table 4.1 and the density profile corresponds to a 30 solar mass blue supergiant (BSG) from Ref. [12]. By taking a variety of injection radii, we obtain the propagated spectra both at escape and on the Earth. Our choice of parameters indicate that efficient CR acceleration happens at $r_{\rm cs} \sim 5.9 \times 10^8$ cm at ~ 10 s and breakout at ~ 4600 s. Based on previous studies, which obtained the $E_\nu^2 dN_\nu/dE_\nu$ flux peak in the 100 TeV range [14,185], we will study the spectrum in the 1 TeV - 100 PeV energy range. Throughout this energy range, pion production is highly efficient. Using Eq. (4.16), we find that, at the injection site, $E_R^H \approx 6$ MeV when the shock becomes radiation unmediated and $E_R^H \approx 160$ TeV at $t_{\rm dur}$.

We show the oscillated neutrino spectra in Fig. 4.3, with proton fluxes normalzied such that $\varepsilon_p^2 dN_p/d\varepsilon_p = 1$. The observed oscillation pattern for our injection radius of 1.6×10^{11} cm is not a mere result of the MSW resonance: the $\nu_1 - \nu_3$ resonance occurs at < 430 GeV at injection, below the energy range of interest. During propagation, we can satisfy the resonance condition in the TeV range, which may explain the peaks at 1 TeV and 3 TeV in the ν_e flux. What we observe are nonadiabatic oscillations, in which oscillations are caused by the $\nu_2 - \nu_3$ mixing in matter induced by adiabaticity breaking of the $\nu_1 - \nu_3$ resonance, the so-called H-wiggles mentioned in Ref. [124], whose effect decreases as we go to energies above 10 TeV.

Choked LP GRB jet parameters

$L_{\rm iso,48}$	θ_j	Γ_j	$t_{\rm dur}$	ϵ_B	$r_{\rm is}$	$\Gamma_{\rm rel\text{-}is}$	ϵ_p
1	1.0	50	1800 s	0.1	$r_{\rm cs}$	4	0.2

Choked SGRB jet parameters

$L_{\rm iso,51}$	θ_j	Γ_j	$t_{\rm dur}$	ϵ_B	$r_{\rm is}$
1	0.3	300	1.8 s	0.1	8.4×10^9 cm
$\Gamma_{\rm rel\text{-}is}$	ϵ_e	ϵ_p	α_1	α_2	$\varepsilon_{\gamma,\rm pk}$
4	0.1	0.2	0.2	2	1.7 keV

Table 4.1. Relevant parameters assumed for our choked LP GRB and choked SGRB models. For the special case of SGRBs, we have the additional parameters $M_{\rm ej} = 0.02 M_\odot$, $\beta_{\rm ej} = 0.33$ and $t_{\rm lag} = 1$ s.

In the high-energy regime, we observe the attenuation of the neutrino flux as a result of both pion/muon cooling and the increase in the CC cross section. The effect of NC interactions slightly modifies the slope of the spectrum and we found that the changes are in the order of 10%. Naturally, the attenuation effects become more significant at lower injection radii; if injection occurs at 10^{10} cm, we would have negligible flux at 1TeV.

On the other hand, at high energies, matter effects enhance the mass splittings inside the progenitor, effectively suppressing oscillation effects. This phenomenon typically occurs in the PeV range. If we consider the propagation close to the edge of the progenitor, where the density is the smallest, we would still find little oscillations because the vacuum oscillation lengths $l_{jk}^{\rm osc} = 4\pi E_\nu / |\Delta m_{jk}^2| \gtrsim 10^{14}$ cm are much larger than the progenitor radius.

Looking at the flavor ratios, it is traditionally assumed that the neutrino spectrum at escape (for $p\gamma$ interactions) follows the ratio $(\nu_e : \nu_\mu : \nu_\tau) = (1 : 2 : 0)$ at escape for low energies and $(0, 1, 0)$ at high energies [186]. Under vacuum neutrino oscillations and Eq. (4.17) takes the form

$$\Phi_{\alpha,\oplus} = \sum_i |U_{\alpha i}|^2 |U_{\beta i}|^2 \Phi_{\beta,*}, \tag{4.18}$$

which is essentially Eq. (2.14) and leads to the flavor ratios $(1 : 1.08 : 1.06)$ for low energies and $(1 : 2.03 : 1.87)$ at high energies. In our case, we inject neutrinos inside the source so matter effects will alter the low-energy ratio. We show the flavor ratios for our model in Fig. 4.4. We see that nonadiabatic oscillations shown in Fig. 4.3 also induce oscillations in the flavor ratios.

One feature that still persists even in the presence of matter effects is that Φ_{ν_μ} and Φ_{ν_τ}

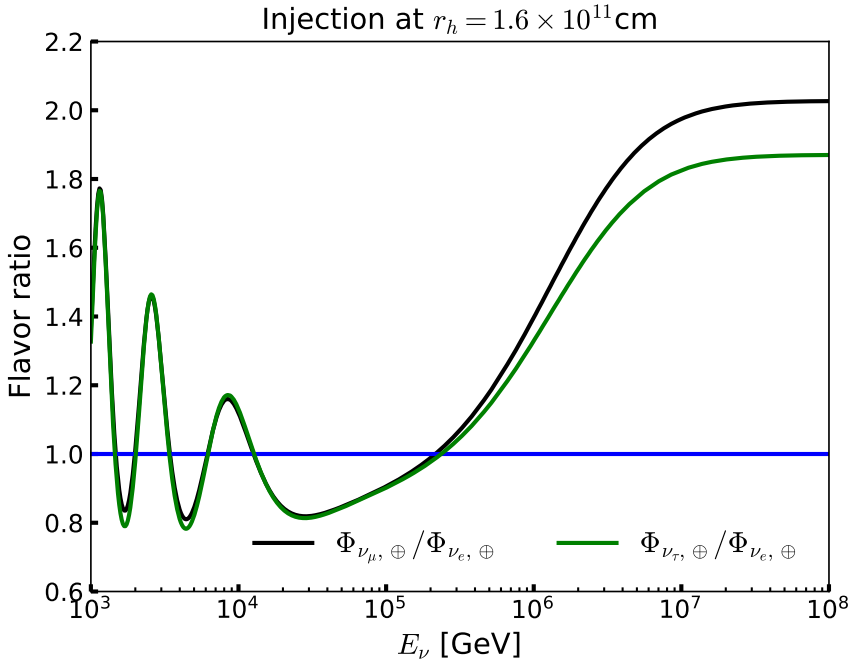

Figure 4.4. Observed $\Phi_{\nu_\alpha}/\Phi_{\nu_e}$ flavor ratios at Earth. Neutrino spectra are injected at $r_{\rm h} = 1.6 \times 10^{11}$ cm. The blue line is a line for the (1:1) ratio and is added as a reference.

fluxes are approximately equal after averaging, for low E_ν. The transition in the flavor ratio and the splitting between the ν_μ and ν_τ fluxes occurs close to 100 TeV, consistent with our theoretical expectation that the ratio approaches $(1 : 2.03 : 1.87)$ when muons are significantly cooled in the GRB. This transition would be hard to spot since the neutrino flux is heavily suppressed at these energies due to inelastic collisions with matter. Additional simulations using a 25 and 35 solar mass BSG (all other parameters fixed) show that the flavor ratio is only mildly affected by choosing different BSG progenitor models. Similar results hold for a red supergiant progenitor as well. We expect this because most of the neutrino injection happens above 10^{11} cm, where the density profiles are similar (see Fig. 4.2).

Upon time integration up to $t_{\rm dur} = 1800$ s, the flavor ratio oscillations get smeared. This can be seen in Fig. 4.5, where the oscillations in ν_e are less prominent. In the 1 TeV - 10 TeV range, some flavor ratio oscillations remain, with slightly more ν_μ and ν_τ than ν_e. In the 10 TeV - 100 TeV range we see that the ν_e excess can enhance the shower to track ratio, which could alleviate the tension between the shower and muon data (see Section IV.B). This excess that covers a wide energy range is present because the jet is choked and matter effects are important: as we increase $t_{\rm dur}$, more neutrinos are injected closer to the progenitor's edge and the fluence would approach the vacuum oscillation

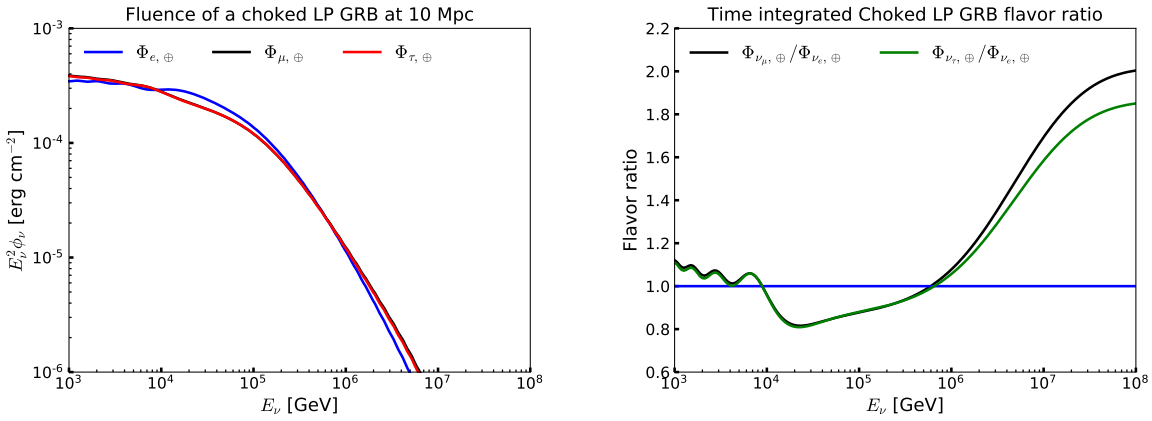

Figure 4.5. Left panel: Fluence of a choked LP GRB at a distance of 10 Mpc, using the parameters of Table 4.1. Right panel: Same as left panel, but showing the flavor ratio of the fluence.

limit. Strong neutrino attenuation starts around 100 TeV, while at 1 PeV muon cooling occurs and the flavor ratio approaches $(1 : 2.03 : 1.87)$.

In the case of a WR star progenitor, we have $\varrho_a > 10^3$ g cm^{-3} until $r \sim 10^{10}$cm. Neutrino attenuation is important and very few neutrinos are present in the TeV range, so the only contributions come from injection close to the edge. We thus conclude that most of the injected neutrinos would be subject to vacuum oscillation mostly. If we insist on having observable matter effects, attenuation would be so strong that attempting a fit with IceCube data would inevitably overshoot the astrophysical flux in the low-energy range. Furthermore, we also get a lower bound on the allowed values of $t_{\rm dur}$ if we are to have observable neutrinos. This restriction can be avoided if the WR star has additional surrounding material outside of its core, allowing for further jet propagation [137].

The parameters chosen for the choked SGRB jets are summarized in Table 4.1 and the resulting oscillation pattern is shown in Fig. 4.6. It is instructive to point out the oscillation pattern differences with respect to the LP GRB case. First, we find that the neutrino flux does not vary significantly over time; unlike LP GRBs, in which the injection begins at ~ 10 s, the constraint $r_{\rm is} < r_{\rm cj}$ forbids CR injection in the early phases, beginning at the neutrino onset time $t_{\rm onset} = 1.7$ s and the duration of the neutrino injection phase is shorter in SGRBs. The mild variations in the spectra mean that the oscillations patterns are not smeared out after time integration. The $\nu_1 - \nu_3$ resonance energy at the injection site occurs at 18 GeV at $t_{\rm onset}$ and 27 GeV at $t_{\rm dur}$.

The particular parameter set that we have chosen allows for an interesting pattern to form. In the LP GRB case, the oscillation lengths are shorter than the size of the progenitor, so oscillations in the flavor ratio could be observed early, at $t = 10^2$ s, but

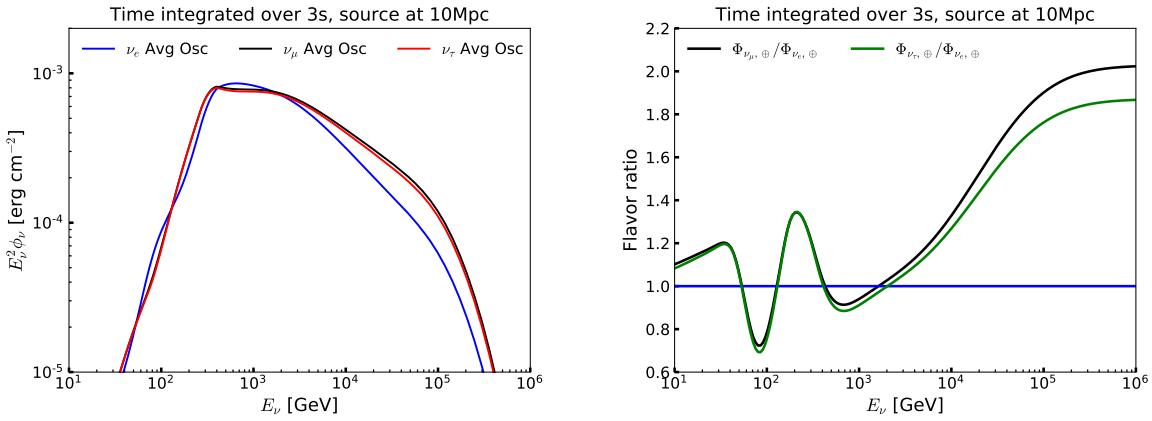

Figure 4.6. Left panel: Neutrino fluence from a failed SGRB at a distance of 10 Mpc. Contributions are integrated over $t_{\rm dur} = 3$ s. The neutrino injection rate varies mildly over time. Right panel: Same as left panel, but showing the neutrino flavor ratio instead of the fluence.

get smeared out when integrating over $t_{\rm dur}$. In the SGRB case, such flavor oscillations occur between 100 GeV and 1 TeV, which is advantageous because we can observe in Fig. 4.6 a $\sim 10\%$ ν_e excess over $\nu_{\mu/\tau}$ that persists through a wide energy range after time integration. Resonance happens at $\mathcal{O}(10)$ GeV, outside our range of interest. We also show the flavor ratio in Fig. 4.6, showing the ν_e excess at 1TeV. In principle, such an excess could be observed by IceCube over the 500 GeV - 30 TeV energy range.

4.7 Detectability of individual bursts with next-generation detectors

It is useful to see if our predictions can be tested in future detectors such as IceCube-Gen2 and KM3Net. In the case of an ideal detector, for instance IceCube-Gen2, we estimate the number of events as

$$\mathcal{N} = \int_{E_{\nu,\rm min}}^{E_{\nu,\rm max}} dE_\nu \mathcal{V}(\varrho_{\rm ice} N_A) \sigma(E_\nu) \phi_\nu \tag{4.19}$$

where $\sigma(E_\nu)$ is the neutrino-nucleon cross section, ϕ_ν is the (time integrated) neutrino fluence, $\varrho_{\rm ice}$ is the ice density, $\mathcal{V} = 10$ km^3 is the detector volume and N_A is the Avogadro's constant. From an experimental point of view, it is often more meaningful to calculate the number of events as a function of the deposited energy. The energy deposited in the detector will depend on the neutrino flavor and on the neutrino topology. In our case,

Choked LP GRBs		
	$E_{\rm dep} > 1$ TeV	$E_{\rm dep} > 10$ TeV
Shower	88	25
	(120)	(47)
Track	28	5
	(40)	(12)

Choked SGRBs		
	$E_{\rm dep} > 1$ TeV	$E_{\rm dep} > 10$ TeV
Shower	65	10
	(124)	(19)
Track	22	3
	(123)	(28)

Table 4.2. Expected number of events in IceCube-Gen2-like detectors as a result of a single choked LP GRB or choked SGRB jet that occurs at a distance of 10 Mpc, over the duration $t_{\rm dur}$ and assuming that the jet points towards us. We use the parameters in Table 4.1 and, in the case of a choked LP GRB, we use a 30 $M_\odot$ progenitor. The event numbers are shown for two different thresholds in deposited energy. The quantities in brackets correspond to the event numbers without attenuation and oscilation.

we consider fully contained events for both showers and tracks. Inclusion of partially contained events depends on selection criteria, which are not discussed in this work.

We use the neutrino-nucleon cross sections in Ref. [187]. The relevant shower/track channels are listed in Ref. [63] and the deposited energy $E_{\rm dep}$ for each channel is given as functions of the neutrino energy E_ν and the mean inelasticity $\langle y \rangle$, where the latter is obtained from Ref. [187]. We compute the event numbers using the fluxes calculated in our work (referred to as "with attenuation and oscillation"), as well as the fluxes obtained if we ignore matter effects and radiation constraints, while assuming that neutrino production is constant in time (i.e., we calculate the flux at $t_{\rm dur}$ and multiply this result by $t_{\rm dur}$ to find the time integrated fluence). We will refer to the latter scenario as the case "without attenuation and oscillation".

For both our sources, we used the parameters in Table 4.1. The results are summarized in Table 4.2, where event numbers with $E_{\rm dep} > 1$ TeV and $E_{\rm dep} > 10$ TeV are presented. Since $t_{\rm dur} \sim 1000$ s, the expected number of background events is less than one.

In choked LP GRB jets, we see that the difference is less than a factor of 2 between the case with attenuation and oscillation and the one without. This comes from matter attenuation. The feature becomes more prominent as we increase the energy threshold for $E_{\rm dep}$ (see blue curve in Fig. 4.7).

In the case of choked SGRB jets, we notice that a scenario without attenuation and

oscillation overestimates the total number of events by a factor of ~ 2. By ignoring the time dependence of the problem, this case assumes neutrino emission throughout $t_{\rm dur}$, but the constraint $r_{\rm is} < r_{\rm cs}$ reduces this time interval by about 1/2. Without matter attenuation effects, we also overestimate the flux and this overestimation increases with energy. In terms of flavor ratios, we observed that the percentage of shower events increased significantly compared to the number of track events and is a feature that persists for all $E_{\rm dep} > 1$ TeV. This is caused by the $\nu_\mu \to \nu_e$ conversion above 1 TeV, reducing the number of track events, while increasing shower events. In the absence of matter effects, the ν_e flux is below $\nu_{\mu/\tau}$ flux at all energies, causing shower and track event numbers to be comparable. Note that the non-detection of neutrinos from GRB 170817A is consistent with our model, because the SGRB jet was off-axis, preventing us from making stringent constraints from this particular event.

4.8 Choked LP GRB jet contribution to the diffuse neutrino flux

We test the possibility of our oscillated neutrino spectra to match IceCube's unfolded diffuse neutrino spectrum with six years of shower data [1] and six years of high energy starting event (HESE) data [13]. In particular, the origin of medium-energy neutrinos has been of interest, because the multi-messenger analyses have indicated that the sources are hidden CR accelerators [188, 189], which include choked GRB jets [14, 190] and cores of active galactic nuclei [191, 192].

We probe the $L_{\rm iso} - \Gamma_j$ space, keeping all other parameters and the progenitor model fixed. Our spectrum is time averaged, from the time that CR acceleration becomes efficient (see Eq. (4.5)) to $t_{\rm dur}$. The normalization is left as a free parameter; we optimize it to provide a best fit to the unfolded spectrum between 10 TeV and 100 TeV. Exploration of the parameter space is limited by the requirement $t_{\rm dur} < t_{\rm bo}$ and that efficient acceleration has to occur before breakout.

For this work, the normalization is set by an energy constraint that relates the total extragalactic diffuse flux to the GRB rate density as

$$E_\nu^2 \Phi_\nu \;\sim\; 4 \times 10^{-8}\ {\rm GeV\ cm^{-2} s^{-1} sr^{-1}} \epsilon_p \times \mathcal{E}_{k,51} \left(\frac{f_{\rm cho} \rho}{1000\ {\rm Gpc^{-3} yr^{-1}}} \right) \left(\frac{f_z}{3} \right),$$

where $\mathcal{E}_k = L_{\rm iso} t_{\rm dur}$ is the isotropic-equivalent kinetic energy, f_z is the redshift evolution

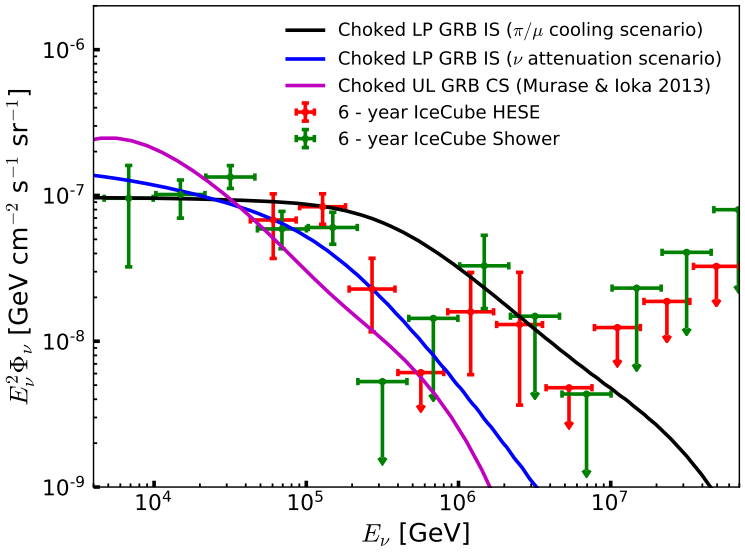

Figure 4.7. All-flavor choked LP GRB diffuse neutrino fluxes in comparison with the IceCube astrophysical neutrino spectra. The data from the 6-year shower analysis [1] is shown by the green bars, while the result of the 6-year HESE analysis [13] is shown by the red bars. The per-flavor neutrino flux from [13] was multiplied by a factor of 3 to estimate the all flavor flux. The π/μ cooling scenario uses $L_{\rm iso,48} = 2, \Gamma_j = 70, \theta_j = 0.2, t_{\rm dur} = 2000$ s and a 75 $M_\odot$ BSG progenitor, while the ν attenuation scenario assumes $L_{\rm iso,48} = 1, \Gamma_j = 50, \theta_j = 1, t_{\rm dur} = 1800$ s and a 30 $M_\odot$ BSG progenitor. The remaining parameters are given in Table 4.1. For comparison, we show the spectrum of the choked UL GRB neutrinos from the collimation shock (CS) in Ref. [14] but the flux is rescaled.

factor [145, 193], ϵ_p is the energy fraction carried by CR protons, ρ is the local rate density of successful LP GRBs, and $f_{\rm cho}$ is the fraction of choked GRB jets compared to the successful ones. LP jets are preferred not only theoretically to satisfy the radiation constraints and jet stalling condition, but also observationally to be consistent with the IceCube data. The failed LP GRB rate density should be above ~ 60 Gpc^{-3} yr$^{-1}(f_z/3)^{-3}$ because a lower rate density contradicts the nondetection of multiplet sources [194–197].

We find that our LP GRB jet parameters can explain the medium-energy neutrino data, which is consistent with the results of Ref. [14]. Ref. [198] had difficulty in explaining the 10-100 TeV data but their parameter space is different. We show in Fig. 4.7 the result with $L_{\rm iso,48} = 1$, $\Gamma_j = 50$, $t_{\rm dur} \approx 1800$ s, $\theta_j = 1$ and $(\rho/1000\ {\rm Gpc}^{-3}\ {\rm yr}^{-1}) f_{\rm cho} \sim 20$. By choosing a duration time smaller than the breakout time, we obtain a spectral cutoff due to the neutrino attenuation in the progenitor star, as expected in Ref. [14]. For a $75 M_\odot$ BSG, we choose the parameters $L_{\rm iso,48} = 2, \Gamma_j = 70, \theta_j = 0.2$ and $t_{\rm dur} \approx 2000$ s, in which the neutrino spectrum extends to the higher-energy regions. The associated rate

density is $(\rho/1000\ \mathrm{Gpc}^{-3}\ \mathrm{yr}^{-1}) f_{\mathrm{cho}} \sim 6$. In this case, neutrino attenuation is weak and the suppression is caused mainly by pion and muon cooling. We also point out that the neutrino flavor ratio is not exactly $\approx 1:1:1$ thanks to matter effects in the neutrino oscillation, and a ν_e excess is expected in the 10 – 100 TeV range. This could help us explain the diffuse neutrino flux suggested by the shower analysis is higher than that from the upgoing muon neutrino analysis.

In both of these cases, our models are not yet constrained by the stacking limits [172, 196, 199] as well as multiplet constraints [194–197]. Note that our LP GRB simulations are shown as the all-flavor diffuse neutrino fluxes; any possible flavor ratio oscillation in the low-energy region is smeared out by the summation over flavors, leaving neutrino attenuation as the relevant effect.

Chapter 5
Charm production in newborn magnetars

The work in this chapter was published in [115].

5.1 Introduction

Magnetars are neutron stars with the highest magnetic fields in the Universe [200–202]. The magnetar birth rate is expected to be more than $\sim 10\%$ of the CCSNe rate. While the fast-rotating magnetar event rate is unknown, it would not exceed the rate of Type Ibc SNe. For fast rotating magnetars with initial periods $P_i \sim 1$ ms at birth, one can expect magnetic fields as high as $10^{14} - 10^{16}$ G, due to the amplification of the field by a dynamo mechanism [203, 204], although a significant fraction of the magnetars may be explained by the fossil field hypothesis [205].

The rotational energy can be extracted in a form of Poynting energy and fast-rotating neutron stars or magnetars may provide a site for efficient UHECR acceleration [206]. These CRs do not escape the SN ejecta, instead losing their energy through pp and/or $p\gamma$ interactions, to secondary particles. Previous studies on neutrino production in magnetars mainly considered pion decays, [207–210] where the pions come from pp and $p\gamma$ interactions (but see also Ref. [211]). Here, we mainly focus on magnetar scenarios where pp interactions dominate at early times and in addition to pion decays, we also consider kaon decays and charmed hadron decays as neutrino sources. Typically, charm production in various astrophysical scenarios can be neglected because its production cross section is small when compared to pion/kaon production, but may not always be the case as considered for choked GRB jets [212, 213]. In magnetars, for energies above $\mathcal{O}(10^9)$ GeV, pions and kaons are subject to strong cooling due to interactions with

surrounding protons and photons, while charmed hadrons decay promptly without any significant energy loss. If sufficient cooling is present, prompt decays of charm hadrons can dominate the neutrino fluence at ultrahigh energies.

We will show that charm hadron contributions become important in the context of next generation detectors, such as IceCube-Gen2 [15], Probe Of Extreme Multi-Messenger Astrophysics (POEMMA) [214] and Giant Radio Array for Neutrino Detection (GRAND) 200k [17], which are sensitive to 10^9 GeV - 10^{11} GeV neutrinos.

In what follows, we assume that the UHECRs accelerated in newborn magnetars are protons, but nuclear composition has been considered in other works (e.g. Ref. [209]). We will consider nearby magnetars, so we consider $\varepsilon = E$. We evaluate neutrino injection rates from a given proton injection spectrum dN_p/dE_p by calculating the particle spectra of the chain $pp \to hX \to \nu Y$, where h is a hadron (pion, kaon and charmed hadron) that decays into neutrinos. The initial proton spectrum is a time-dependent function that depends on the magnetar's parameters, e.g., the magnetic field, radius, initial period, moment of inertia, efficiency of acceleration and shock velocity, as discussed later.

To determine the proton injection spectra, we start by considering properties of the magnetars and their mechanism for accelerating protons to high energies. The magnetar consists of a rapidly rotating neutron star, with an initial angular frequency $\Omega_i = 2\pi/P_i$ and initial period $P_i \sim 1$ ms. Neutron stars are known to spin down, and their rotational energy is carried by the wind, consisting of the outflowing plasma and magnetic fields. Charged particles are accelerated by tapping a fraction of the voltage available in the wind, via the wake-field acceleration mechanism [206].

The spindown luminosity at time t is given by

$$\begin{aligned} L(t) &= \frac{B_{\rm NS}^2 R_{\rm NS}^6 \Omega_i^4}{4c^3}(1+\sin^2\chi)\left(1+\frac{t}{t_{\rm sd}}\right)^{-2} \\ &\simeq 1.5\times 10^{50}{\rm erg\ s^{-1}}\, B_{\rm NS,15}^2 R_{\rm NS,6}^6 \Omega_{i,4}^4 \\ &\quad \times(1+t/t_{\rm sd})^{-2}\,, \end{aligned} \tag{5.1}$$

where χ is the angle between the rotation and magnetic axes. Note that the above formula based on magnetohydrodynamics simulations [215–217] is analogous to the well-known vacuum dipole formula. Our numerical values are obtained with $\langle \sin^2\chi\rangle = 2/3$.

From Eq. (5.1), it follows that for $t \gg t_{\rm sd}$, the luminosity will decrease as t^{-2} and does not depend on Ω_i, since the spindown time $t_{\rm sd}$ depends on Ω_i^{-2}. In particular, for a neutron star with magnetic field $B_{\rm NS}$, radius $R_{\rm NS}$ and moment of inertia I, the spindown

time is [218]

$$t_{\rm sd} = \frac{6Ic^3}{5\Omega_i^2 B_{\rm NS}^2 R_{\rm NS}^6} \simeq 10^{2.5}\,{\rm s}\ \ I_{45} B_{\rm NS,15}^{-2} R_{\rm NS,6}^{-6} \Omega_{\rm i,4}^{-2}. \tag{5.2}$$

As noted above, we assume a proton composition of cosmic rays, and for simplicity, we assume that all accelerated protons at t have a monotonic energy [206, 207]

$$\begin{aligned} E^M(t) &= \frac{f_{\rm acc} e B_{\rm NS} R_{\rm NS}^3}{2c^2}\Omega_i^2 \\ &\simeq 1.3\times 10^{13}\ {\rm GeV}\, f_{\rm acc,-1} B_{\rm NS,15} R_{\rm NS,6}^3 \Omega_{i,4}^2 \left(1+t/t_{\rm sd}\right)^{-1}, \end{aligned} \tag{5.3}$$

where $f_{\rm acc}$ parametrizes the efficiency of the acceleration process.

We assume that the proton injection rate is determined by the Goldreich-Julian rate [219], in which the proton injection rate spectrum at t is written as

$$\frac{dN_p}{dE_p} = \frac{B_{\rm NS} R_{\rm NS}^3 \Omega_i^2}{ec(1+t/t_{\rm sd})}\delta[E_p - E^M(t)], \tag{5.4}$$

which roughly gives

$$\begin{aligned} \frac{dN_p}{dE_p} &\sim 7\times 10^{39}\ {\rm GeV}^{-1}\ B_{\rm NS,15} R_{\rm NS,6}^3 \Omega_{i,4}^2 \\ &\quad (1+t/t_{\rm sd})^{-1}\delta[(E_p - E^M(t))/{\rm GeV}]. \end{aligned} \tag{5.5}$$

In the limit $t \gg t_{\rm sd}$, we see that $E^M(t) \propto t^{-1}$ and is independent of Ω_i. The time integration of dN_p/dE_p gives a proton time-integrated injection spectrum that scales as E_p^{-1} [207].

Magnetar-driven supernovae

At the birth of the magnetar, the SN ejecta propagates outward with speed $\beta_{\rm ej}c$. We estimate the SN ejecta radius as

$$r_{\rm ej} \approx \beta_{\rm ej} ct \simeq 10^{13.5}\ {\rm cm}\ \beta_{\rm ej,-1} t_4. \tag{5.6}$$

Although $\beta_{\rm ej}$ may depend on time, we assume time-independence for simplicity. The nucleon density in the ejecta is assumed to be homogeneous, such that $n_N = 3M_{\rm ej}/(4\pi r_{\rm ej}^3 m_p)$, where $M_{\rm ej}$ is the ejecta mass and m_p is the proton mass. We may assume that the SN ejecta masses typically lie between $10M_\odot$ and $35M_\odot$ [220].

Magnetar-driven merger novae

Rapidly rotating magnetars could be born at the merger of low-mass neutron star

binaries. A significant amount of the mass would be ejected during the merger by dynamical interactions and/or disk winds, with typical ejecta masses lying in the range $10^{-2}M_{\odot}$-$10^{-1}M_{\odot}$ [221]. In the merger case, the rotational energy can be used to accelerate the ejecta. Thus, the ejecta speed $\beta_{\rm ej}$ is time dependent in general, and is found by solving

$$\Gamma_{\rm ej}(\beta_{\rm ej})M_{\rm ej}c^2 = \Gamma_{\rm ej}(\beta_{\rm ej,0})M_{\rm ej}c^2 + \int_0^t L(t)dt, \tag{5.7}$$

where $\Gamma_{\rm ej}(\beta) = (1-\beta^2)^{-1/2}$ is the Lorentz factor of the ejecta. We then calculate the ejecta radius

$$r_{\rm ej}(t) = \int_0^t \beta(t')cdt', \tag{5.8}$$

which determines the time-dependent nucleon density n_N.

5.2 Hadronic spectrum

The time-dependent hadronic spectrum at the source is found via convolution of Eq. (3.3) with the proton injection rate:

$$\frac{dN_h}{dE_h}(E_h) = \int_{E_h}^{\infty} dE_p \frac{dN_p}{dE_p} F_{pp\to h}(E_h, E_p). \tag{5.9}$$

We include $h = \pi,\ K$ and charm hadrons $h = D^0, D^{\pm},\ D_s,\ \Lambda_c$. For charmed hadron production, we use the relation between differential energy distributions of the charm quark and charmed hadron (see, e.g., Ref. [222, 223]),

$$\frac{d\sigma}{dx_E}(x_E, E_p) = \int_{x_E}^1 \frac{dz}{z}\frac{d\sigma}{dx_c}(x_c, E_p)D_c^h(z), \tag{5.10}$$

where $x_c = E_c/E_p = x_E/z$, $d\sigma/dx_c$ is the $pN \to cX$ production cross section and D_c^h is the fragmentation function. The quantity x_E translates to the hadron energy by $E_h = x_E E_p$. We use the fragmentation function D_c^h of Kniehl and Kramer [30]. This fragmentation function was also used, for example, in the evaluation of the prompt atmospheric neutrino flux from charm in ref. [222, 223]. The fragmentation function includes the corresponding fragmentation fractions for charm quarks to fragment into D^+, D^0, D_s^+ and Λ_c^+, equal to the fragmentation functions for antiquarks to the corresponding antiparticle hadrons [31].

There are large uncertainties in the theoretical predictions of hadronic production of charm. The strong interaction corrections depend on powers of the strong coupling

constant, evaluated at characteristic energy scales comparable to the mass of the produced quark. The charm quark mass m_c, taken here to be 1.3 GeV, means that the theoretical uncertainties are large, even in the next-to-leading order (NLO) QCD evaluation in the collinear parton model [224–226].

Another source of uncertainty at high energies is the fact that the neutrino fluence from charm contributions depends on the small momentum fraction (small-x) parton distribution functions (PDFs), especially the gluon PDF, of relevance to evaluating $d\sigma/dx_E$ in Eq. (3.3). At these high energies, the values of x probed in the pp interactions are extremely small, beyond the range which was probed in the high energy accelerators. Thus the PDFs are largely unconstrained in this region and need to be extrapolated. One theoretical approach to small-x PDFs is the k_T-factorization framework [227–230] in its linear formulation that accounts for resummation of large logarithms $\ln(1/x)$, and in its non-linear formulation that also accounts for saturation effects [231] of the gluon density at very small-x.

In the results shown here, we perform a NLO QCD evaluation of $d\sigma/dx_c$ in the collinear approach. This is our central result, which is in reasonable agreement with SIBYLL after fragmentation is included. We also evaluate the differential cross section for charm production in the k_T factorization framework with linear and non-linear evolution of the gluon PDF density. Details are included in appendix . The result is that the span of predictions is a factor of $\sim 1/3 - 3$ of the central NLO QCD curve for most of the range of x_E values. This factor of $1/3 - 3$ uncertainty is represented by the shaded blue band in the results from charm shown below. We discuss the evaluation of the charmed hadron contribution in more detail in appendix .

Inside the ejecta, hadrons will interact with the ambient protons, leading to hadronic cooling. Since the magnetic field in the SN shock is weak, we neglect synchrotron losses. We account for hadronic cooling by comparing the cooling timescale $t_{\rm cl}$ to the decay timescale $t^h_{\rm dec} = E_h\tau_h/m_h$, where τ_h is the lifetime of the hadron. For example, the pion cooling timescale is given by $t_{\rm cl} \approx t_{\pi N} \approx (\kappa_{\pi p}\sigma_{\pi p} n_N c)^{-1}$, where $\sigma_{\pi p}$ is the pion-proton inelastic cross section and $\kappa_{\pi p}$ is the average inelasticity, and n_N is the nucleon density. We can then modify the hadronic injection rate with a cooling factor $1 - \exp(-t_{\rm cl}/t^h_{\rm dec})$. Analogous expressions are obtained for kaon and charmed hadron cooling timescales. The πp, Kp inelastic cross sections are obtained from SIBYLL, while the charmed hadron-proton cross sections are assumed to be equal to the Kp cross section. The typical energy range of interest is 10^{10} GeV-10^{12} GeV. The inelasticities are assumed to be energy-independent, with $\kappa_{hp} = 0.8$ for all hadron-proton interactions, including for

charmed hadrons.

The hadronic injection rates are also modified by the effective optical depth of the pp reaction, which is $f_{pp} \approx \kappa_{pp}\sigma_{pp}n_N r_{\rm ej} \simeq 5.7\times10^4\, M_{\rm ej,1}\beta_{\rm ej,-1}^{-2}t_4^{-2}$ for $\sigma_{pp}\sim 10^{-25}\,{\rm cm}^{-2}$ and $\kappa_{pp}\sim 0.5$ in the case of a magnetar driven supernova. The modification of the hadronic injection rate is thus

$$\frac{dN_h}{dE_h}(E_h) \longrightarrow f_{pp}\frac{dN_h}{dE_h}(E_h)\left[1-\exp\left(-\frac{t_{\rm cl}}{t^h_{\rm dec}}\right)\right]\ . \tag{5.11}$$

Cooling in the merger case is treated in a similar fashion. Secondary pion production from πp interactions are neglected, which can affect the spectra by a factor $\mathcal{O}(1)$ at earlier times [207].

5.3 Neutrino production

In Section 3.2 we presented formulas that accurately depict the neutrino spectra from ultrarelativistic pion and muon decays. When determining the neutrino spectrum from muon decays, Eq. (3.11) uses the muon polarization. Here we note that this polarization is determined at production, but the neutrino spectrum is determined when the muon decays, which happens after muon cooling.

To include cooling, we define the average polarization

$$\langle h_{\pi\to\mu}\rangle = \frac{\int_{\varepsilon_\mu}^{E_\mu/\lambda_\pi} dE_\pi \dfrac{h(E_\mu/E_\pi)}{E_\pi(1-\lambda_\pi)}\left.\dfrac{dN_\pi}{dE_\pi}\right|_{\rm prod}(E_\pi)}{\int_{E_\mu}^{E_\mu/\lambda_\pi} dE_\pi \dfrac{1}{E_\pi(1-\lambda_\pi)}\left.\dfrac{dN_\pi}{dE_\pi}\right|_{\rm prod}(E_\pi)}, \tag{5.12}$$

where $dN_\pi/dE_\pi\,|_{\rm prod}$ is the pion spectrum at production, ignoring cooling effects. The neutrino spectrum is thus given by the formula

$$\frac{dN_\nu}{dE_\nu} = \int_{E_\nu}^\infty dE_\mu \frac{dN_\mu}{dE_\mu}\left(1-\exp\Big(-\frac{t_{\rm cl}}{t^\mu_{\rm dec}}\Big)\right)\langle F_{\mu\to\nu}\rangle, \tag{5.13}$$

where dN_μ/dE_μ is found from Eq. (3.4), with the cooling factor for the pion included in dN/dE_π and the function $\langle F_{\mu\to\nu}\rangle$ is given by Eq. (3.11) with the substitution $h_{\pi\to\mu}\to\langle h_{\pi\to\mu}\rangle$. This is valid under the assumption that the muons are not depolarized.

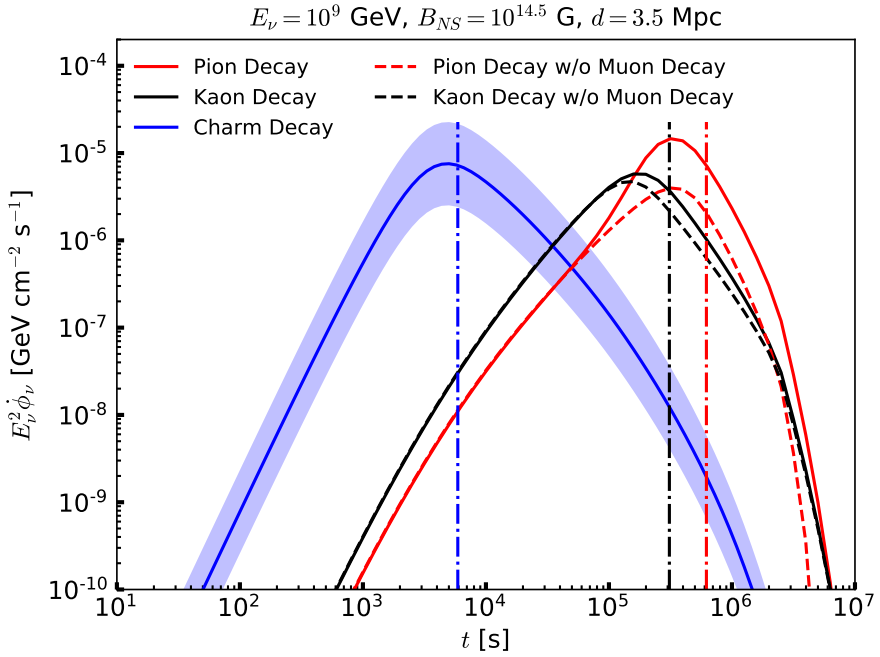

Figure 5.1. All-flavor neutrino light curve $E_\nu^2 \dot{\phi}_\nu$ at $E_\nu = 10^9$ GeV of a magnetar at a distance of 3.5 Mpc. The charm uncertainty factor of 1/3–3 around the central curve is given by the shaded blue region. For the case of neutrinos from pion (kaon) decay, we include an additional dashed red (black) curve to isolate the ν_μ component from π^+ (K^+) $\rightarrow \mu^+ \nu_\mu$ and charge conjugate, without taking into account the contributions from the muon decay. The dot-dashed vertical lines indicate the locations where decay time and cooling time are equal, based on our estimate given by Eq. (5.14). Here, the spin-down time is $t_{\rm sd} = 10^{3.5}$ s.

5.4 Magnetar-driven supernovae

Our first magnetar model assumes $M_{\rm ej} = 10\ M_\odot$, $\beta_{\rm ej} = 0.1$, $I = 10^{45}$ g cm^2, $B_{\rm NS} = 10^{14.5}$ G, $R_{\rm NS} = 10^6$ cm and $f_{\rm acc} = 0.1$. The initial angular frequency is $\Omega_i = 10^4$ s^{-1}, an optimistic value because its corresponding period $P_i = 0.6$ ms is close to the minimum period of a neutron star [18]. The associated spindown time is $t_{\rm sd} = 10^{3.5}$ s. For the purposes of observation estimates, we consider a nearby magnetar at a distance of $d = 3.5$ Mpc. We calculate the neutrino injection rate dN_ν/dE_ν and convert it to the observed single source flux $\dot{\phi}_\nu = (1/4\pi d^2) dN_\nu/dE_\nu$, where d is the source distance.

The neutrino optical depth can be estimated as $\tau_{\nu N} = n_N \sigma_{\nu p} r_{\rm ej} \simeq 3.1 \times 10^{-2} M_{\rm ej,1} \beta_{\rm ej,-1}^{-2} t_4^{-2}$, where we take $\sigma_{\nu p} \sim 10^{-32}$ cm^{-2}, which is the order of magnitude for the neutrino-nucleon charged current cross section in the 10^9 GeV - 10^{10} GeV range. We can thus neglect neutrino attenuation effects in our calculations, except for $t < 10^3$ s. Fortunately, for such early times, the flux does not significantly contribute to the fluence. For this work,

we consider the all-flavor neutrino flux, so neutrino oscillation effects are ignored. While we won't separate the fluxes from a single source by flavor, we will separate it into its source components from pion, kaon and charm, namely, $\dot{\phi}_{\nu,\pi}, \dot{\phi}_{\nu,K}$ and $\dot{\phi}_{\nu,c}$ respectively. Similar notations will be used when referring to the fluence and the diffuse neutrino flux.

We show the neutrino light curves from pions, kaons and charm at $E_\nu = 10^9$ GeV in Fig. 5.1. Here we observe the expected pattern of neutrinos from charm decay dominating first, followed by contributions of kaon and pion decay at later times. We also found that D^0 decays contribute the most to the charm component of the neutrino flux, due to its larger production cross section compared to other charmed hadrons.

We see that for $t < t_{\rm sd}$, all fluxes are suppressed. In this regime, where we can assume $L(t)$ and $E^M(t)$ are time independent, the time dependence is carried by the cooling factor. The large matter density leads to a short cooling time, and the cooling factor is well approximated by $t_{\rm cl}/t_{\rm dec} \propto t^3$, where the t^3 power law comes from the $n_N \propto t^{-3}$. The charm flux peaks slightly after $t_{\rm sd}$, when cooling time and decay time are equal, and will continuously decrease afterward, as a result of the luminosity decrease. The time dependence of the spectral function $F_{pp\to h}$ due to its dependence on E_p will also mildly contribute to the flux suppression (see Eq. 5.9).

In the case of the kaon and pion components of the neutrino flux, the impact of the luminosity decrease is not as significant as the exponential increase in the cooling factor, causing the t^3 behavior to shift to an approximate t^2 power law above $t_{\rm sd}$. We stress that this tail of the pion component of the light curve, and its t^2 dependence, can be significantly modified by secondary pion production and cause a flatter light curve. At $t \sim 3 \times 10^5$ s, pion and kaon cooling stops, and the flux suppression is caused by the luminosity decrease. At $t \sim 5 \times 10^6$ s there is a sharp cutoff that is caused by the corresponding cutoff in the pion/kaon flux due to $E_{\pi/K}/E_p$ approaching unity, as well as the decrease in the efficiency f_{pp}. A similar effect occurs for the charm component, but is not shown in the figure.

Above $t \sim 10^5$ s, we observe a small bump in the pion flux, which is caused by the muon decay component that is no longer suppressed by its corresponding muon cooling factor (see dashed red line in Fig. 5.1). This feature is less prominent with kaons; contributions from muon decays in this case are much smaller because they come from the high $y_K = E_\mu/E_K$ region, where the distribution function is much smaller.

In Fig. 5.1, for our parameter choices and $E_\nu = 10^9$ GeV, the pion, kaon and charm sources of the fluxes have approximately the same $E^2\dot{\phi}$ peak. This is not a general feature, as these peaks are related to the interplay between the spindown luminosity

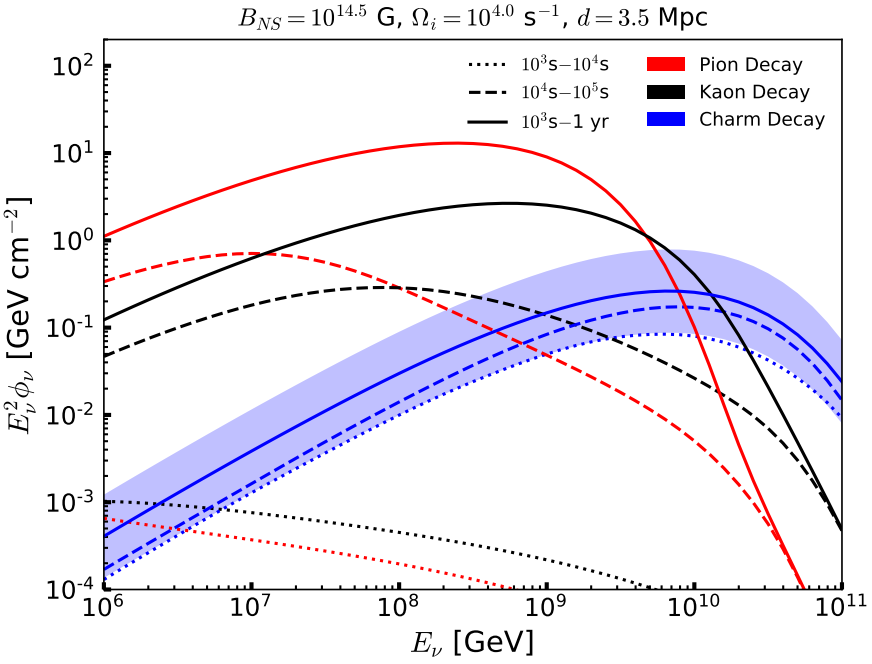

Figure 5.2. All-flavor fluence of high-energy neutrinos of a nearby magnetar at a distance of 3.5 Mpc, for different time intervals. A band in the charm spectrum in the time interval 10^3 s – 1 yr is shown, spanning a factor of $1/3 - 3$ times the central result.

and cooling factors for each particle. The spindown luminosity determines the injected proton flux, while the cooling factor is in general different between particles since they have different masses and decay rates.

The peak flux is approximately determined by the critical time, when $t_{\rm dec} = t_{\rm cl}$. Because of the different t dependence of the fluxes, at higher (lower) neutrino energies, the pion and kaon peak fluxes are lower (higher) than the charm peak flux.

However, we note that the relative positions of the peaks, for any neutrino energy, is the same, since it depends on the ratios of the hadron masses and their lifetimes, neglecting small difference in the energy dependence of the cross section, σ_{hp} for different hadron. The exception to this rule occurs when the neutrino energy is close to the proton energy.

The critical time, t_h^{cr}, which is the time at which the decay time, $\tau_h E_h / m_h c^2$, is equal to the cooling time, $t_{\rm cl} \approx (\kappa_{hp} \sigma_{hp} n_N c)^{-1}$, is given by

$$t_h^{\rm cr} \simeq 68 \text{ s} \left(\frac{E_h}{m_h c^2} \right)^{1/3} M_{\rm ej,1}^{1/3} \sigma_{hp,-25}^{1/3} \beta_{\rm ej,-1}^{-1} \tau_{h,-9}^{1/3}. \tag{5.14}$$

A slight deviation from this relationship is present in our simulations because of the

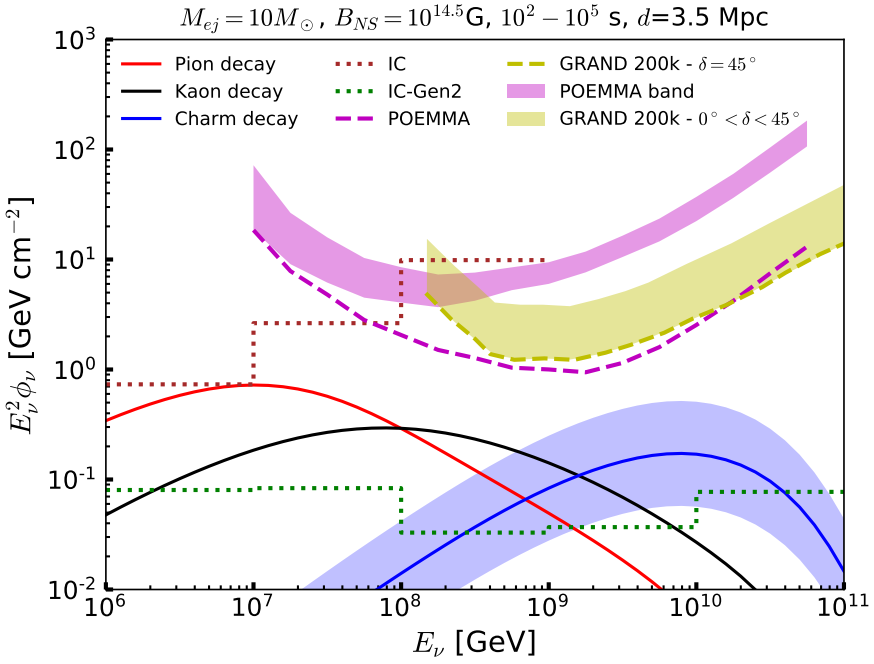

Figure 5.3. Neutrino fluence in the interval $10^2 - 10^5$ s compared to the long burst sensitivities of various experiments. A band in the charm spectrum is shown, spanning a factor of $1/3 - 3$ times the central result. The IceCube 90% CL upper limit on the spectral fluence from GW170817 on a 14-day window [15] (dotted brown line), while the IceCube-Gen2 curve is the 90% sensitivity for an event at a similar position in the sky [15] (dotted green line). The best 90% unified CL sensitivity per energy decade for long bursts for POEMMA is given by the dashed purple line, while its the purple band is the sensitivity range over most portions of the sky [16]. The 90% CL sensitivity for GRAND 200K in the optimistic case of a source at declination $\delta = 45°$ is shown by the dashed yellow line, and the yellow band is the declination-averaged sensitivity $0° < \delta < 45°$ [17].

inherent time dependence of the hadron-proton cross section σ_{hp}. We can estimate the critical energy E_h^{cr} at which cooling time is equal to decay time. We use Eq. (5.14), substituting $t_h^{\rm cr}$ with t and E_h with $E_h^{\rm cr}$ and solving for $E_h^{\rm cr}$. The estimated value of $E_h^{\rm cr}$ increases with time.

We applied these estimates to Fig. 5.1 and marked these critical times with dot-dashed lines. To convert the neutrino energy $E_\nu = 10^9$ GeV to a hadron energy, we estimate $E_h = 4E_\nu$ for $h = \pi, K$ and $E_h = 3E_\nu$ for D^0. Eq. (5.14) somewhat overestimates the time at which the peak flux occurs because of the simplified form of the equation, which does not include time dependence of the luminosity, for example.

The all-flavor fluence, ϕ_ν, scaled by neutrino energy squared for the model is shown in Fig. 5.2, for three time intervals. We observe that the pattern in Fig. 5.1 extends over a wide energy range: pion and kaon fluxes are suppressed below 10^4 s, when the neutrino

flux is predominantly from charm decay. The most energetic protons are accelerated at early times, where strong hadronic cooling of pions and kaons occurs. Consequently, the neutrino flux is dominated by charm decay at the highest energies, followed by kaon decay and finally pion decay, in order of their respective decay times. Unlike the neutrino light curves, the time dependent proton energy cutoff effects are not seen in Fig. 5.2 as they get smeared out by the time integration, with the exception of the absolute cutoff given by $E^M(t=0)$, which lies outside the chosen energy range.

For $t > 10^5$ s, the proton number density is very low and cooling effects become negligible. At late times, we see pion contributions dominating the neutrino fluence, with a maximum of $E^2\phi_\nu$ at 10^9 GeV for this model. We expect the maximum value of $E^2\phi_\nu$ from the pion contribution to be at a lower energy than that from charm because proton injection energy decreases with time.

We also varied the mass $M_{\rm ej}$ to $20M_\odot$ and $30M_\odot$ and compared the fluences with those of Fig. 5.2. In the time interval $10^3 - 10^4$ s, all fluxes are suppressed by approximately the same factor above 10^9 GeV, while charm is not very sensitive to $M_{\rm ej}$ below this energy. At larger times, fluence become less sensitive to mass. This insensitivity manifests itself at lower energies first, where decay time is shorter. The total fluence is very insensitive to mass, and the fluence does not vary more than a factor $\sim 2-3$ because late time emissions contribute the most to the total fluence, when the cooling time is very large.

A separate all-flavor fluence calculation was made with $B_{\rm NS} = 10^{15}$ G (other parameters remain the same). Our results for $t > t_{\rm sd}$ are in agreement with those of Ref. [207], which use the same parameter set.

In Fig. 5.3 we compare the neutrino fluence, in the interval 10^2 s - 10^5 s, with the sensitivities of various experiments to a long burst. We show the IceCube 90% CL upper limit on the spectral fluence from GW170817 in a 14 day window [15] to illustrate IceCube's current sensitivity. The projected 90% CL sensitivities for IceCube-Gen2 for a similar position in the sky (green dotted histogram) [15], for POEMMA's best case scenario (purple dashed curve) and sensitivity range over most portions of the sky (purple band) [16], and for GRAND 200K for the declination average over $0^\circ < \delta < 45^\circ$ (yellow band) and for $\delta = 45^\circ$ (dashed yellow curve) [17] are also shown.

We see in Fig. 5.3 that the pion component can be detected in IceCube in the 1 PeV - 10 PeV range, but the kaon component will be below the sensitivity curve for this model. IceCube Gen-2, however, would pick up all the components above 10^8 GeV. If we have a magnetar at a distance of 1 Mpc, POEMMA and GRAND 200K can detect the charm component, although such an event would be rare. In the case of a shorter burst of less

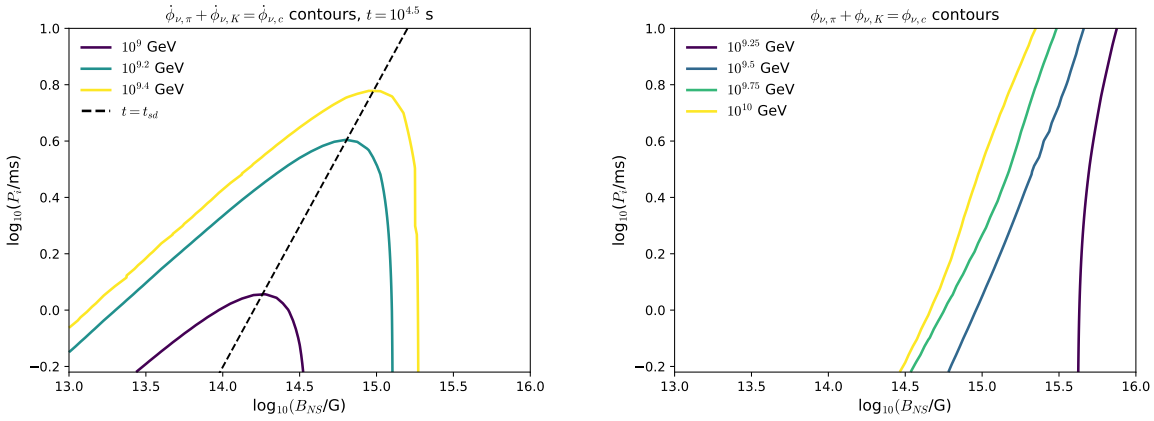

Figure 5.4. Left panel: Contour plots where $\dot{\phi}_{\nu,\pi} + \dot{\phi}_{\nu,K} = \dot{\phi}_{\nu,c}$ at the injection time $t = 10^{4.5}$ s. We have also marked the line where $t = t_{\rm sd}$. The lower limit in the period corresponds to the minimum spin period of a neutron star, $P_i \sim 0.6$ ms [18]. The parameter space below the solid curves have $\dot{\phi}_{\nu,c} > \dot{\phi}_{\nu,\pi} + \dot{\phi}_{\nu,K}$ for a given energy. Right panel: Same as left panel, but using the total fluence ϕ instead of the flux $\dot{\phi}$ at a fixed time. The parameter space to the right of the solid curves have $\phi_{\nu,c} > \phi_{\nu,\pi} + \phi_{\nu,K}$ for a given energy.

than 10^3 s, where the POEMMA and GRAND 200K sensitivities are better, we find that the fluence is not large enough to reach these sensitivities.

We also studied the parameter sets where we can get significant charm contributions. To do this, we look at the $B_{\rm NS} - P_i$ parameter space, keeping all other parameters listed at the beginning of the section fixed. For each $(B_{\rm NS}, P_i)$ pair, we look at the energy where $\phi_{\nu,\pi} + \phi_{\nu,K} = \phi_{\nu,c}$, that is, the energy where the neutrino flux from pions and kaons falls below the neutrinos from charm. We first look at these contours for $t = 10^{4.5}$ s, which are shown in the left panel of Fig. 5.4. With a fixed injection time, the cooling factors depend primarily on the Lorentz factor E_h/m_h because the hadron-proton inelastic cross section grows slowly with energy. Thus, the proton energy becomes the relevant variable when scanning the parameter space, as this determines the hadronic spectrum. The region of $B_{\rm NS} - P_i$ parameter space below the solid curves have $\dot{\phi}_{\nu,c} > \dot{\phi}_{\nu,\pi} + \dot{\phi}_{\nu,K}$ for a given energy. The diagonal black dashed line in the left panel of Fig. 5.4 shows $t = t_{\rm sd}$. To the left of the black dashed line, the luminosity $L(t)$ is constant and to the right, it is proportional to t^{-2} (see Eq. (5.1)). As mentioned above, for $t \gg t_{\rm sd}$ the proton energy $E^M(t)$ becomes independent of P_i, which is why we get the vertical lines on the contours.

In the right panel of Fig. 5.4, we make a similar study using the total fluence, where the region of $B_{\rm NS} - P_i$ parameter space to the right of the solid curves have $\Phi_{\nu,c} > \Phi_{\nu,\pi} + \Phi_{\nu,K}$ for a given energy. When comparing fluence, the value of the $t_{\rm sd}$ is important: strong magnetic fields and small values of P_i are preferred, as this increases

the proton energy and enhances the charm spectrum. Late time emission is dominated by pion and kaon contributions, when $t \gg t_{\rm sd}$. It follows that these fluences depend on $B_{\rm NS}$, but are independent of P_i (see Eq. (5.1) and Eq. (5.3)). On the other hand, charm contributions depend on both parameters, where smaller P_i increases the proton energy and the luminosity at early times, where charm production is relevant.

We emphasize that if the spindown time falls below 10^2 s, the neutrinos need to come from early decays, however, at early times, the proton density is high enough to cool even the charm hadrons. In addition, if the spindown time is small as a result of a large $B_{\rm NS}$, the luminosity will be much lower at later times because $L(t) \propto B_{\rm NS}^{-2} t^{-2}$ for $t \gg t_{\rm sd}$ (see Eq. (5.1)). We thus find that, while stronger $B_{\rm NS}$ is preferred to get a charm dominated flux at the highest energies, such a choice would hinder our ability to detect the neutrino flux.

5.5 Magnetar-driven merger novae

Another scenario of interest is neutrino production from merger ejecta. We use $I = 10^{45}$ g cm^2, $B_{\rm NS} = 10^{15}$ G, $R_{\rm NS} = 10^6$ cm, $f_{\rm acc} = 0.1$ and $\Omega_i = 10^4$ s^{-1}. For the ejecta mass, we use $M_{\rm ej} = 0.01\ M_\odot$ and initial speed $\beta_{\rm ej,0} = 0.1$. Changing the ejecta mass by a factor of 2 has negligible impact on the fluence.

The ejecta is less massive than the magnetar case and its speed increases with time, so cooling effects are weaker. This allows for enhanced neutrino production at earlier times, because charm hadrons will decay before cooling. We see in Fig. 5.5 that, for a nearby merger, next generation experiments could see the charm component, within a 1000 s time window, for sources optimally located for detection. The pion and kaon components, on the other hand, are suppressed below the sensitivity curve and would only be observable at later times.

5.6 Diffuse neutrino intensity

The sources discussed in Section III will also contribute to the diffuse neutrino flux. The corresponding all-flavor diffuse neutrino flux, Φ_ν is given by

$$\Phi_\nu = \frac{c f_s}{4\pi} \int_0^{z_{\rm max}} \mathcal{R}(z) \frac{dN}{dE'}[E(1+z)](1+z) \left|\frac{dt}{dz}\right| dz \tag{5.15}$$

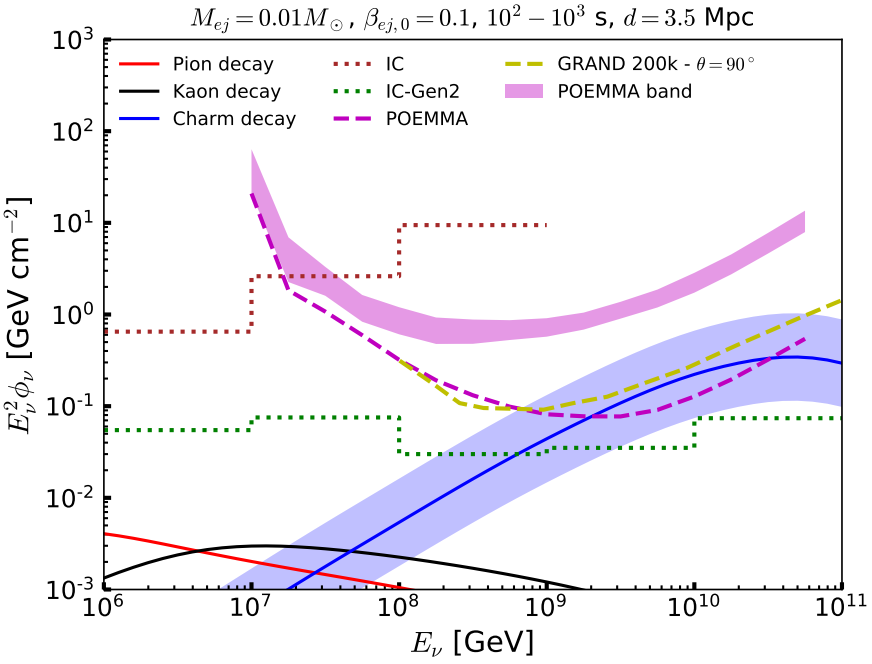

Figure 5.5. Neutrino fluence of a nearby neutron star merger at a distance of 3.5 Mpc, in the interval $10^2 - 10^3$ s, compared to the short burst sensitivities of various experiments. The IceCube 90% CL upper limit on the spectral fluence from GW170817 on a ± 500 s time window [15] is shown with a dotted brown line, while the IceCube-Gen2 curve is the 90% sensitivity for an event at a similar position in the sky [15] (dotted green line). The best 90% unified CL sensitivity per energy decade for short bursts for POEMMA is given by the dashed purple line, while its the purple band is the sensitivity range over most portions of the sky [16]. The 90% CL sensitivity for GRAND 200K in the optimistic case of a source at zenith angle $\theta = 90^\circ$ is shown by the dashed yellow line [17].

where $\mathcal{R}(z)$ is the local rate density of magnetar sources, $f_s \mathcal{R}(0)$, is a free parameter and its functional form can be parametrized as [232]

$$\mathcal{R}(z) = \mathcal{R}(0)(1+z)^{2.7} \frac{1 + [1/2.9]^{5.6}}{1 + [(1+z)/2.9]^{5.6}} \ . \tag{5.16}$$

We take $f_s \mathcal{R}(0) = 500$ yr^{-1} Gpc^{-3} in our evaluation below. This value is consistent with observations as long as not all of the supernova and merger events are bright. The prefactor f_s takes into account effects from pair loading, particle acceleration mechanisms and other phenomena that could affect flux normalization. The derivative $|dt/dz|$ is given by Eq. (2.34) with $\Omega_M = 0.3$, $\Omega_\Lambda = 0.7$ and $H_0 = 67$ km s^{-1} Mpc^{-1}.

Contributions to the diffuse flux are shown in Fig. 5.6. We include the results from the IceCube six-year HESE [19] and six-year shower [1] analyses. The diffuse flux sensitivities

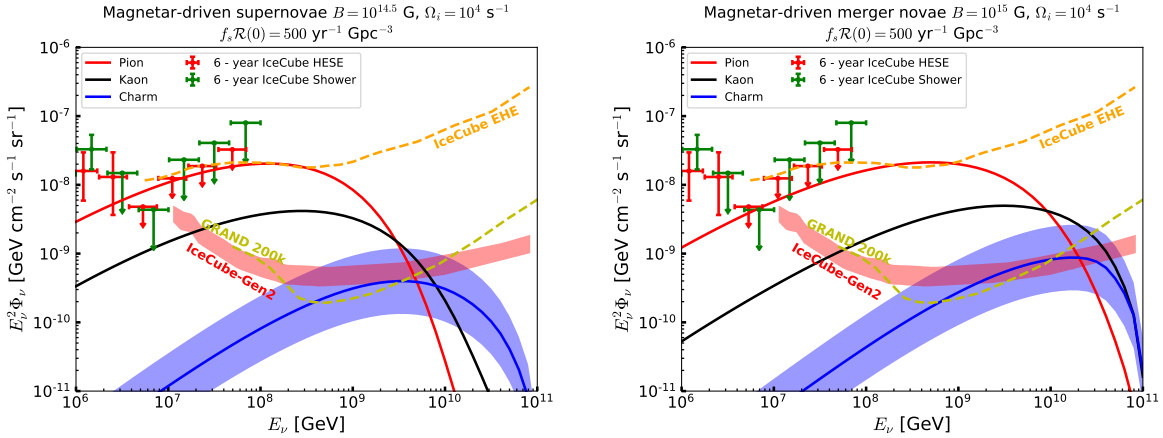

Figure 5.6. Left panel: Magnetar-driven supernovae contributions to the all-flavor diffuse neutrino flux. The red error bars show the results of the IceCube 6-year HESE analysis, obtained by multiplying the per-flavor neutrino flux in Ref. [19] by a factor of 3. The green error bars correspond to the IceCube 6-year shower analysis [1]. The 5-year IceCube-Gen2 sensitivity is shown by the red band [15], while the 10-year GRAND200k sensitivity is shown by the yellow curve and is scaled from the 3-year sensitivity [17]. The orange curve is the IceCube nine-year 90% CL EHE diffuse flux upper limit [20]. Right panel: Same as the left panel, showing instead magnetar-driven merger novae contributions to the diffuse neutrino flux.

for IceCube-Gen2 (5-year) [15] and GRAND 200K (10-year) [17] are shown by the red band and yellow curve, respectively, while the IceCube extremely-high-energy (EHE) diffuse flux upper limit (9-year) is shown by the orange curve. For both magnetar-driven supernovae and merger novae, we see that charm decay does not significantly contribute to the diffuse flux, because the flux is dominated by pion decay at late times. The fluxes for both types of supernovae and merger novae can remain below current IceCube limits if the rate is $f_s\mathcal{R}(0) = 500$ yr^{-1} Gpc^{-3}, and next-generation detectors can see the pion component up to $E_\nu \sim 10^{10}$ GeV. In the case of merger novae, cooling at early times is not as strong as the supernova case. At times $t > 10^4$ s, pions and kaons will decay before cooling, and will contribute significantly to the fluence, even at the highest energies. For magnetar-driven supernovae, the separation between charm and pion components is more pronounced, but the diffuse flux from charm hadron decay is not sufficiently high to be detected by IceCube-Gen2.

We point out that, for both scenarios, there is some tension between our models and the IceCube EHE limits, because the model dependent limits would be more stringent than the differential limit shown in Fig. 5.6 [20]. However, given model uncertainties such as the local rate density, one can evade these constraints.

5.7 Effects of the photomeson production

One of the possible caveats of this work is that we ignore the photomeson production. Details are model dependent and in principle depend on two kinds of radiation fields. One is radiation thermalized in the ejecta, while the other is thermal or nonthermal radiation from the wind bubble. If the radiation is thermal, the ejecta temperature is estimated to be $kT \approx 0.4$ keV $\mathcal{E}_{\rm rad,51}^{1/4}(\beta_{\rm ej}/0.1)^{-3/4}(t/1000\ {\rm s})^{-3/4}$, where $\mathcal{E}_{\rm rad}$ is the radiation energy. The threshold photomeson production is $E_p \sim 0.2\ {\rm GeV}^2/(3kT) \sim 0.2\times10^6$ GeV $\mathcal{E}_{\rm rad,51}^{-1/4}(\beta_{\rm ej}/0.1)^{3/4}(t/1000\ {\rm s})^{3/4}$, which is typically lower than the proton energy given by Eq. (5.3).

Above the threshold, the photomeson production optical depth is approximately given by Ref. [207]

$$\begin{aligned} f_{p\gamma} &\approx \kappa_{p\gamma}\sigma_{p\gamma}n_\gamma R_{\rm ej} \\ &\simeq 380\ (\mathcal{E}_{\rm rad}/10^{51}\ {\rm erg})^{3/4}(\beta_{\rm ej}/0.1)^{-5/4} \\ &\times\ (t/10^4\ {\rm s})^{-5/4}, \end{aligned} \tag{5.17}$$

where $\kappa_{p\gamma}\sim0.2$ is the inelasticity and $\sigma_{p\gamma}$ is the photomeson production cross section. Note that the multipion production is important in the case of the thermal radiation field. This can be compared to the effective pp optical depth, which is given by

$$\begin{aligned} f_{pp} &\approx \kappa_{pp}\sigma_{pp}n_{\rm ej}R_{\rm ej} \\ &\simeq 5.7\times10^4\ (M_{\rm ej}/10\ M_\odot)(\beta_{\rm ej}/0.1)^{-2} \\ &\times\ (t/10^4\ {\rm s})^{-2}, \end{aligned} \tag{5.18}$$

where $\kappa_{pp}\sim0.5$ is the inelasticity and σ_{pp} is the pp cross section. Thus, as long as energy injected by the central engine is thermalized, interactions with baryonic matter are more important at early times. The transition occurs at

$$t_{\rm tr} \sim 8\times10^6\ {\rm s}\ (M_{\rm ej}/10\ M_\odot)^{4/3}(\mathcal{E}_{\rm rad}/10^{51}\ {\rm erg})(\beta_{\rm ej}/0.1)^{-1}. \tag{5.19}$$

This implies that our results on the charm contribution are unlikely to be affected even if the thermal radiation field is included. This is because energy losses due to inelastic pp collisions are dominant in the early phase during which the charm contribution is dominant at the highest energies.

In addition, nonthermal particles may be generated at the termination shock inside the magnetar nebula (e.g., Refs. [233–235]). Analogous to the Crab pulsar wind nebula, a significant fraction of the Poynting energy could be dissipated. If this is the case, the thermalization in the nebula matters, which could happen if the nebular Thomson optical depth satisfies $\tau_T^{\rm nb} \gtrsim \beta_{\rm nb}^{-1}$, i.e., $t \gtrsim 2 \times 10^4$ s $M_{\rm nb,-7}^{1/2} \beta_{\rm nb,-1}^{-1/2}$, where $M_{\rm nb}$ is the nebular mass and $\beta_{\rm nb}$ is the nebular velocity. For example, in the merger case, this can happen if almost all the spindown energy is dissipated with the production of electron-positron pairs (see Ref. [211] for such a case). Then, the model would need to be adjusted to include contributions from $p\gamma$ interactions, where charmed hadrons are not produced. However, such a situation can be realized only if the nebula is compact, in which most of the thermalization occurs in the ejecta. Details depend on the magnetization and pair-loading of the wind that are uncertain. Also, if only a fraction of the spindown energy is dissipated in the nebula [236], our assumptions can be justified. Note that our setup for the calculations is similar to those in the previous works [209, 210]. See Fig. 1 of Refs. [207] for effects of the photomeson production (see also Ref. [211] for the merger case).

5.8 Conclusions

We presented a study of ultrahigh-energy neutrino production by newborn magnetars, accounting for pion, kaon and charmed hadron production from pp interactions in the supernova and merger ejecta. The charm component was obtained in the QCD calculation at NLO accuracy, together with an uncertainty band, a factor of $1/3 - 3$ around the NLO QCD flux that encloses the results obtained from k_T factorization approaches and the SIBYLL Monte Carlo simulations. The evolution of the proton injection spectrum and the ejecta expansion was included in the calculations, as well as the energy dependence of the various production cross sections. Using a benchmark parameter set, we found that for neutrino energies above 10^9 GeV, charm contributions are much higher than the pion and kaon contributions at early times because hadronic cooling suppresses the neutrino fluxes from these latter contributions. When $t > t_{\rm sd}$, the relative importance of kaon contributions increases as the ejecta's proton density decreases, followed by the pion contributions, in line with our expectations based on their lifetimes. The highest energies, above 10^{10} GeV, are dominated by charm contributions, essentially independent of pion/kaon contributions, and come from the most energetic protons which are injected at times $t < t_{\rm sd}$.

We found that for $B_{\rm NS} = 10^{14.5}$ G and $P_i = 2\pi \times 10^{-4}$ s, IceCube-Gen2 is projected to be sensitive to the charm component of the all-flavor neutrino fluence from a nearby magnetar at a distance ~ 3.5 Mpc, for locations such as that of GW17081. POEMMA and GRAND200k would be sensitive to such an event if it was located at a distance of ~ 1 Mpc. For the benchmark magnetar parameters, the accompanying pion and kaon contributions to the neutrino fluence at energies below 10^9 GeV could also be observed by IceCube (pion only) and IceCube Gen-2 (both).

We scanned the $P_i - B_{\rm NS}$ parameter space, to see at what energy the charm contributions to the neutrino flux overcome those of pions and kaons. Stronger magnetic fields and shorter periods are preferred, as this increases the proton energy at early times. However, these choices reduce the spindown time and cause cooling of charm hadrons, reducing their flux contributions below POEMMA and GRAND sensitivity curves.

In the case of a nearby neutron star merger, we found that neutrinos from charm hadron decay are likely to be observed by next generation detectors, within a time window of ~ 1000 s, without the accompanying lower energy neutrinos from pion and kaon decays. Both magnetar-driven supernovae and merger novae neutrino fluxes are consistent with IceCube's diffuse flux measurements.

Newborn magnetars have been expected to be the promising sources of gravitational waves, which is especially the case in the merger scenario (see Ref. [237] for a review). Even for the magnetar-driven supernova case, gravitational waves from a nearby event may be detected by current and future detectors if a magnetar is deformed and/or subject to instabilities [235]. Our model demonstrates that newborn magnetars are interesting targets for multimessenger searches with gravitational waves and ultrahigh-energy neutrinos, as well as electromagnectic waves.

Chapter 6
BSM Neutrino interaction models

In this dissertation we consider BSM neutrino interactions at the phenomenological level. Our models are not intended to be UV complete or to be used as a means of explaining phenomena such as neutrino masses. Astrophysical neutrinos are expected to collide with two potential targets in transit: the CνB and dark matter χ. Among the possible interactions between neutrinos and these targets, we focus on scalar mediators ϕ and vector mediators V^μ only, with interactions terms of the form $\bar{f}f'\phi$ and $\bar{f}\gamma^\mu f' V_\mu$, respectively, for bispinors f, f'. Among the possible combinations of f, f', we allow $\nu - \nu$ and $\chi - \chi$ couplings, but we do not consider $\nu - \chi$ direct couplings. We show the typical Feynman diagrams in Fig. 6.1.

Active neutrinos are left-handed in nature, so some of these interactions are forbidden, depending on whether the neutrino is Dirac or Majorana. Taking Dirac neutrinos as an example, $\bar{\nu}\nu\phi$ requires us to couple ν_L with ν_R, but ν_R does not exist without invoking BSM physics, such as sterile neutrinos or the seesaw mechanism. On the other hand, a vector mediator would use $\bar{\nu}\gamma^\mu\nu V_\mu$, which couples ν_L with ν_L, just like in the Standard Model. Majorana neutrinos have the interesting feature of allowing the existence of a

Figure 6.1. Left panel: Neutrino-neutrino interactions mediated by a scalar or vector mediator. Right panel: Same as right panel, but showing neutrino-dark matter interactions. In both cases, we account for the general situation where neutrinos of different flavors can couple to the mediator.

right handed neutrino, ν_L^C, which can be built from ν_L alone and does not require BSM.

To compute the cross sections, we begin with the kinematics. Our targets are taken at rest, so for an incident neutrino of energy ε_ν, its scattered energy ε'_ν is given by

$$\varepsilon'_\nu = \frac{\varepsilon_\nu}{1 + \dfrac{\varepsilon_\nu}{m_{\nu,\chi}}(1 - \cos\theta)}, \tag{6.1}$$

where θ is the scattering angle. This equation implies that the lower the scattered energy, the larger the scattering angle. With this, we have the differential cross section

$$\frac{d\sigma}{d\cos\theta} = \frac{\langle|\mathcal{M}|^2\rangle}{32\pi} \frac{1}{(m_{\nu,\chi} + \varepsilon_\nu(1 - \cos\theta))^2}, \tag{6.2}$$

where $\langle|\mathcal{M}|^2\rangle$ is the spin averaged squared amplitude of the interaction. The amplitude depends on the mediator type and the interaction channel. For the first examples, we assume a coupling g for all processes for simplicity, consider a single neutrino generation, and assume the incoming neutrino to be ultrarelativistic. The Mandelstam variables s, t and u are

$$s = 2m_\nu\varepsilon_\nu \qquad t = -2\varepsilon_\nu\varepsilon'_\nu(1 - \cos\theta) \qquad u = -s - t \tag{6.3}$$

for $\nu\nu$ scattering, assuming $m_\nu^2 \ll s, t, u$ and

$$s = m_\chi^2 + 2m_\chi\varepsilon_\nu \qquad t = -2\varepsilon_\nu\varepsilon'_\nu(1 - \cos\theta) \qquad u = 2m_\chi^2 - t - u \tag{6.4}$$

for $\nu\chi$ scattering.

6.1 $\nu - \bar{\nu}$ s-channel scattering with a scalar mediator

The standard cosmological model, ΛCDM, provides a reasonable explanation for the evolution of the Universe while remaining consistent with the cosmic microwave background, large-scale structure in galaxy distribution and the observed nuclei abundances. Through cosmic microwave bacgkround (CMB) observations, the Planck experiment measured a value of $H_0 = 67.4 \pm 0.5$ km s^{-1} Mpc^{-1} [126], which is in stark contrast to the value $H_0 = 73.04 \pm 1.04$ km s^{-1} Mpc^{-1} derived from Cepheid-SN data [238]. This discrepancy is known as the Hubble tension, which shows that the ΛCDM model is incomplete. Neutrino self-interactions provide a way to alleviate the tension, but not

fully solve it. While the ΛCDM has neutrinos decouple from other particles once the Hubble rate exceeds the weak interaction rate, neutrino secret interactions can delay this decoupling. This affects the CMB power spectrum by enhancing it at smaller scales and shifting its acoustic peaks [239].

Here, we will focus on s-channel scattering with a scalar mediator, which requires an MeV-scale mediator to ammeliorate the Hubble tension [22]. This interaction channel is of interest because of the simplicity in the angular distribution and its cross section formula, which allows for fast Monte Carlo simulations of neutrino propagation. We will also discuss the basics of this interaction channel, how the MeV-scale mediator is relevant for IceCube neutrinos.

6.1.1 One neutrino generation

The interaction Lagrangian for this process is of the form $\bar{\nu}\nu\phi$. Under the assumption of s-channel scattering, the differential cross section in the lab frame as a function of the scattering angle θ is

$$\frac{d\sigma}{d\cos\theta} = \frac{g^4}{32\pi m_\nu^2}\frac{s^2}{(s-m_\phi^2)^2+m_\phi^2\Gamma_\phi^2}\left(1+\frac{\varepsilon_\nu}{m_\nu}(1-\cos\theta)\right)^{-2}, \tag{6.5}$$

Alternatively, we can use the differential cross section $d\sigma/d\varepsilon'_\nu$ as a function of ε'

$$\frac{d\sigma}{d\varepsilon'_\nu}(\varepsilon_\nu \to \varepsilon'_\nu) = \frac{g^4}{32\pi}\frac{s^2}{(s-m_\phi^2)^2+m_\phi^2\Gamma_\phi^2}\frac{1}{m_\nu\varepsilon_\nu^2}, \tag{6.6}$$

where $\Gamma_\phi = g^2 m_\phi/16\pi$ is the resonance width. Since we are assuming s channel scattering and a scalar mediator, the neutrino angular distribution in the center of mass frame is isotropic, which is why the energy distribution in the lab frame is flat. The invariant cross section is

$$\sigma(\varepsilon_\nu) = \frac{g^4}{16\pi}\frac{s}{(s-m_\phi^2)^2+m_\phi^2\Gamma_\phi^2}, \tag{6.7}$$

which we use to compute the angular distribution

$$\frac{1}{\sigma}\frac{d\sigma}{d\cos\theta} = \frac{\varepsilon_\nu}{m_\nu}\left(1+\frac{\varepsilon_\nu}{m_\nu}(1-\cos\theta)\right)^{-2}. \tag{6.8}$$

When computing the time delays of scattered neutrinos with respect to unscattered ones, we need the average of θ^2

$$\langle\theta^2\rangle \sim 2\int_{-1}^{1}(1-\cos\theta)\frac{1}{\sigma}\frac{d\sigma}{d\cos\theta}d\cos\theta \approx \frac{2m_\nu}{\varepsilon_\nu}\left[\ln(2\varepsilon_\nu/m_\nu)-1\right]. \tag{6.9}$$

This average assumes that we are collecting all particles, i.e. with scattered energies in $[0,\varepsilon_\nu]$; if we impose an energy threshold in our study, the lower bound of the scattering angle has to be modified in accordance to Eq. (6.1). This cross section is maximal when ε_ν is equal to the resonance energy

$$\varepsilon_{\nu,\,\mathrm{res}} = \frac{m_\phi^2}{2m_\nu} = 1\mathrm{PeV}\left(\frac{m_\phi}{10\mathrm{MeV}}\right)^2\left(\frac{m_\nu}{0.05\mathrm{eV}}\right)^{-1}. \tag{6.10}$$

The resonance cross section $\sigma_{res} = 8\pi/m_\phi^2$ is independent of g. The coupling will, however, determine the resonance width and how sharply the cross section decreases as we move away from resonance.

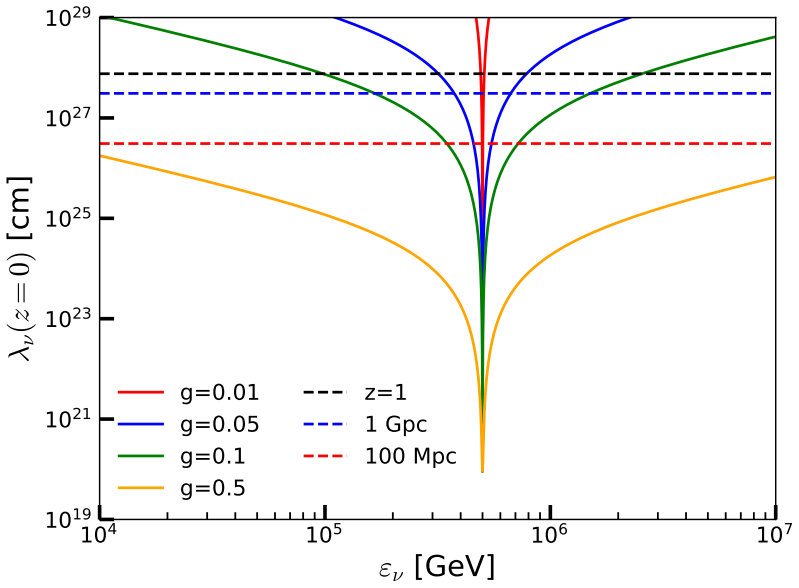

Figure 6.2. Neutrino mean free path λ_ν, at redshift $z = 0$, as a function of neutrino energy. We set the parameters $m_\nu = 0.1$ eV, $m_\phi = 10$ MeV, and choose a variety of coupling parameters g. As a reference, we use the light travel distances corresponding to 100 Mpc, 1 Gpc and $z = 1$.

Boson masses lying in the 1-10 MeV range would put the resonance energy in the 10 TeV - 1 PeV range, ideal for IceCube detection. While $\nu - \nu$ scattering in the t-channel is possible, the parameter space of interest causes t-channel contributions to be

subdominant [63, 64, 99].

Neutrino propagation depends on the mean free path length $\lambda_\nu = 1/n_\nu\sigma_\nu$, where $n_\nu = 56(1+z)^3\text{cm}^{-3}$ is the CνB target density at redshift z. In the case of a Majorana neutrino, the density is doubled. We show the interaction length at redshift $z = 0$ in Fig. 6.2. We chose the values of $m_\phi = 10$ MeV and $m_\nu = 0.1$ eV, which sets the neutrino resonance energy to $\varepsilon_{\text{res}} = 500$ TeV in the cosmic rest frame. The resonance length is $\lambda_{\text{res}} \sim 1.5 \times 10^{21}$ cm at ε_{res} =500 TeV and increases sharply off-resonance. The length is symmetric about ε_{res}, since $\sigma \propto s$ for $s \ll m_\phi^2$ and $\sigma \propto 1/s$ for $s \gg m_\phi^2$. As the value of g increases, the width of the resonance region increases, which allows for multiple scatterings. We included the light-travel distances corresponding to 100 resonance lengths, 1 Mpc and $z = 1$.

In general, the neutrino-neutrino cross section also has t-channel contributions and an additional u-channel term for Majorana neutrinos. However, our applications lie in the regime $g < 0.2$, where these terms are subdominant compared to the $s-$channel term [63].

6.1.2 Three neutrino generations

As mentioned before, in the case of multiple generations, instead of a single coupling we use a coupling matrix $g_{\alpha\beta}$, which reflects the general case where the interaction can change neutrino flavor. For example, the Lagrangian for $\nu\nu$ coupling with a scalar is $\mathcal{L}_{\text{int}} = -\sum_{\alpha,\beta} g_{\alpha\beta}\bar{\nu}_\alpha\nu_\beta\phi$. We switch to the mass basis because neutrino masses appear in the differential cross sections. Using Eq. (2.7), we have

$$\mathcal{L}_{\text{int}} = -\sum_{i,j=1}^{3}\left(\sum_{\alpha,\beta=e,\mu,\tau} U^*_{\alpha i} g_{\alpha\beta} U_{\beta j}\right)\bar{\nu}_i\nu_j\phi, \tag{6.11}$$

where the term in brackets becomes the coupling matrix in the mass basis

$$g_{ij} = \left(\sum_{\alpha,\beta=e,\mu,\tau} U^*_{\alpha i} g_{\alpha\beta} U_{\beta j}\right). \tag{6.12}$$

As an example, the differential cross section for the process $\nu_i\nu_j \to \nu_k\nu_l$ in $s-$channel scattering is

$$\frac{d\sigma_{ijkl}}{d\cos\theta} = \frac{|g_{ij}|^2|g_{kl}|^2}{32\pi m_\nu^2}\frac{s^2}{(s-m_\phi^2)^2 + m_\phi^2\Gamma^2}\left(1 + \frac{\varepsilon_\nu}{m_j}(1-\cos\theta)\right)^{-2}, \tag{6.13}$$

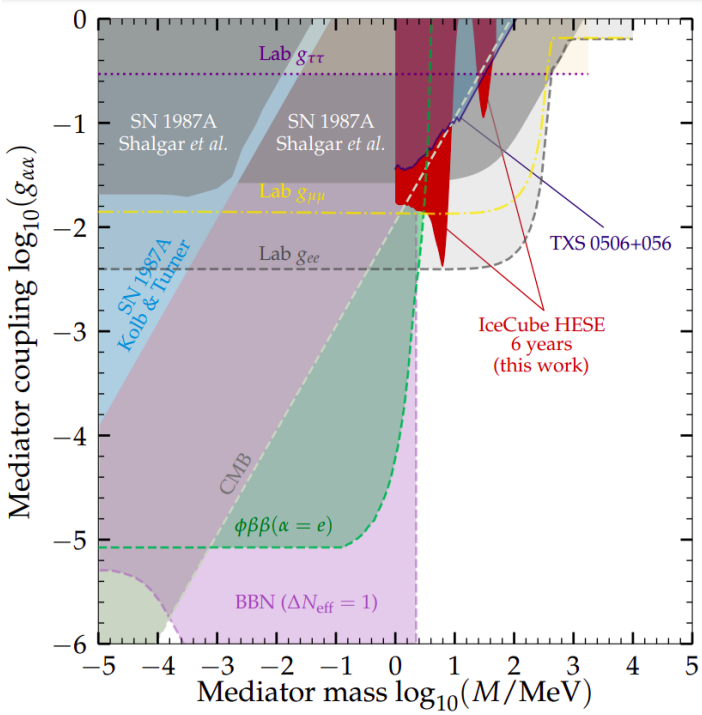

Figure 6.3. Constraints on coupling constant and mass of the scalar mediator of νSI. The red shaded region is disfavored by the IceCube six-year HESE sample [13]. Constraints which do not specify flavor assume $g_{ee} = g_{\mu\mu} = g_{\tau\tau}$. The constraints from CMB [21], BBN [22], lab measurements [23], SN1987A [24, 25] and the neutrino event coincident with the blazar TXS 0506+056 [26] are also included. Image from [27].

with $s = 2m_j\varepsilon_\nu$. This is the same formula for one neutrino generation, but instead of g we used $g_{ij}(g_{kl})$ for the $\nu_i\nu_j(\nu_k\nu_l)$ coupling in the Feynman diagram, and m_j as the target neutrino mass. The resonance width also needs to be adjusted to

$$\Gamma_\phi = \frac{m_\phi}{4\pi}\sum_{i,j} g_{ij}^2, \tag{6.14}$$

to account for the multiple decay nodes $\phi \to \nu_i\nu_j$.

In the three flavor case, it is also worthwhile to assess the current constraints of the model. We show in Fig. 6.3 the results of Ref. [27] based on IceCube data, assuming a diagonal coupling matrix. The CMB limits come from νSI effects on the CMB angular power spectrum [21], while the BBN constraints rely on the relationship between νSI and $N_{\rm eff}$ [22]. The lab constraints from Ref. [23] come from kaon decays $K \to e\nu\phi$ for g_{ee}, $K \to \mu\nu\phi$ for $g_{\mu\mu}$ and τ decay $\tau \to l\nu\nu\phi$ for $g_{\tau\tau}$. We see from these constraints that $g_{\tau\tau}$ is the least constrained out of the three. SN1987A constraints in Ref. [24] use the supernova as a neutrino source to constrain νSI interactions with the CνB, while those

in Ref. [25] also use the νSI's ability to halt the supernova explosion by preventing the shock revival. The neutrino event coincident with the blazar TXS 0506+056 also leads to constraints of the scalar mediator parameter space [26].

In the case of neutrino coupling to fermionic dark matter, the couplings are of the form $g_\alpha \bar{\nu}_\alpha \gamma^\mu \chi V_\mu + \text{h.c.}$. By switching to the mass basis, we see that to find the cross sections for $\nu_i \chi \to \nu_j \chi$, the change to the one-flavor formulas is $g^2 \to g_{ij}^2$ for the $\nu_i \nu_j$ coupling in the Feynman diagram.

6.2 ν-DM t-channel scattering

Besides neutrino-neutrino scattering with the CνB, neutrinos can also interact with a DM particle χ. In this case, we have no neutrino cascade but the scattering with χ will still lead to a time delay. Consider χ to be a Dirac fermion, with mass m_χ. Unless we are considering ultralight DM, we are dealing with $m_\nu \ll m_\chi$, so the scattering angles are expected to be significantly larger than in the case of neutrino-neutrino scattering. The typical propagation distances that we will be using are shorter than 1 Mpc. For this reason, we will assume $\varepsilon = E$ (i.e. no redshift energy loss).

Using the right panel of Fig. 6.1 as a guide, we consider three particle physics models for neutrino-DM interactions. First, we consider fermionic DM that interacts via a vector mediator V_μ, and the interaction Lagrangian of the form

$$\mathcal{L}_{\text{int}} \supset g_\nu \bar{\nu} \gamma^\mu \nu V_\mu + g_\chi \bar{\chi} \gamma^\mu \chi V_\mu, \tag{6.15}$$

where g_ν and g_χ are dimensionless coupling constants of the vector mediator to neutrinos and DM, respectively. We will also consider fermionic DM with a scalar mediator

$$\mathcal{L}_{\text{int}} \supset g_\nu \bar{\nu} \nu \phi + g_\chi \bar{\chi} \chi \phi, \tag{6.16}$$

and scalar DM with a scalar mediator

$$\mathcal{L}_{\text{int}} \supset g_\nu \bar{\nu} \nu \phi + g_\chi \Lambda \chi^* \chi \phi \tag{6.17}$$

For the scalar DM and scalar mediator case, we included an energy scale Λ (with dimensions of energy) for the Lagrangian density to have the correct dimensions.

For a neutrino-DM scattering with fermionic DM and a vector mediator, the differential cross section for the interaction takes the form

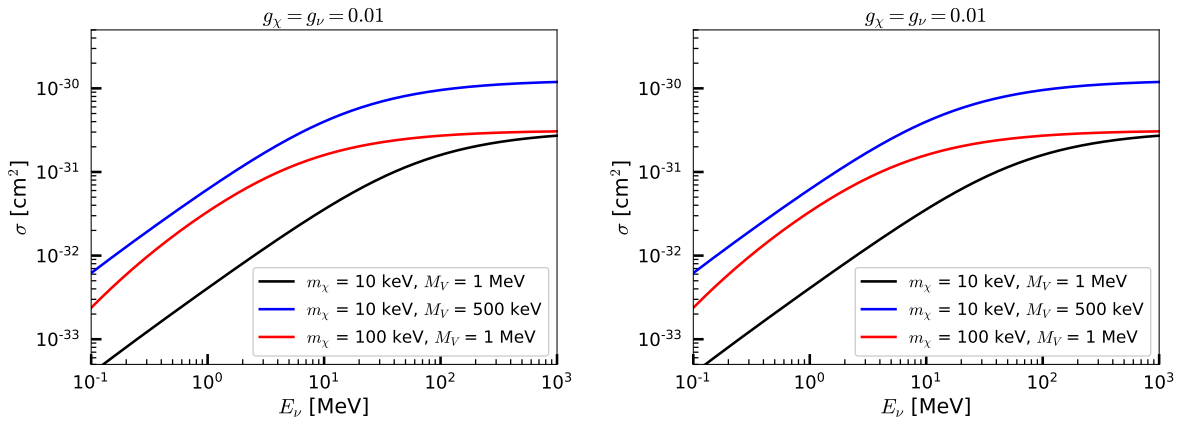

Figure 6.4. Left panel: Neutrino-DM differential cross section as given by Eq. (6.18), scaled by $\sin\theta$. We fixed m_χ= 1 keV, $m_V = 1$ MeV and $g_\nu = g_\chi = 0.01$. Cross sections are shown for energies $E_\nu = 5$ MeV, 10 MeV and 20 MeV. Right panel: Total cross section for $\nu\chi$ interactions via $t-$channel scattering, with $g_\nu = g_\chi = 0.01$ and a vector mediator of mass M_V.

$$\frac{d\sigma}{d\cos\theta} = \frac{g_\nu^2 g_\chi^2}{4\pi} \frac{E_\nu^2 + E_\nu'^2 - E_\nu E_\nu'(1-\cos\theta)}{(E_\nu E_\nu'(1-\cos\theta) + m_V^2)^2} \left(\frac{E_\nu'}{E_\nu}\right)^2, \tag{6.18}$$

where E_ν' is given by Eq. (6.1). For the application of the time delay approach of supernova neutrinos ($\mathcal{O}(10)$ MeV neutrinos), the parameter range of interest will be $m_\chi \in [1\text{ keV}, 100\text{ keV}]$ and $m_V \in [10\text{ keV}, 10\text{ MeV}]$.

The differential cross sections for this interaction process are shown in the left panel of Fig. 6.4 to provide insight into its angular distribution. The most notable difference is that the location of the peak of the distribution decreases with E_ν, which is to be expected in light of the $E_\nu(1-\cos\theta)/m_\chi$ term in E_ν'. From these distributions, we also find that the typical scattering angle is below 0.1. As for the total cross section, we see that for low neutrino energies the cross section has a power law scaling and for high energies the cross section flattens out. The effect of m_V at the highest energies is to scale the value of the cross section, scaling as m_V^{-2}. At low energies, the behavior depends on the combination of m_χ and m_V in a non-trivial way, as given by the analytic expression [104]

$$\begin{aligned}\sigma \;=\; & \frac{g_\nu^2 g_\chi^2}{16\pi E_\nu^2 m_\chi^2}\left[(m_V^2 + m_\chi^2 + 2E_\nu m_\chi)\log\left(\frac{m_V^2(2E_\nu + m_\chi)}{m_\chi(4E_\nu^2 + m_V^2) + 2E_\nu m_V^2}\right)\right. \\ & \left. + 4E_\nu^2\left(1 + \frac{m_\chi^2}{m_V^2} - \frac{2E_\nu(4E_\nu^2 m_\chi + E_\nu(m_\chi^2 + 2m_V^2) + m_\chi m_V^2)}{(2E_\nu + m_\chi)(m_\chi(4E_\nu^2 + m_V^2) + 2E_\nu m_V^2)}\right)\right].\end{aligned} \tag{6.19}$$

For scalar DM and scalar mediators, the differential cross section is [104]

$$\frac{d\sigma}{d\cos\theta} = \frac{g_\nu^2 g_\chi^2 \Lambda^2 (1-\cos\theta) E_\nu^2 m_\chi}{16\pi \left((1-x)E_\nu + m_\chi\right)\left((1-x)E_\nu m_\phi^2 + m_\chi\left(m_\phi^2 - 2(\cos\theta - 1)E_\nu^2\right)\right)^2}, \quad (6.20)$$

and the total cross section is

$$\sigma = -g_\nu^2 g_\chi^2 \Lambda^2 \frac{4E_\nu^2 m_\chi + (2E_\nu m_\phi^2 + 4E_\nu^2 m_\chi + m_\phi^2 m_\chi)\ln\left(\frac{m_\phi^2(2E_\nu + m_\chi)}{2E_\nu m_\phi^2 + 4E_\nu^2 m_\chi + m_\phi^2 m_\chi}\right)}{64\pi E_\nu^2 m_\chi^2 (2E_\nu m_\phi^2 + 4E_\nu^2 m_\chi + m_\phi^2 m_\chi)}. \quad (6.21)$$

In the case of fermionic DM and a scalar mediator, we have

$$\frac{d\sigma}{d\cos\theta} = \frac{g_\nu^2 g_\chi^2 (\cos\theta - 1) E_\nu^2 m_\chi^2 \left(2(\cos\theta - 1)E_\nu m_\chi + (\cos\theta - 1)E_\nu^2 - 2m_\chi^2\right)}{8\pi \left(m_\chi - (\cos\theta - 1)E_\nu\right)^2 \left((\cos\theta - 1)E_\nu m_\phi^2 - m_\chi\left(m_\phi^2 - 2(\cos\theta - 1)E_\nu^2\right)\right)^2}, \quad (6.22)$$

and

$$\begin{aligned}\sigma \;=\; & \frac{g_\nu^2 g_\chi^2}{32\pi E_\nu^2 m_\chi^2}\left[E_\nu m_\chi - \frac{E_\nu m_\chi^2}{2E_\nu + m_\chi} - \frac{E_\nu m_\chi^2 m_\phi^2\left(m_\phi^2 - 4m_\chi^2\right)}{\left(2E_\nu m_\chi + m_\phi^2\right)\left(4E_\nu^2 m_\chi + 2E_\nu m_\phi^2 + m_\chi m_\phi^2\right)}\right. \\ & \left. + \frac{E_\nu m_\chi\left(m_\phi^2 - 4m_\chi^2\right)}{2E_\nu m_\chi + m_\phi^2} + \left(m_\phi^2 - 2m_\chi^2\right)\log\left(\frac{m_\phi^2(2E_\nu + m_\chi)}{4E_\nu^2 m_\chi + 2E_\nu m_\phi^2 + m_\chi m_\phi^2}\right)\right]. \quad (6.23)\end{aligned}$$

The models introduced in this chapter will be used in the context of CνB or DM-induced scattering of astrophysical neutrinos as they travel from the source to the observer. In chapters 7 and 8 we will show how to simulate neutrino propagation and how to incorporate these BSM models. We will be using the total cross sections to determine the neutrino optical depth and the locations along the trajectory where neutrinos get scattered. Likewise, the differential cross sections will determine the angular distribution of neutrinos. The angular distributions in particular will be crucial to determine the elongated trajectory length of scattered neutrinos, and are going to be used extensively in Chapters 7 and 8.

Chapter 7
Simulating neutrino echoes induced by secret neutrino interactions

In this chapter, we will consider the case of neutrino echoes caused by νSI for 10 TeV neutrinos and above. We also outline the numerical techniques used to implement neutrino time delay for this model. The text in this chapter is based on my work in Ref. [116].

We assume that the $\nu - \nu$ scattering is mediated by a scalar boson ϕ, of mass m_ϕ. High-energy neutrinos will scatter off the CνB via $\nu\nu \to \nu\nu$ [63–65]. Assuming that neutrinos are Majorana fermions, we consider the effective Lagrangian for one neutrino generation, $\mathcal{L} \supset -\frac{1}{2} g \overline{\nu_L^c} \nu_L \phi + \text{c.c.}$, where g is the coupling constant. This model is used for its simplicity, as there is only one neutrino mass and allows us to separate neutrino mixing effects from intrinsic features of the BSM scattering. The three-generation case is discussed later. While the high energy neutrinos are ultrarelativistic and left-handed, the CνB kinetic energy is assumed to be lower than the neutrino mass, so these neutrinos are taken as unpolarized and at rest [240].

Given the angular distribution and our interest in neutrinos above 10 TeV, we expect the scattering angles to be of order $\mathcal{O}(10^{-7})$ and below, as is seen from equation (6.8) and $(1 - \cos\theta)\varepsilon_\nu / m_\nu \sim 1$. If neutrinos interact via a vector mediator, the total cross section would only increase by a constant factor. On the other hand, the angular distribution in the center-of-momentum frame is no longer isotropic: the left-handed neutrino is more likely to scatter in the forward direction. For the same g and source distance D, more (less) scatterings would take place in the vector (scalar) mediator case, resulting in typically longer (shorter) delays.

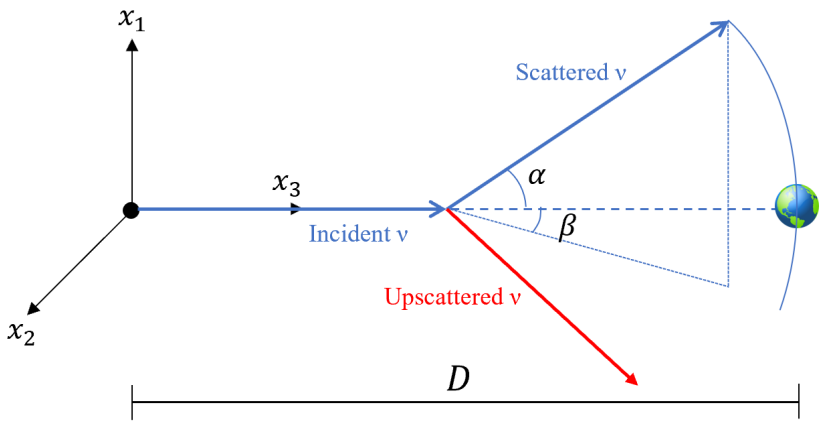

Figure 7.1. Geometrical setup for our MC simulations. The source is located at the origin, while the observer is at $(0, 0, D)$. An outgoing neutrino in the $+x_3$ direction is emitted. Upon scattering, the neutrino is deflected and an additional neutrino is upscattered. Neutrinos stop propagating when they reach the sphere of radius D. The angles α and β used to compute the time delay are also marked. For illustrative purposes, in this Fig.the initial neutrino scatters only once.

7.1 Method

In the astrophysical context, time delay due to small-angle scattering was studied e.g., for X-ray scattering [241, 242], and some techniques are applicable to the current problem of neutrino scattering by using the appropriate differential cross section.

We create a Monte-Carlo code to scatter the neutrinos from a given source and obtain the time delay distributions caused by BSM neutrino interactions. We adopt the geometrical setup of Ref. [241]. In Cartesian coordinates, the source is located at the origin, while the observer is at $(0, 0, D)$, as shown in Fig. 7.1. Neutrinos are emitted individually from the source and are tracked until they reach the observer. For a given neutrino path between source and observer, we can make appropriate rotations so that the initial neutrino is always emitted in the $+x_3$ direction, while the final location is some point on the surface of a sphere of radius D with the source as its center.

Let $\hat{\mathbf{p}}$ be the three-dimensional momentum unit vector of the neutrino and α be the angle that its projection on the x_1x_3 plane makes with the x_3-axis. Likewise, we define β as the angle between the x_3-axis and the projection of $\hat{\mathbf{p}}$ on the x_2x_3 plane. Under the assumption of small-angle scattering, $\alpha, \beta \ll 1$, which applies to our case, we neglect terms of third order and higher in α and β, such that the time delay t of a scattered

neutrino compared to an unscattered one is [241]

$$t = \frac{1}{2}\int_0^D (\alpha^2(x_3) + \beta^2(x_3))dx_3 - \frac{1}{2D}\left[\left(\int_0^D \alpha(x_3)dx_3\right)^2 + \left(\int_0^D \beta(x_3)dx_3\right)^2\right]. \quad (7.1)$$

The x_3 dependence in α and β represents the changes in these angles whenever a scattering takes place, thus being applicable for an arbitrary number of scatterings. Equation (7.1) is evaluated in the MC simulation by splitting into a discrete sum, where the steps dx_3 correspond to the distance traveled between scatterings. When a scattering takes place, a scattering angle θ is chosen based on equation (6.8), which changes the neutrino's momentum $\hat{\mathbf{p}}$ and hence the values α and β. Neutrino propagation stops upon reaching the sphere of radius D.

To determine distances, we choose the cosmological density parameter $\Omega_\Lambda = 0.7$, the matter density parameter $\Omega_M = 0.3$ and the Hubble constant $H_0 = 67$ km s^{-1} Mpc^{-1}. With these values, a source at redshift z corresponds to a particle-travel distance defined by Eq. (2.35). We also use this integral to establish a one-to-one correspondence between redshift and neutrino location.

Let ε_ν be the neutrino energy at some redshift. A neutrino initially at position $\mathbf{r}$ may experience a scattering at $\mathbf{r}' = \mathbf{r} + \hat{\mathbf{p}}dD$ for some traveled distance dD and $\mathbf{r} = (x_1, x_2, x_3)$. To identify dD, we also define the optical depth

$$\tau_\nu = \int_{x_3 - dD}^{x_3} n_\nu(x_3'')\sigma_\nu(\varepsilon_\nu(x_3''))dx_3'', \quad (7.2)$$

where $n_\nu(x_3) = 112$ cm^{-3} $(1 + z(x_3))^3$ is the $\nu + \bar{\nu}$ number density of the CνB and ε_ν becomes position dependent as a result of expansion losses. Notice that equation (7.2) is a line-of-sight integral and can be used instead of a three-dimensional approach because motion in the other axes is negligible in the small scattering approximation and has little effect in redshift losses.

The probability of an interaction occurring after propagating a distance corresponding to an optical depth τ_ν is $1 - \exp(-\tau_\nu)$. We can thus calculate dD in the MC simulation by drawing τ_ν from an exponential distribution and solving equation (7.2) for dD.

The main issue when solving for dD is that the cross section can increase by several orders of magnitude as the neutrino energy approaches $\varepsilon_{\rm res}$. The optical depth of a neutrino with energy $\varepsilon_\nu > \varepsilon_{\rm res}$ will then spike as expansion losses cause the neutrino to reach resonance energy. For small g, the resonance region is so narrow that a poor choice in dx_3'' when carrying out the numerical integration of equation (7.2) will cause us to

miss the resonance entirely.

To tackle this problem, we tabulate the cross section over as a function of the node energy in the range $[\epsilon_0, \epsilon_N]$, for some number of bins N, which contains $\varepsilon_{\rm res}$ and choose a node k such that $\epsilon_k = \varepsilon_{\rm res}$. We consider $k = N/2$ or the integer closest to $N/2$. We find the nearest resonance at ϵ_k, and the cross section decreases as we move away from ϵ_k. With ϵ_0 and ϵ_N fixed, given that ϵ_k is determined, we then find the value of ϵ_i that satisfies

$$\sigma_\nu(\epsilon_i) = \left(\frac{\sigma_\nu(\epsilon_0)}{\sigma_\nu(\epsilon_k)}\right)^{i/k} \sigma_\nu(\epsilon_0), \quad i \leq k, \tag{7.3}$$

and

$$\sigma_\nu(\epsilon_i) = \left(\frac{\sigma_\nu(\epsilon_k)}{\sigma_\nu(\epsilon_i)}\right)^{(N-i)/(N-k)} \sigma_\nu(\epsilon_N), \quad k < i \leq N. \tag{7.4}$$

With this method, we get a larger bin density near resonance as we increase N. In this work, we choose $\epsilon_0 = 1$ GeV and $\epsilon_N = 10^9$ GeV

We now proceed to outline the method to determine dD. We draw a random number by setting $\tau_\nu = -\ln u$ for a random number u uniformly distributed in (0,1]. Let $\mathbf{r}$ be the position of our neutrino with energy ε_ν. As the particle propagates in steps dx_3'', it accumulates contributions to the optical depth integral $\overline{\tau}_\nu$, following equation (7.2) and computed via the trapezium rule. Thus, dD becomes the sum of steps dx_3'' required to make $\overline{\tau}_\nu = \tau_\nu$. As for the choice of the spacing dx_3'' used for each contribution to $\overline{\tau}_\nu$, we use the energy nodes ϵ_i to account for redshift energy losses. For the first dx_3'' we first identify the node ϵ_i closest to ε_ν with $\varepsilon_\nu \geq \epsilon_i$. dx_3'' is the distance required so that ε_ν decreases to ϵ_i as a result of redshift energy losses alone. The next step dx_3'' is then chosen so that redshift reduces neutrino energy from ϵ_i to ϵ_{i-1}. Each step calculated via this method keeps increasing the value of $\overline{\tau}_\nu$ and this process is repeated until either reach the sampled τ_ν or exceed it. If $\overline{\tau}_\nu \geq \tau_\nu$, we interpolate to τ_ν and find its associated step dx_3''. It is possible that $\overline{\tau}_\nu \leq \tau_\nu$ throughout the remaining propagation length, in which case the particle is tracked up to the sphere of radius D without further scatterings.

With dD determined, the particle is moved from $\mathbf{r}$ to $\mathbf{r}'$, the contributions of α and β to the integrals $\int \alpha^2 dx_3$, $\int \beta^2 dx_3$, $\int \alpha dx_3$ and $\int \beta dx_3$ in equation (7.1) are computed, and the neutrino energy is redshifted to ε_ν' to account for the new position. To perform a scattering, we pick the scattered neutrino energy from a uniform distribution in the interval $[0,\varepsilon_\nu']$, since the scattered energy distribution is flat in the cosmic rest frame. From the scattered energy, we can determine the momentum four-vector for both the scattered and upscattered neutrinos, and the upscattered neutrino is injected at $\mathbf{r}'$.

To find time delay distributions in our examples, we inject neutrinos until the observer collects 10^7 neutrinos. The energy threshold, below which we do not collect particles, is specified in each example as $E_{\rm th}$.

Henceforth, we choose the values of $m_\phi = 10$ MeV and $m_\nu = 0.1$ eV, which sets the neutrino resonance energy to $\varepsilon_{\rm res} = 500$ TeV in the cosmic rest frame. In Fig. 6.2, we show the neutrino mean free path, $\lambda_\nu = 1/n_\nu \sigma_\nu(\varepsilon_\nu)$, using the C$\nu$B density at $z = 0$, as a function of the neutrino energy ε_ν. We include the particle-travel distances corresponding to 100 Mpc, 1 Gpc and $z = 1$, which will be used in our examples. To describe the regimes of interest, we also introduce the inelasticity parameter y, where $y = 0$ means that the incident neutrino loses no energy after the scattering. We will also make a distinction between the energy ε_ν at redshift z, which changes due to cosmological redshift, and the observed neutrino energy $E_\nu = \varepsilon_\nu(z = 0)$ at $z = 0$. In the first cases, where propagation distances are less than 1 Gpc, adiabatic energy losses do not play a significant role and we have $\varepsilon_\nu \approx E_\nu$. The distinction will be necessary in our examples with sources at $z = 1$.

7.2 Results

7.2.1 Scattering in the optically thin limit

As the first example, we consider the propagation of neutrinos with an optical depth of $\tau_\nu \ll 1$, corresponding to the optically thin limit. In this regime, neutrinos are unlikely to scatter more than once and only a fraction τ_ν of all neutrino events will experience a scattering.

Analytically, the time delay t follows, to a good approximation, the distribution,

$$P(t, \varphi; D) = \frac{1}{2t/D + \varphi^2} \frac{1}{\sigma_\nu} \left. \frac{d\sigma_\nu}{d\theta} \right|_{\theta = \varphi + 2t/(D\varphi)} \tag{7.5}$$

where φ is the arrival angle on Earth, with respect to the direction of the source. See Ref. [243] for the derivation. Integrating over φ will yield the delay distribution $P(t)$. The characteristic time delay in the optically thin regime is [106]

$$\Delta t \approx \frac{1}{2} \frac{\langle \theta^2 \rangle}{4} D \simeq 77 \text{ s } C^2 \left(\frac{D}{3 \text{ Gpc}} \right) \left(\frac{m_\nu}{0.1 \text{ eV}} \right) \left(\frac{100 \text{ TeV}}{E_\nu} \right), \tag{7.6}$$

where $\langle \theta^2 \rangle$ is the mean squared angular deflection from a single scattering. The constant

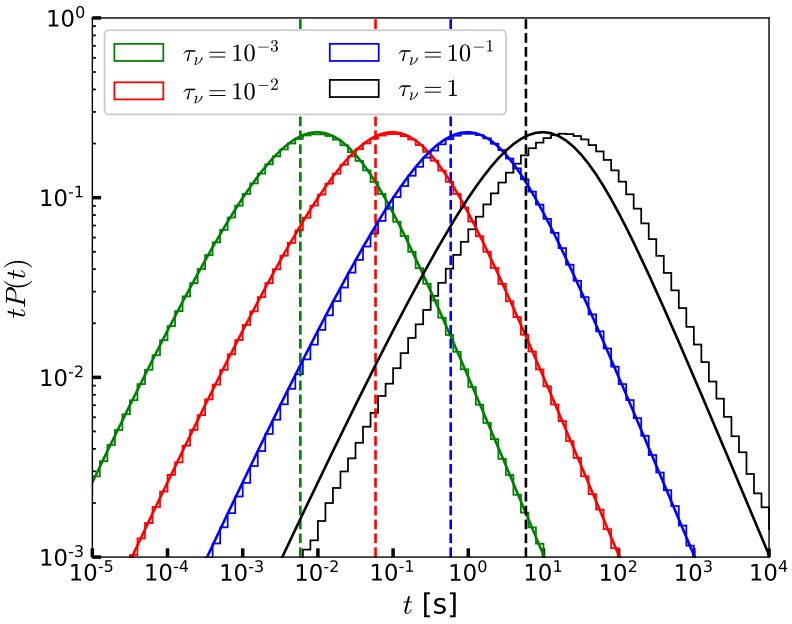

Figure 7.2. Time delay probability distribution, for different optical depths with $D = \tau_\nu$ Gpc. The histograms are the results from the MC simulations. The solid curves are obtained by integrating equation (7.5) over φ, while the dashed lines are the characteristic time delays given by equation (7.6).

$C \sim 1$ comes from the angular distribution of the interaction and thus depends on the mediator used. In the case of $s-$channel scattering, we have $\langle\theta^2\rangle = 2C^2 m_\nu/E_\nu$, with $C = 0.62$ for leading scattered neutrinos [106, 243].

To demonstrate our simulation results, we inject neutrinos with $\varepsilon_\nu = 170$ TeV and assume $g = 0.1$, which leads to $\lambda_\nu = 1$ Gpc. We choose $E_{\rm th} = 0$ and construct the time delay distribution $P(t)$, which are shown in Fig. 7.2 as histograms for different source distances $D = \tau_\nu\lambda_\nu = \tau_\nu$ Gpc. As expected, as D increases, the probability density decreases for shorter t. Second, for long time delays we get $P(t) \propto t^{-2}$. This is also verified by integrating equation 7.5 over φ, which is shown as solid curves, and we see the excellent agreement between analytical and numerical results in this optically thin limit. The characteristic time delays in equation (7.6) are also presented as dashed lines. With this example, we also see that our simulation results are consistent with the analytical estimate with leading particles.

We note that for $\tau_\nu \gtrsim 0.1$ one can see a visible difference between the numerical and analytical results. At this point, the Poisson probability of two scatterings taking place is $\tau_\nu^2 e^{-\tau_\nu}/2$, such that roughly 5% of the scattered events will scatter twice, causing them to

experience longer delays. At $\tau_\nu = 1$, the effect of multiple scatterings becomes apparent as we leave the optically thin regime. We note that $\tau_\nu = 1$ corresponds to 1 Gpc, where the redshift effect may take place. In this example we ignore redshift energy losses, which will be addressed later.

7.2.2 Scattering in the optically thick limit with zero inelasticity

Let us consider the case where neutrinos do not lose energy, in such a way that the angular distribution in equation (6.8) holds but there are no upscattered neutrinos. Assuming that multiple scatterings take place, the characteristic neutrino time delay in the large τ_ν limit can be estimated as [106]

$$\Delta t \simeq 500 \text{ s } C^2 \left(\frac{\tau_\nu}{10}\right)\left(\frac{D}{3 \text{ Gpc}}\right)\left(\frac{m_\nu}{0.1 \text{ eV}}\right)\left(\frac{0.1 \text{ PeV}}{E_\nu}\right), \tag{7.7}$$

implying $\Delta t \propto \tau_\nu^2$ for a given λ_ν.

The time delay distribution can be expressed as [241, 242]

$$P(t; D) = \frac{4\pi^2}{3\langle\varphi^2\rangle D}\sum_{n=1}^{\infty}(-1)^{n+1}n^2 \exp\left(-\frac{2n^2\pi^2 t}{3\langle\varphi^2\rangle D}\right), \tag{7.8}$$

where $\langle\varphi^2\rangle = \tau_\nu\langle\theta^2\rangle/3$. When $n_\nu\sigma_\nu t \gg \tau_\nu^2\langle\theta^2\rangle$, which corresponds to long time delays, only the first term of the series is relevant and the probability distribution decreases exponentially. In Ref. [241], this distribution is satisfied for the Brownian motion, where $(1/\sigma_\nu)d\sigma_\nu/d\theta$ follows a Gaussian distribution with mean 0 and variance $\langle\theta^2\rangle$. On the other hand, Ref. [242] derives equation (7.8) under the assumption that the width of the angular distribution of the particles in transit is large when compared to the width of the angular distribution of a single scattering (see Ref. [242] for details on the assumptions). Our simulations show good agreement with equation (7.8) when the angular distribution is assumed to follow a Gaussian distribution for $\tau_\nu = 20$ – 1000.

In Fig. 7.3 we show the time delay distribution for 300 TeV neutrinos and $g = 0.5$, which gives $\lambda_\nu = 10^{24}$ cm. We choose $D = 100$ Mpc to achieve $\tau_\nu = 310$ and the angular distribution used in our simulation follows equation (6.8). We also compare our result with equation (7.8) by setting $\langle\theta^2\rangle = 0.77 m_\nu/E_\nu$, where we assumed $\mathcal{C} = 0.62$, and include the typical delay from equation (7.7). We find that the time delay distribution is significantly different from equation (7.8): while the analytic expression predicts an exponential decay for large time delays, our simulation suggests that $P(t) \propto t^{-2.1}$.

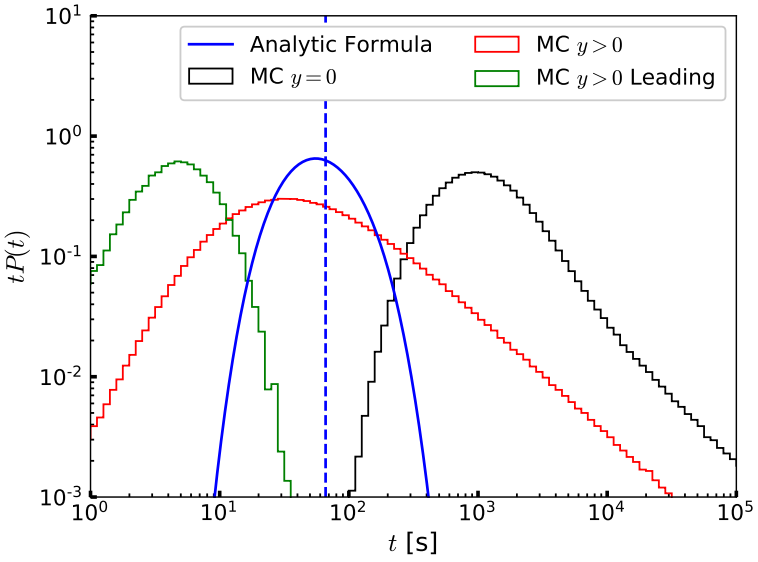

Figure 7.3. Time delay probability density function for the scattering of 300 TeV neutrinos in the $y = 0$ regime, with the CνB at the optical depth $\tau_\nu = 310$. The blue curve is the analytical expression of equation (7.8), while the blue dashed line is the typical delay in equation (7.7). We also include the results from our MC simulations which do include the finite inelasticity.

We note that in the $y = 0$ limit, equation (7.7) underestimates the characteristic time delay in the sense that the expression relies on $\langle\theta^2\rangle$ to be proportional to the mean number of scatterings $\mathcal{M} = \tau_\nu$, which is true in the case of the Gaussian angular distribution. When we use equation (6.8), the tail for large θ is responsible for causing $\langle\theta^2\rangle$ to follow an approximate power law dependence τ_ν^α with $\alpha \approx 1.2$, increasing the typical time delay.

As a comparison, we also include the results from the MC simulations with $y > 0$, allowing for energy losses and upscatterings of CνB neutrinos. In this case, the neutrino time delay distribution can be split into the leading and non-leading components. A leading neutrino is ranked based on its energy; at the injection site, the initial neutrino is considered the leading particle. Whenever a leading neutrino scatters, the most energetic of the two outgoing neutrinos is tagged as the leading particle, while the other is tagged as a non-leading particle. When a non-leading neutrino scatters, both outgoing neutrinos are tagged as non-leading. From this definition, at any point in the cascade development there can only be one leading neutrino. The time delays in $y > 0$ are significantly smaller because neutrinos quickly enter the optically thin regime after a few scatterings, so they do not experience $\mathcal{O}(300)$ scatterings as in the $y = 0$ case. The leading component has

the shortest time delays because the typical scattering angle decreases with ε_ν. In this case, the analytical expression falls in between the $y = 0$ and $y > 0$ regimes.

7.2.3 Scattering in the optically thick limit with finite inelasticity

In realistic scenarios, an incident neutrino loses energy at each scattering, and the energy is transferred to the upscattered neutrino from the CνB. Multiple scatterings then lead to so-called neutrino cascades [64, 65, 244]. In this example we set $g = 0.1$ and $D = 500$ Mpc, and look at the scattering of neutrinos with initial energy $\varepsilon_\nu = 500$ TeV.

We note that as the incident neutrino loses energy and leaves the resonance region, the cross section will continue to decrease. It is therefore possible that a particle may start off in the optically thick regime, yet ending up in the optically thin regime after a few scatterings, when the mean free path exceeds the propagation length. We can select neutrinos that remain in the optically thick regime by choosing an energy window that is sufficiently close to the resonance, thus avoiding the possibility of a neutrino entering the optically thin regime.

In the limit that neutrinos cascade down to energies such that the optical depth is below unity, the shortest time delay can be estimated with the conservative estimate [106],

$$\Delta t \sim \frac{1}{12}\mathcal{M}\langle\theta^2\rangle\lambda_\nu, \tag{7.9}$$

where $\mathcal{M}$ is the mean number of scatterings and can be determined from the MC simulation.

To account for energy losses, we define the effective optical depth $\tau_{\nu\,\mathrm{eff}}$ as the optical depth using the average cross section over the energy window, which we choose as 200 TeV – 500 TeV. The quantity $\tau_{\nu\,\mathrm{eff}}$ is defined for illustrative purposes to explain the physics by using a single optical depth and is not used in the simulations themselves. We show our results in Fig. 7.4, where the source distance $D = 500$ Mpc corresponds to $\tau_{\nu\,\mathrm{eff}} = 600$. The resulting distribution is shown by the black curve and the neutrinos that generate this distribution are mostly leading particles. By definition there are no non-leading particles with energies above $\varepsilon_{\mathrm{res}}/2 = 250$ TeV, because when the first scattering occurs, only the leading neutrino will have energy above 250 TeV. Any non-leading neutrino from the cascade will never have more than half the energy of the initial neutrino. The drop in the distribution for long time delays is caused by the threshold, as particles with less energies are typically the ones with the larger scattering angles and time delays, by virtue of equation (6.8).

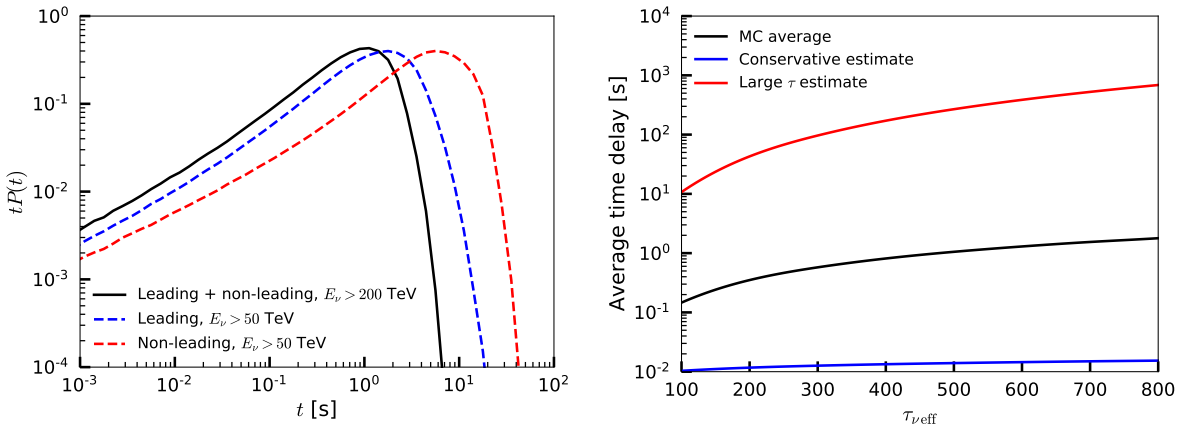

Figure 7.4. Left panel: Time delay probability distribution, scaled by t, for a source distance $D = 500$ Mpc and initial neutrino energy $\varepsilon_\nu = 500$ TeV. The distribution of all particles above 200 TeV (mostly leading particles) is shown by the black curve, as well as the leading and non-leading components for neutrinos with energy above 50 TeV, by the blue and red curves respectively. Right panel: MC average time delay of $E_\nu > 200$ TeV neutrinos, as a function of the effective optical depth in the 200 TeV – 500 TeV energy range. This time delay is compared to the large optical depth estimate and the conservative estimates, given by equations (7.7) and (7.9), respectively.

We also include the leading and non-leading components at energies above 50 TeV. For this threshold we cannot guarantee the optically thick regime, but including these highlight the shift to longer time delays as the energy threshold decreases. As expected, the leading component is associated with shorter time delays when compared to the non-leading.

On the right panel of Fig. 7.4, we compare the average time delay with the estimates provided by equations (7.7) and (7.9). The time delays are given as a function of the effective optical depth in all three cases, using the energy range 200 TeV – 500 TeV. Since almost all the neutrinos in this energy range are leading particles, the MC average will not change if we only consider leading neutrinos. For the conservative estimate, we find that $\mathcal{M}$ increases slowly, from 1.8 at $\tau_{\nu\,\mathrm{eff}} = 100$ to 2.7 at $\tau_{\nu\,\mathrm{eff}} = 800$. For $y = 0$, we would have $\mathcal{M} \propto \tau_\nu$, but in the presence of energy losses, most of the particles that experience multiple scatterings lie below the threshold and are not counted in the calculation of $\mathcal{M}$.

7.2.4 Scattering over cosmological distances

When the source is located at non-negligible redshifts, we must account for neutrino energy losses due to the expansion of the Universe. Here, we use a coupling constant of $g = 0.01$, providing a very small energy window for the neutrino to interact (see Fig. 6.7).

As an example, we consider a neutrino source at $z = 1$, which corresponds to a particle-travel distance of $D = 2.5$ Gpc, emitting 800 TeV neutrinos. Assuming redshift losses only, the neutrino energy reaches $\varepsilon_{\rm res}$ at $z = 0.25$. In the vicinity of $z = 0.25$, a scattering will take place and the neutrino will then lose energy such that it is no longer in the resonance window.

The resulting time delay distribution is presented in Fig. 7.5. Together with the MC simulation, we include the case without the redshift effect, where we ignore redshift loss, but manually change the neutrino energy to $\varepsilon_\nu = \varepsilon_{\rm res}$ at $z = 0.25$ and allow the particle to scatter the CνB. The distribution shown by the red curve shows the redshift effect in the transition from the optically thick to the optically thin regime. We also show the case of the single scattering approximation, which treats the cross section as a Dirac delta function that spikes at $\varepsilon_{\rm res}$, and this is represented by the blue curve. We see that the single scattering approximation correctly predicts the MC results, except for short time delays of $t < 1$ s. In the single scattering approximation, the short time delay portion originates from particles that experience small-angle scatterings and keep their energies very close to $\varepsilon_{\rm res}$ within less than 1%. In reality, these particles should scatter again, since they are still within the resonance region. Upon the second scattering, the time delay is expected to increase, which is why the scenario ignoring redshift losses has a deficit in events with $t \lesssim 0.3$ s. If we then compare the red curve to the MC distribution, we see that this deficit is less significant. Once adiabatic energy losses are considered, small changes in z as the neutrino propagates are enough to shift the energy away from the resonance, and increase the mean free path, facilitating the transition to the optically thin regime.

Our treatment is applicable to cosmological sources as long as particles travel almost along the line of sight. When the scattering angle is not small, due to cosmological expansion, the delay due to one scattering may scale as, e.g., $\propto (1 + z_{\rm sc}) l_{\rm prop}$ instead of the particle-travel distance, where $l_{\rm prop}$ is the proper scattering length and $z_{\rm sc}$ is the redshift where the scattering occurs. However, this effect would increase the delay by $\sim 10\%$ for $z \lesssim 1$.

7.2.5 Applications

7.2.5.1 Source spectra

In the previous section, we have focused on monoenergetic spectra at the source. Here, we analyze effects of neutrino-neutrino scattering assuming an ε_ν^{-2} power law spectrum

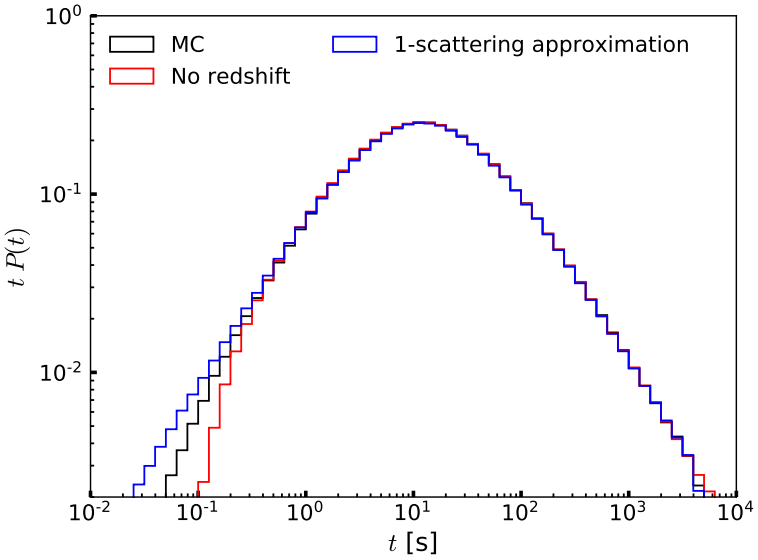

Figure 7.5. Time delay distribution of 800 TeV neutrinos starting at $z = 1$ and scattering off the CνB. The black histogram is the result from our MC simulation. The red histogram is a separate simulation, where redshift energy losses are ignored and the neutrino's energy is manually changed to $\varepsilon_\nu = \varepsilon_{\rm res}$ at $z = 0.25$. The single scattering approximation, which assumes that the cross section is a Dirac delta function spiking at $\varepsilon_{\rm res}$, is shown as the blue histogram.

from a source at redshift $z = 1$ and set a threshold energy of 1 TeV.

As examples, we consider values of the coupling, $g = 0.01, 0.05$ and 0.2, as they represent the $\tau_\nu \ll 1, \tau_\nu \sim 1$ and $\tau_\nu \gg 1$ regimes in the 100 TeV–1 PeV range, as shown in Fig. 7.6. The results from the MC simulations are shown by the blue curves, while separate simulations ignoring redshift effects, meaning no expansion losses and assuming a uniform CνB number density of 112 cm^{-3}, are shown by the red curves.

Starting with $g = 0.01$, we see that the time delay distribution close to the $tP(t)$ peak is not very sensitive to redshift effects and $P(t) \propto t^{-2}$ past the peak. Below the peak, we see there are more events with $t < 1$ s when we neglect redshifts. In the absence of redshifts there is a sharp decrease at 500 TeV due to the resonance, together with the corresponding pileup in the 400 TeV region. This occurs over a very narrow energy region, and the pileup is not very significant because few neutrinos lie in the resonance windows. In the realistic scenario we see the expected decrease in the normalization, with $E_\nu^2 \Phi_\nu$ scaling as $1/(1+z)$. The pileup region shifts towards lower energies, and the peak is more prominent. Because neutrinos from the higher-energy tail get redshifted into the resonance region and scatter, it follows that the total number of scattered neutrinos in the presence of redshift is larger than the case without. There is also a distinct break

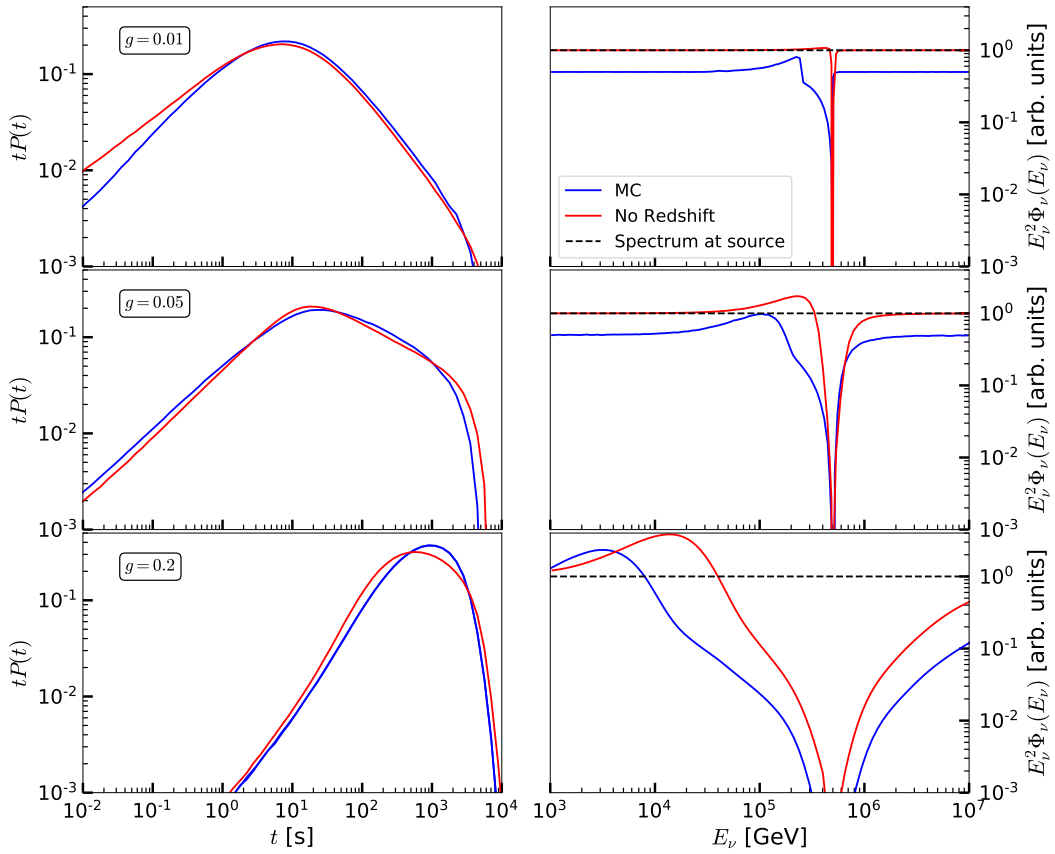

Figure 7.6. Time delay distributions (left panels) and observed energy spectra (right panels) of an ε_ν^{-2} source at $z = 1$, for coupling constants $g = 0.01, 0.05$ and 0.2 (top,middle and bottom row, respectively). The source spectrum is normalized such that $\varepsilon_\nu^2 \Phi_\nu = 1$. The blue curves represent the results of our MC simulation, while the red curves correspond to a case where the redshift energy loss and CνB density dependence on z are neglected. The dotted black lines in the energy spectra are the neutrino spectra at the source.

in the spectrum at the 250 TeV mark, which is understood by differentiating between scattered and unscattered neutrinos. The component of the initial ε_ν^{-2} spectrum that was below 500 TeV remains unscattered and is simply redshifted to 250 TeV and below. On the other hand, neutrinos between 500 TeV and 1 PeV will eventually scatter as they get redshifted into the resonance window, while those above 1 PeV are redshifted to a minimum energy of 500 TeV and do not interact. Therefore, the observed energy spectrum of unscattered neutrinos is an ε_ν^{-2} spectrum with a gap in the 250 TeV– 500 TeV region, which is to be filled by the scattered component. For couplings this small, there are not enough upscattered neutrinos to cover this gap, causing the discontinuity.

For $g = 0.05$ we have multiple scatterings, typically four to five, which causes the $tP(t)$ peak to appear at $t \approx 20$ s. For long time delays, we also see a sudden drop

around 5000 s. This is caused by the 1 TeV energy threshold, which removes lower-energy neutrinos that would have a larger scattering angle and longer time delay. The energy spectrum shows features similar to $g = 0.01$, but the pileup region is wider as a result of multiple scatterings. The spectrum between 100 and 500 TeV in the MC case is dominated by the scattered component, so we no longer see the break in the spectrum observed when $g = 0.01$.

The case where $g = 0.2$ shows a large separation in the time delay distribution peaks between the redshift and no redshift cases. Here, the number of neutrino scatterings is much higher, many of them experiencing over 15 scatterings. In this case, redshift losses decrease the neutrino energy before the next scattering takes place, at which point larger scattering angles are preferred, according to equation (6.8). The threshold effect on the delay distribution occurs close to 10^4 s, but does not have an effect on the location of the distribution peaks, which is also true for $g = 0.05$ and $g = 0.01$. Setting the energy threshold to 10 TeV, however, would shift the peak locations to lower t for $g = 0.2$ only. Looking at the energy spectrum, we see that the pileup region is much wider. We also note that $E_\nu^2 \Phi_\nu$ is no longer flat in the 1 TeV region and the MC result overcomes the no redshift case at low energies. Now that the number of scatterings is so large, particle multiplicity allows the MC peak to compensate for the redshift factor $1/(1 + z)$. On the other hand, there is a drop in the case without the redshift effect, because TeV neutrinos experience scatterings at such large couplings, and the higher-energy neutrinos that cascade downward are unable to compensate. After repeating these simulations with the inclusion of the $t-$channel contributions to the cross section, we find negligible differences for $g = 0.01$ and $g = 0.05$ and a slight shift to longer time delays for $g = 0.2$. The differences only appear at large couplings, where the resonance width is large and the $t-$channel term is comparable to the $s-$channel away from ε_{res}.

7.2.5.2 Flavors

If we consider three neutrino flavors, the cross section has to be modified for different mass eigenstates m_i. The oscillation parameters are fixed to the best-fit oscillation results from NuFIT 2021 [29, 180]. While there are three mass eigenstates, neutrino oscillation data tell us that two of these are close together. We should then expect two well-separated resonance dips. To comply with the cosmological bound of $\sum m_\nu < 0.12$ eV [126], we choose the masses $m_1 = 0.022$ eV, $m_2 = 0.024$ eV and $m_3 = 0.055$ eV. In addition, to obtain the dips in the energy spectrum between 100 TeV and 1 PeV, we choose $m_\phi = 5$ MeV.

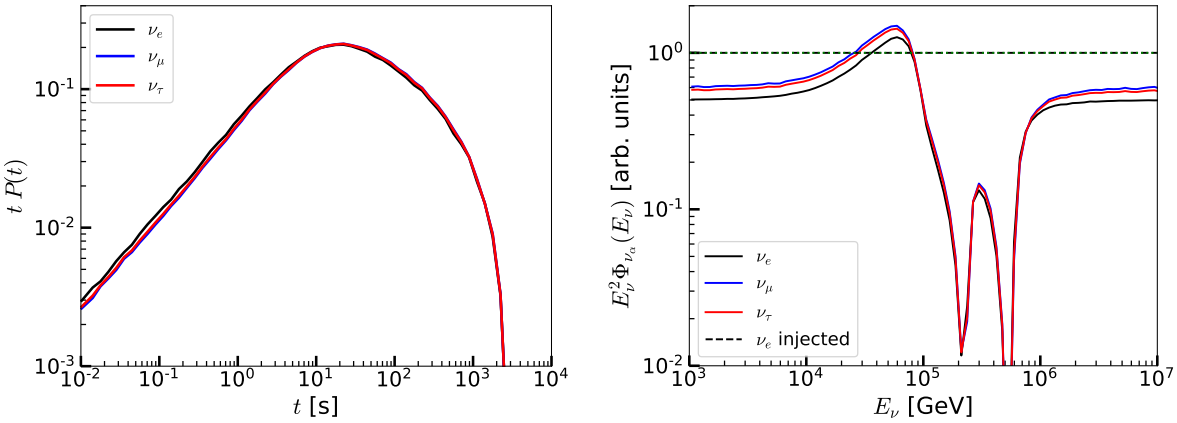

Figure 7.7. Time delay distributions (left panel) and observed energy spectra (right panel) of an ε_ν^{-2} source at $z = 1$, for $g_{\tau\tau} = 0.05$ and $m_\phi = 5$ MeV. The source spectrum is normalized such that $\varepsilon_\nu^2 \Phi_{\nu_e} = 1$.

The CνB density for each mass eigenstate is $112(1+z)^3$ cm^{-3}, as before. Regarding the ε_ν^{-2} source at $z = 1$, we will assume that the flavor ratio at the source is (1:2:0), which quickly decoheres into mass eigenstates as the neutrino oscillation and coherence lengths are shorter than the interaction length. The propagation and interactions can thus be carried out in the mass eigenstate basis and then converted to the flavor eigenstate basis when it reaches the source.

The neutrino coupling now becomes a 3×3 coupling matrix, and we assume the coupling only for ν_τ: $g_{\alpha\beta} = \mathrm{diag}(0, 0, g_{\tau\tau})$. Such secret neutrino interactions involving only ν_τ are of interest as they are the least constrained by laboratory experiments [22]. Under this assumption, the invariant cross section for the process $\nu_i \nu_j \longrightarrow \nu_k \nu_l$ is [63]

$$\sigma_\nu^{ijkl} = \frac{|U_{\tau i}|^2 |U_{\tau j}|^2 |U_{\tau k}|^2 |U_{\tau l}|^2 g_{\tau\tau}^4}{32\pi} \frac{s_j}{(s_j - m_\phi^2)^2 + m_\phi^2 \Gamma_\phi^2}, \tag{7.10}$$

where $s_j = 2 m_j E_\nu$, $\Gamma_\phi = g_{\tau\tau}^2 m_\phi / 16\pi$ and U is the Pontecorvo-Maki-Nakagawa-Sakata matrix.

The results of the MC simulation are shown in Fig. 7.7 for $g_{\tau\tau} = 0.05$. The energy spectrum shows two dips due to the three resonances. Besides that, the spectral shape is about the same for all three neutrino flavors, separated by factors which correspond to the observed flavor ratio at Earth after oscillations are averaged out. When a scattering takes place, the outgoing mass eigenstates ν_k and ν_l depend on $|U_{\tau k}|^2$ and $|U_{\tau l}|^2$ only. For our choice of oscillation parameters, we have $|U_{\tau 1}|^2 < |U_{\tau 2}|^2 < |U_{\tau 3}|^2$. As a result, there is a slight tendency for ν_3 to be produced over the other states, which builds up

over several scatterings, creating the deficit in ν_e when we convert the ν_3 flux to a flavor flux. Our results on the spectra are consistent with those by Ref. [63].

For the time delay, the delay distributions are almost identical. One could see that $P(t)$ is slightly larger for ν_e in the 0.01 s – 1 s range. This part of the distribution comes from neutrinos that only scatter once, while the long time-delay tail consists of particles that scatter multiple times.

7.3 Summary and Conclusions

We have presented a numerical study of secret neutrino interactions of TeV–PeV neutrinos and their associated time delays. We developed a MC simulation code that accounts for the sudden changes in the s-channel interactions as we approach the resonance energy, allowing us to accurately calculate the scattering locations. The developments can be applied to various astrophysical neutrino sources, by which constraints on νSI can be placed with neutrino data (see Ref. [117] as an application to the Galactic supernova).

As the first example, we have shown that in the optically thin limit the simulation result is in agreement with the analytical expression. Deviations from it become apparent at $\tau_\nu \sim 0.1$, when multiple scatterings become more relevant. In the optically thick limit with $y = 0$, there is a significant difference in the time delay distribution between our result from the MC simulation and the analytical expression, because the angular distribution is not a Gaussian. The case $y = 0$ predicts longer delays than $y > 0$ as energy losses allow particles to leave the resonance window, causing less scatterings to take place. In the case $\tau_\nu \gg 1$ and $y > 0$, we have found that the time delay distribution is also sensitive to the energy threshold: lowering it leads to the inclusion of the lower-energy particles that experience more scatterings and longer time delays. A clear separation between the distribution peaks for leading and non-leading components is seen at an energy threshold of 50 TeV. The characteristic time delays in the MC simulations are found to lie between the large optical depth and conservative estimates.

Considering sources at cosmological distances, we have shown that for a source at $z = 1$ and the coupling strength $g = 0.01$, redshift effects are most important for neutrinos in the short time-delay tail. We have also highlighted the difference between the MC simulation and the single scattering approximation, and the latter predicts more events in the short time-delay tail, compared to the former. For a source at redshift $z = 1$ with an ε_ν^{-2} spectrum, the observed neutrino spectrum presents the expected pileup region below the resonance energy. As the coupling strength increases, the resonance width

increases and the location of the pileup moves to lower energies. Breaks in the spectrum at coupling strengths $g = 0.01$ and $g = 0.05$ are present, at energies slightly above the pileup region, where the scattered and unscattered components of the spectrum intersect. This effect is not present when we ignore redshift effects. The time delay distributions for larger couplings lead to longer delays, as more scatterings occur, with delays of approximately 1 hour for $g = 0.05$.

The MC simulation code developed in this work can also be applied for a broader set of BSM interactions. As long as the small-angle scattering approximation is satisfied, then the MC code presented here can be applied to neutrino scattering with dark matter or axions, as discussed in Refs. [106, 245]. Other BSM interactions which produce SM particles such as muons and pions, which decay into neutrinos, can also be accommodated readily. The code is expected to be publicly available in the near future.

Chapter 8
Time-delayed neutrino emission from supernovae as a probe of dark-matter neutrino interactions

In this chapter we will apply the time delay approach described in chapter 7 and use it in the context of supernova neutrinos. The ~ 10 MeV neutrinos will interact with galactic DM and be delayed. We look at the delayed signal and how it can be used to constrain neutrino-DM scattering. The text in this chapter is part of the work in Ref. [117].

8.1 Method

We consider a neutrino emitted by a source at a distance D, propagating through a bath of DM particles χ. We define the optical depth $\tau = n_\chi \sigma_{\nu\chi} D$, where n_χ is the DM number density and $\sigma_{\nu\chi}$ is the total cross section for DM-neutrino interaction. Suppose that the interactions happen in the optically-thin limit, i.e., $\tau \ll 1$, such that neutrinos would at most experience one interaction as they travel towards the Earth. In this limit, if N neutrinos are emitted at the source, the majority will arrive together, while a fraction of $\sim \tau N$ neutrinos will scatter and arrive later because of the increased trajectory length [106]. The time delay t for the arrival of scattered neutrinos depends on the scattering angle, with a typical delay Δt given by [106]

$$\Delta t \approx \frac{1}{2}\frac{\langle\theta^2\rangle}{4} D \simeq 1.3 \times 10^7 \mathrm{s} \left(\frac{\langle\theta^2\rangle}{10^{-4}}\right)\left(\frac{D}{10\,\mathrm{kpc}}\right), \tag{8.1}$$

where $\langle\theta^2\rangle$ is the mean of θ^2, for a given differential cross section, and θ is the scattering angle. See also Refs. [116, 243].

In the SN frame, DM is at rest and the incident neutrino's energy is E_ν. For a scattering angle θ, the scattered energy E'_ν is given by

$$E'_\nu = \frac{E_\nu m_\chi}{m_\chi + E_\nu(1-\cos\theta)}, \tag{8.2}$$

where m_χ is the DM mass and we neglect neutrino mass. The differential cross section for a neutrino of incident energy E_ν to have a scattered energy E'_ν is

$$\frac{d\sigma_{\nu\chi}}{dE'_\nu}(E_\nu, E'_\nu) = \frac{d\sigma_{\nu\chi}}{d\cos\theta}\frac{d\cos\theta}{dE'_\nu}, \tag{8.3}$$

where

$$\frac{d\sigma_{\nu\chi}}{d\cos\theta} = \frac{1}{32\pi m_\chi^2}\left(\frac{E'_\nu}{E_\nu}\right)^2 |\mathcal{M}|^2. \tag{8.4}$$

Here the squared matrix element $|\mathcal{M}|^2$ depends on particle physics models that we discuss below. We will explore the range of mediator masses $\in [1\,\text{eV}, 100\,\text{MeV}]$ and $m_\chi \in [10\,\text{eV}, 100\,\text{keV}]$ in this work.

We consider three particle physics models in this work. First, we consider fermionic DM that interacts via a vector mediator V_μ, and the interaction Lagrangian of the form

$$\mathcal{L}_{\text{int}} \supset g_\nu \bar{\nu}\gamma^\mu \nu V_\mu + g_\chi \bar{\chi}\gamma^\mu \chi V_\mu, \tag{8.5}$$

where g_ν and g_χ are dimensionless coupling constants of the vector mediator to neutrinos and DM, respectively. Neutrino coupling to a vector mediator has also been used for example in the gauged $U(1)_{L_\mu - L_\tau}$ model [28, 246, 247]. DM couplings to vector mediators have also been considered in the cosmological context [98, 101, 248]. The Lagrangian in equation (8.5) implies that DM-neutrino scatterings are mainly forward scatterings, allowing us to remain within the small-angle scattering approximation. In addition, m_V has little effect on the angular distribution for $m_V > 5$ MeV.

In addition to the Lagrangian in equation (8.5), we will also consider fermionic DM with a scalar mediator

$$\mathcal{L}_{\text{int}} \supset g_\nu \bar{\nu}\nu\phi + g_\chi \bar{\chi}\chi\phi, \tag{8.6}$$

and scalar DM with a scalar mediator

$$\mathcal{L}_{\text{int}} \supset g_\nu \bar{\nu}\nu\phi + g_\chi \Lambda\chi^*\chi\phi. \tag{8.7}$$

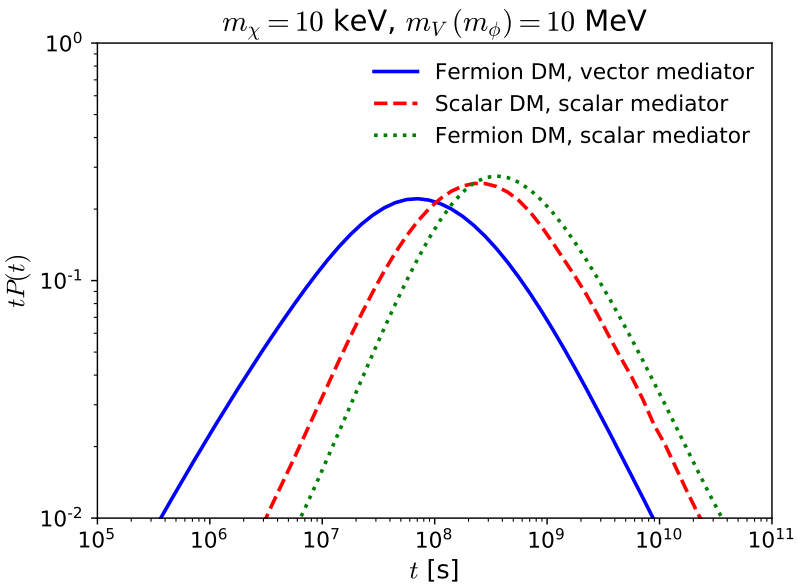

Figure 8.1. Time delay distribution of 15 MeV neutrinos for $m_\chi = 10$ keV and a 10 MeV mediator. The distribution is multiplied by t. For each model, g_χ and g_ν have been chosen such that $\tau = 10^{-3}$ for $D = 10$ kpc. These results are, in fact, independent of τ, provided that $\tau \ll 1$

The differential and total cross sections for these interactions can be found in Ref. [104]. For the last Lagrangian, we note that the coupling is split into a dimensionless coupling g_χ and an energy scale $\Lambda = 100$ GeV. In scalar mediator models, if neutrinos are Dirac fermions we would need to consider mixing with sterile states; for Majorana neutrinos, $\bar{\nu}\nu$ should be interpreted as $\overline{\nu}^c_L \nu_L/2 + \text{c.c.}$ For example, DM interactions with scalar mediators arise in Standard Model extensions, where DM couples to the Higgs sector and protected by a $\mathbb{Z}_2$ symmetry [249]. This leads to Higgs portal models for fermionic DM [82] or scalar DM [249, 250] after the spontaneous electroweak symmetry breaking.

Let $P(t)$ be the probability density function of the neutrino time delay t of the neutrinos within the arrival energy range of interest. By working in the $\tau \ll 1$ limit, $P(t)$ depends on $(1/\sigma_{\nu\chi})d\sigma_{\nu\chi}/d\cos\theta$ and is therefore independent of the coupling strength [106, 242, 243]. In Fig. 8.1 we show the time delay distribution of neutrinos with an initial energy of 15 MeV, a dark matter mass $m_\chi = 10$ keV and a 10 MeV mediator. Each model has values of g_χ and g_ν such that $\tau = 10^{-3}$, in the optically-thin regime. Here we see that among the three models, the fermionic DM with a vector (scalar) mediator yields shorter (longer) time delays. This is related to the details of the angular distribution of the model, where smaller scattering angles lead to shorter time delays. For fermionic DM with a scalar mediator, we see that the ΔT decreases for DM masses above 100 keV

and m_ϕ in the 100 eV – 10 keV range. This decrease is caused by the energy threshold used in the analysis, which we address in the next section.

In order to estimate the temporal profile for the arrival of neutrinos from a SN, we adopt a SN neutrino spectrum at the source of the form [140, 251, 252],

$$\Phi_\nu(E_\nu) = \frac{L_\nu}{\langle E_\nu \rangle^2} \frac{(\alpha+1)^{\alpha+1}}{\Gamma(\alpha+1)} \left(\frac{E_\nu}{\langle E_\nu \rangle} \right)^\alpha \exp\left(-\frac{(\alpha+1)E_\nu}{\langle E_\nu \rangle} \right), \tag{8.8}$$

where $\langle E_\nu \rangle$ is the average neutrino energy, α is the pinching parameter, $L_{\bar{\nu}_\alpha}$ is the neutrino luminosity, and Γ is the Euler Gamma function. Hereafter, we assume $\alpha = 2.3$ and $\langle E_\nu \rangle = 16$ MeV, although in general the values of α and $\langle E_\nu \rangle$ are different among neutrino flavors [140]. The total neutrino energy is set to $\mathcal{E}_\nu = L_\nu T_{\rm dur} = 3 \times 10^{53}$ erg, where $T_{\rm dur} = 10$ s is the duration of the neutrino emission.Neutrino emission consists of several stages. Around the core bounce, the so-called ν_e neutronization burst is expected, which lasts for ~ 20 ms. This is followed by the accretion phase with significant production of ν_e and $\bar{\nu}_e$, which lasts for a few seconds (e.g., [253–255]). Then, the protoneutron star cools and neutrino luminosities of all flavors become similar, lasting for $\sim 10 - 100$ s (e.g., [251, 256, 257]). The total energy we are considering here can also be matched to the simulation results presented in Ref. [258] within 1 s after the bounce.

The supernova spectrum consists of $\bar{\nu}_e$ and $\bar{\nu}_x$ (non-electron antineutrinos). We assume that both fluxes are related by $\Phi_{\bar{\nu}_x} = 0.3\Phi_{\bar{\nu}_e}$ [255], such that they have the same production spectra. This assumption is made for simplicity because using separate spectra would require us to look at $\bar{\nu}_e$ and $\bar{\nu}_x$ with different pinching parameters α. The flux is normalized so the total neutrino energy in all three flavors is equal to $\mathcal{E}_\nu$. For pure adiabatic transitions, the fluxes at the surface of the star are $\Phi_{\bar{\nu}_1} = \Phi_{\bar{\nu}_e}$ and $\Phi_{\bar{\nu}_2} = \Phi_{\bar{\nu}_3} = \Phi_{\bar{\nu}_x}$, assuming normal mass ordering [259]. The $\bar{\nu}_e$ flux on Earth becomes $\Phi_{\bar{\nu}_e} = \sum_i \Phi_{\bar{\nu}_i} |U_{ei}|^2$, where U is the neutrino mixing matrix.

For a nearby SN of $D \sim \mathcal{O}(10)$ kpc, we can assume a local DM density $n_\chi = 0.3$ cm$^{-3}(m_\chi/1\,\text{GeV})^{-1}$. As we show in our results, within our parameter space the typical time delays would lie in the 10^2-10^8 s range. While the SN neutrino spectrum is time-dependent (see e.g., Ref. [258]), the characteristic time delays are much longer than $T_{\rm dur}$, so we use the time-integrated flux on Earth

$$\frac{dN_\nu}{dE_\nu} = \frac{\Phi T_{\rm dur}}{4\pi D^2}. \tag{8.9}$$

The number of neutrino events in Hyper-Kamiokande is

$$N_{\rm events} = N_{\rm T} \int_{10\,{\rm MeV}}^{50\,{\rm MeV}} \frac{dN_{\bar{\nu}_e}}{dE_{\bar{\nu}_e}} \sigma_{\rm QE}(E_\nu) dE_{\bar{\nu}_e}, \tag{8.10}$$

where $N_{\rm T}$ is the number of targets (1.25×10^{34} for the 187 kton HK detector fiducial volume [258]) and $\sigma_{\rm QE}$ is the quasi-elastic inverse beta decay cross section. We have assumed 14 MeV as the neutrino energy threshold. These are the total number of events, which accounts for both scattered and unscattered neutrinos. For our chosen parameter set, we get $N_{\rm events} = 48200$. This is consistent with Ref. [258], which obtained $N_{\rm events} \approx 20000$ for $T_{\rm dur} = 500$ ms, although we use a larger total neutrino energy (in all flavors) of $\mathcal{E}_\nu = 3 \times 10^{53}$ erg.

To calculate the delayed neutrino spectrum $dN_{\rm scatt}/dE_\nu$, which is the time-integrated spectrum of all scattered neutrinos, we use

$$\frac{dN_{\rm scatt}}{dE_\nu} = \int_0^\infty dt \int_{E_\nu}^{E_\nu'^{\rm max}(E_\nu,t)} dE'_\nu \frac{dN_\nu}{dE'_\nu} P(t, E'_\nu) \frac{d\sigma_{\nu\chi}}{dE_\nu}(E'_\nu, E_\nu) n_\chi D, \tag{8.11}$$

where the integrand is the product of the SN spectrum at E'_ν and the probability that a neutrino of energy E'_ν scatters once and arrives with an energy E_ν, in the optically-thin limit. The spectrum dN_ν/dE_ν is inserted into equation (8.10) to obtain the number of events that undergo scatterings. We point out that the relationship between $N_{\rm scatt}$ and $N_{\rm events}$ is not trivial due to the threshold, as some of the scattered neutrinos will fall below that energy, but the relationship $N_{\rm scatt} \sim \tau N_{\rm events}$ provides an order of magnitude estimate. We may write $N_{\rm scatt} = \kappa\tau N_{\rm events}$, where κ is the fraction of scattered events with $E_\nu > 14$ MeV and is determined from simulations. Given that effects of $P(t, E_\nu)$ and $E_\nu'^{\rm max}$ are included in κ, the rest will only depend on m_χ and the mediator mass when $\tau \ll 1$. Within this approximation, for fixed DM and mediator masses, we have $N_{\rm scatt} \propto g_\nu^2 g_\chi^2 L_\nu T_{\rm dur}/D$.

We constrain the (g, m_V, m_χ) parameter space under the assumption that no significant background excess has been observed within a time window ΔT after the SN neutrino burst is detected.

We use the Feldman-Cousins upper limits [260] to obtain constraints on the parameters of DM-neutrino interactions. The background rate is obtained from the different channels provided in [261]: invisible muons, neutral current, atmospheric neutrinos, lithium, reactor neutrinos and diffuse supernova neutrinos. For a 187 kton detector with Gadolinium in the energy range [14 MeV, 50 MeV], the total rate would be 3.41×10^{-6} Hz. We use this

rate to estimate the expected number of background events μ_b over a time ΔT after the MeV burst. Starting from the arrival time of the unscattered signal, we take the time window ΔT that encloses a factor $0 < \beta \leq 1$ of N_{scatt}. Our calculations of ΔT enforce an $E_\nu > 14$ MeV threshold. The different interaction models affect ΔT only through the distribution $P(t)$, so the choice of time window depends on DM and mediator masses only. Within this ΔT, we find the Feldman-Cousins upper limit μ_s, assuming that the expected number of events is μ_b (i.e., background only) and the observed number of events is also μ_b. This μ_s would then correspond to the expected number of delayed neutrino events within ΔT. We set $\mu_s = \beta N_{\text{scatt}}$ and adjust $g_\nu^2 g_\chi^2$ to get this equality to hold. This equation for μ_s relies on the scaling of $N_{\text{scatt}} \propto g_\nu^2 g_\chi^2$, which is only valid in the optically thin regime. Therefore, this method cannot be applied for $\tau \geq 1$. Within the parameter space shown in Fig. 8.2, only the fermion DM with a scalar mediator has such a region for $m_\chi > 0.8$ MeV and $m_\phi \gtrsim 10$ MeV. In the case of heavier dark matter $m_\chi \gtrsim 100$ keV, $\Delta T > 10^8$ s for heavy mediators. For these cases, we set $\Delta T = 10^8$ s and adjust β accordingly.

8.2 Results

We calculate the 95% confidence level (CL) upper limit on the coupling constant in Hyper-Kamiokande in the event of a 10 kpc SN, assuming no significant delayed neutrino signal is detected. For this purpose, we define the effective coupling $g = (g_\nu g_\chi)^{1/2}$, and set $\beta = 0.5$. Our choice of β is motivated by the Monte Carlo simulation results [116] which suggest that ΔT will coincide with the peak of the $tP(t)$ distribution (see Fig. 8.1 as an example). We show the upper limit on the coupling for different DM and mediator mass in Fig. 8.2. We mark the set of points for which $\Delta T = 10^8$ s and $\Delta T = 10$ s, where the latter corresponds to the duration of the neutrino emission. We consider a maximum time window of 10^8 s as this leads to exceedingly long delays. In this sense, we are only truly sensitive to DM lighter than 1 MeV for heavy mediators, where $\Delta T < 10^8$ s. We also shade the region where $\tau \geq 1$, where the optically thin approximation is not satisfied and our results are not applicable. This region is only present within our parameter space when we assume fermionic DM with a scalar mediator. For fermionic DM and a vector mediator, we see that when $m_{\text{V}} \lesssim 100\,\text{eV}$, the time window used is too short for the delayed signal to be well separated from the initial MeV burst. This is not the case for scalar mediators, where the scattering angles remain relatively large for very light scalars.

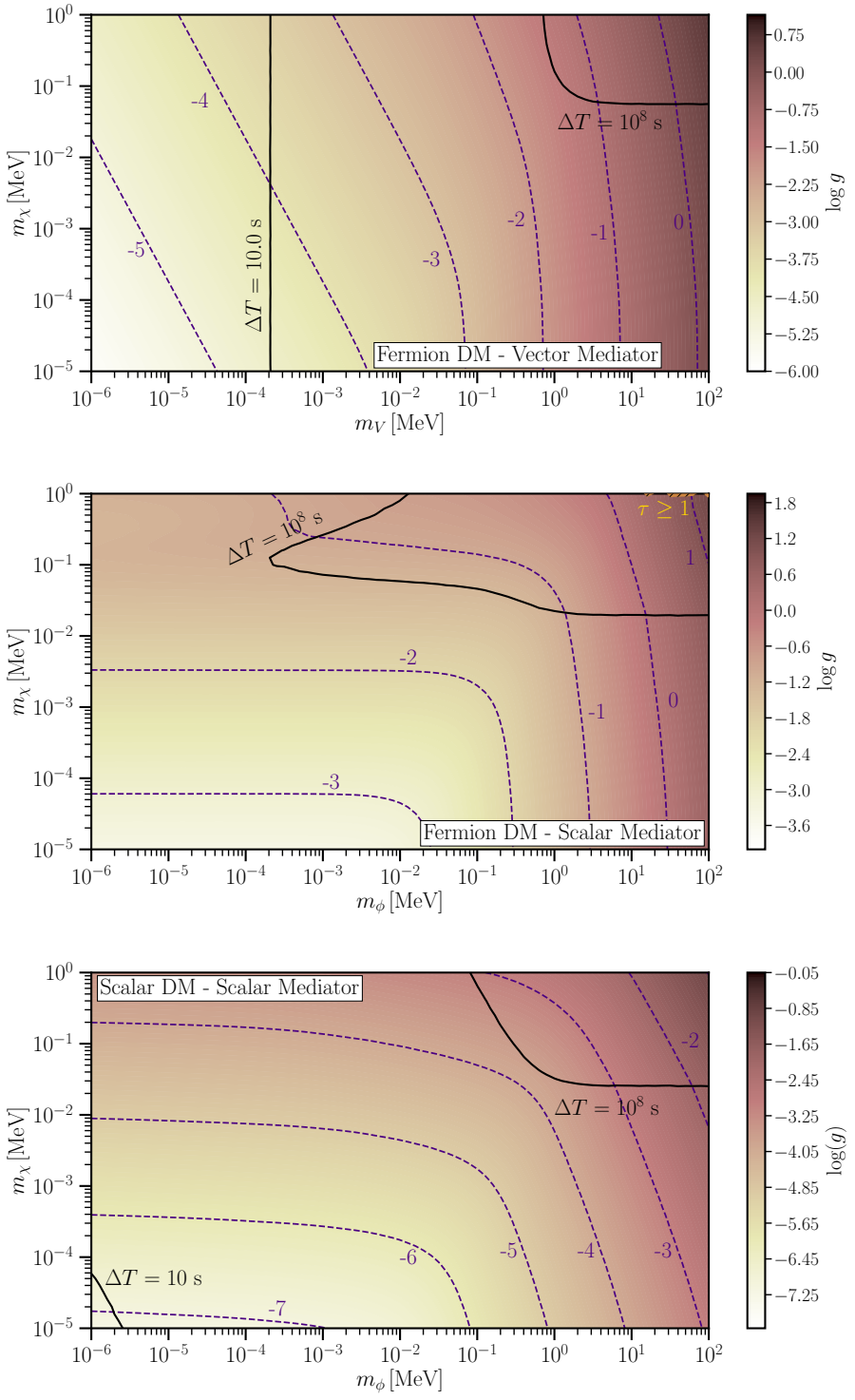

Figure 8.2. Neutrino-DM coupling constraints on $g = (g_\nu g_\chi)^{1/2}$ for the models described by equations (8.5) (top), (8.6) (middle) and (8.7) (bottom). The time window ΔT is the time taken to enclose 50% of the scattered neutrinos with energy above 14 MeV. The region $\tau \geq 1$ has been shaded for the Fermion DM and Scalar Mediator case. This is a very small region in the top right corner. The other models do not have $\tau \geq 1$ within the parameter space shown.

We also compare our constraints against limits from other observables. The first one is the neutrino self-interaction bound $g_{\tau\tau} < 0.27$ from [22], which only applies to ν_τ coupling. To convert $g_{\tau\tau}$ into an effective coupling $g_\nu^{\rm eff}$ and then into the ν-DM coupling g, we proceed as follows. The $\bar{\nu}_e$ flux from $\nu-$DM scatterings, $\Phi_{\bar{\nu}_e,\rm scatt}$, is given by the probability that $\bar{\nu}_i$ interacts via $g_{\tau\tau}$, becomes $\bar{\nu}_j$ and is detected on Earth as $\bar{\nu}_e$. In the limit $\tau \ll 1$, this probability is simply an effective optical depth. We then write $\Phi_{\bar{\nu}_e,\rm scatt} = \sum_i \tau_i \Phi_{\bar{\nu}_i}$, which is the sum of fluxes of scattered $\bar{\nu}_i$ which are detected as $\bar{\nu}_e$. With the assumption that $\bar{\nu}_e$ and $\bar{\nu}_x$ are proportional to each other, we may also simplify this expression to $\Phi_{\bar{\nu}_e,\rm scatt} = \tau^{\rm eff}\Phi_{\bar{\nu}_e}$ for an effective optical depth

$$\tau^{\rm eff} = n_\chi \sigma_{\nu\chi}^{\rm eff} D = n_\chi \frac{\sigma_{\nu\chi} D}{g_\nu^2} \sum_{i,j} |U_{ej}|^2 |U_{\tau j}|^2 |U_{\tau i}|^2 g_{\tau\tau}^2 P_i, \tag{8.12}$$

where $P_i = \Phi_{\bar{\nu}_i}/\Phi_{\bar{\nu}_e}$. Note that the cross sections involved have negligible contributions from neutrino mass, so $\sigma_{\nu\chi}$ is the same regardless of the neutrino mass eigenstate involved. The cross section $\sigma_{\nu\chi}^{\rm eff}$ is now proportional to $(g_\nu^{\rm eff})^2$. We can thus absorb neutrino mixing effects into this coupling, such that

$$(g_\nu^{\rm eff})^2 = g_{\tau\tau}^2 \sum_{i,j} |U_{ej}|^2 |U_{\tau j}|^2 |U_{\tau i}|^2 P_i. \tag{8.13}$$

With the current values of the oscillation parameters, this leads us to $g_\nu^{\rm eff} = 0.1$. To get the upper bound of g, we use $g_\nu^{\rm eff}$ together with the upper bound $g_\chi < 4\pi$ originating from the perturbative limit. This then leads to a bound $g < \sqrt{4\pi g_\nu^{\rm eff}} = 1.11$.

We also have the BBN constraint on mediator masses, given in [22, 28]. Finally, we also consider the constraints for merging galaxy clusters, which requires $\sigma_{\chi\chi}/m_\chi < 0.1$ cm^2 g^{-1} [262, 263]. Here $\sigma_{\chi\chi}$ is DM self-scattering cross section in the low velocity limit. The cluster constraints provide upper bounds on g_χ for fixed DM and mediator masses. To convert this into a bound for g, we need to assume a ratio g_ν/g_χ. Since the constraints are on g_χ only, choosing small (large) g_ν/g_χ will strengthen (weaken) the bounds on g.

In Fig. 8.3, we show the 2D projections for selected DM masses assuming fermionic DM and show the aforementioned bounds from laboratory measurements, BBN and cluster constraints. For the case of fermionic DM, we take $g_\nu/g_\chi = 1/125$, the ratio corresponding to $g_\chi = 4\pi$ and $g_\nu = 0.1$. For this choice, our constraints are stronger than laboratory and cluster bounds for $m_\chi < 20$ keV ($m_\chi < 1$ keV) for a vector (scalar) mediator. In the case of scalar DM with a scalar mediator, as shown in figure 8.4, we find that the cluster bounds required a g_ν/g_χ ratio above 10^4 for the echo limits to be

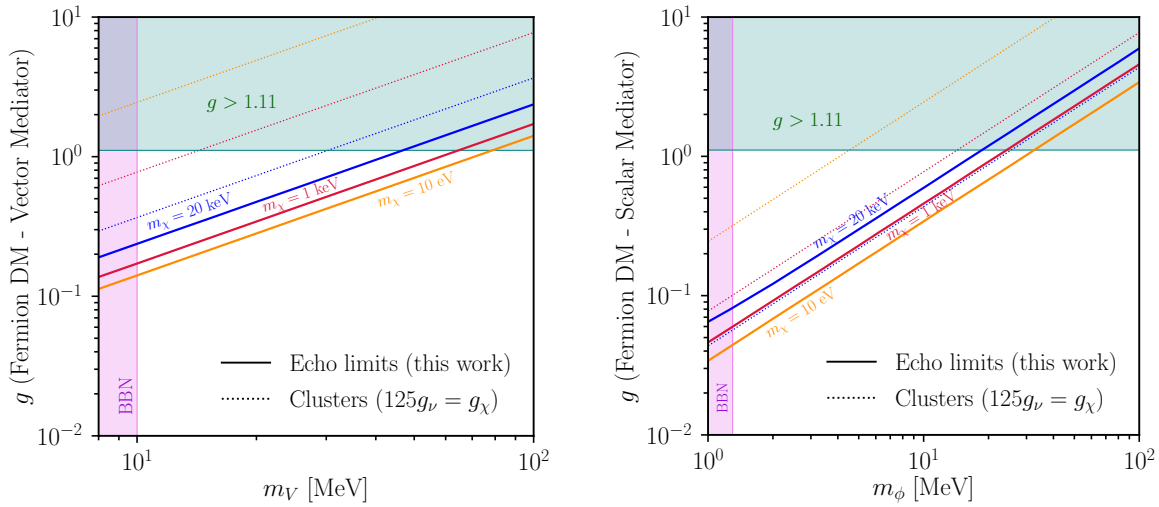

Figure 8.3. Neutrino-DM coupling constraints on $g = (g_\nu g_\chi)^{1/2}$ for the models described by equations (8.5) (left panel) and (8.6) (right panel). Cluster constraints are shown as dotted lines for each DM mass, assuming $125g_\nu = g_\chi$, corresponding to the ratio of $g_\nu = 0.1$ and $g_\chi = 4\pi$. BBN nucleosynthesis constraints [22, 28] correspond to the shaded region (magenta).

competitive. For these large ratios, we easily reach the laboratory bound on g_ν, as shown by the dashed lines. In the end, our constraints are stronger than laboratory and cluster bounds when $m_\phi \lesssim 3$ MeV for $g_\nu/g_\chi = 7 \times 10^4 (g_\nu/g_\chi = 5 \times 10^5)$ for $m_\chi = 20(1)$ keV. For $m_\chi = 10$ eV and $g_\nu/g_\chi = 3 \times 10^7$, laboratory bounds are stronger than our bounds when $m_\phi \gtrsim 1.3$ MeV. Overall, given the BBN bound, there is a limited range of m_ϕ, in which the constraints in our work are the strongest.

If the water detector does not have Gadolinium, the energy threshold would be at around 17 MeV, since below it the spallation background is large [261]. Taking this energy threshold into account, the background is dominated by invisible muons, increasing μ_b. Likewise, the increased energy threshold means that a larger fraction of the scattered events will lie below it. In this scenario, depending on m_χ and mediator mass, we may require up to 3 times as many scattered events. In turn, the couplings presented in our results would have to be increased by up to 30%.

A general feature is that for a fixed m_χ, the constraint on the coupling weakens for larger mediator masses. The delayed neutrino spectrum is proportional to $\sigma_{\nu\chi}$ in the small optical depth limit, so a larger value of g is needed to account for heavier mediators. On the other hand, for a fixed mediator mass, the constraint gets weaker for heavier DM and this weakening becomes more dramatic for lighter mediators. The total cross section monotonically decreases with m_χ, which contributes to weaker constraints. In

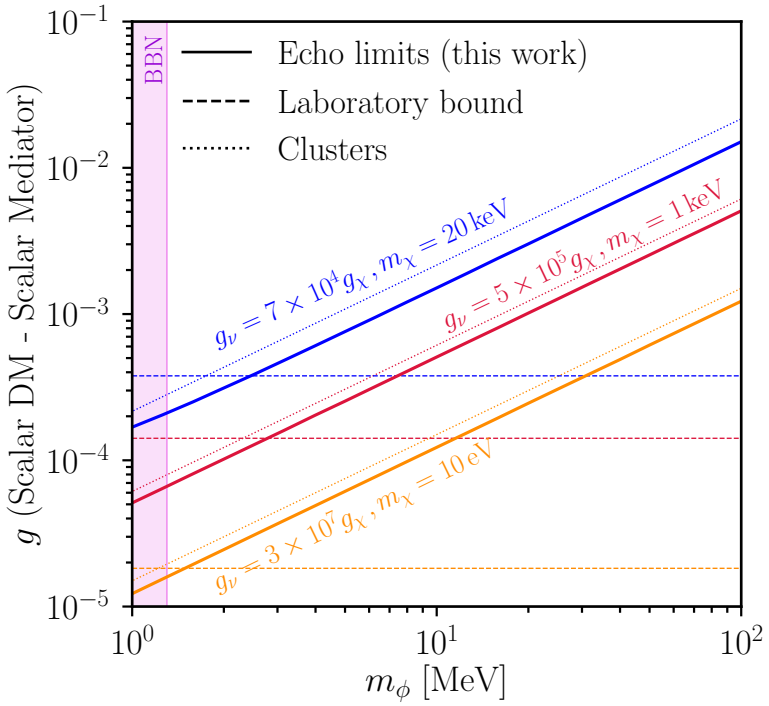

Figure 8.4. Neutrino-DM coupling constraints on $g = (g_\nu g_\chi)^{1/2}$ for scalar DM and scalar mediator. Here, we present the constraints for three DM masses. BBN constraints [22, 28] correspond to the shaded region (magenta). The cluster lines (dotted) show the limits for different ratios of g_ν and g_χ. The laboratory bounds with the same ratios used in each cluster line are shown as dotted lines. The energy scale is $\Lambda = 100$ GeV.

all three models considered, we see that there is a region of parameter space that is not constrained by BBN or laboratory measurements that can be probed by the echo approach.

The time window ΔT used to constrain g is shown in Fig. 8.5 for fermionic DM with a vector mediator. We find that for $\mathcal{O}(10$ keV) mediators, we need time delays between a few weeks and a month. We see that ΔT goes up to a year for mediators heavier than 100 keV, and remains constant for a fixed m_χ, for which the angular distribution becomes less dependent on m_V. The typical scattering angle is sensitive to m_χ, and heavier DM monotonically increases the time window ΔT to achieve a given β, for a fixed mediator mass. For DM above 100 keV, however, a local maximum can be reached and then ΔT decreases. The reason behind this is that ΔT is determined by the delayed neutrino signal, which incorporates a neutrino energy threshold of 14 MeV. As m_χ increases, the scattering angle increases and a larger number of neutrinos are scattered to energies below the threshold. Neutrinos below the energy threshold are not considered part of

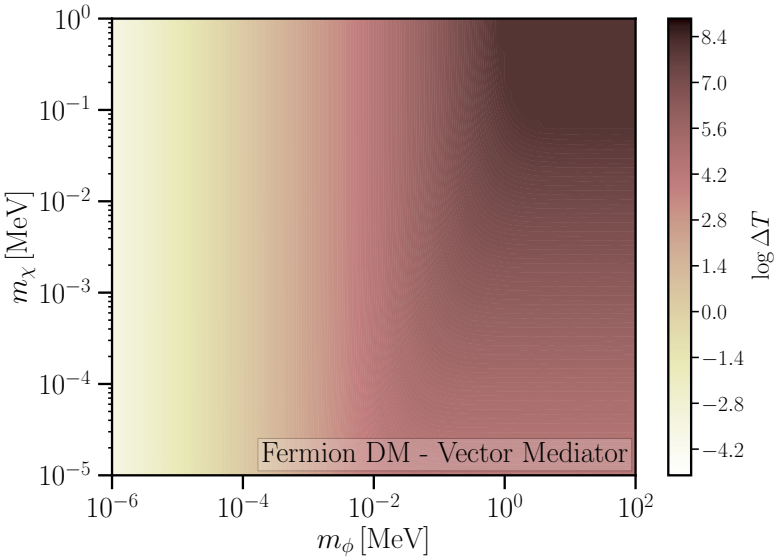

Figure 8.5. Time window ΔT as a function of the mediator mass and DM mass, for 50% of the delayed neutrino signal to reach Earth in the event of a SN at a distance of 10 kpc. We show the case for fermion DM and a vector mediator.

the delay distribution used to determine ΔT, and the removal of these events with large delays causes ΔT to decrease. This effect is clearly visible in the case of fermionic DM with a scalar mediator (see Fig. 8.2), where the time delay distributions tend to have a large peak close to 10^8 s for $m_\chi > 100$ keV, even for light scalar masses.

To get a better view of the comparison between signal and background events, we present in Fig. 8.6 the cumulative number of signal events for 10 keV DM and a 10 MeV mediator. This choice of these parameters corresponds to the region with longer time delays, where delays get closer to 10^8 s. Each model is normalized to the number of events required by the Feldman-Cousins upper limit. Similar to Fig. 8.1, the vector mediator has several neutrino events early on, as the forward scattering is predominant. Even though the signal to background ratio is quite small, the upper limit μ_s grows roughly with $\sqrt{\mu_b}$, so fewer signal events are needed.

We note that the constraints shown were obtained for a SN with total neutrino energy of 3×10^{53} erg at $D = 10$ kpc. Our approach relies on determining μ_s, which depends only on the chosen time window (i.e. on m_χ and m_V. Once m_χ and m_V are fixed, $N_{\rm scatt} \propto g_\nu^2 g_\chi^2 \mathcal{E}_\nu / D$, so we can get constraints for other SNe by the appropriate scaling. Thus, choosing different SNe models, namely changing α and $\langle E_\nu \rangle$, mildly affects the constraints, as long as the majority of the SN neutrinos is above the neutrino energy threshold for Hyper-Kamiokande.

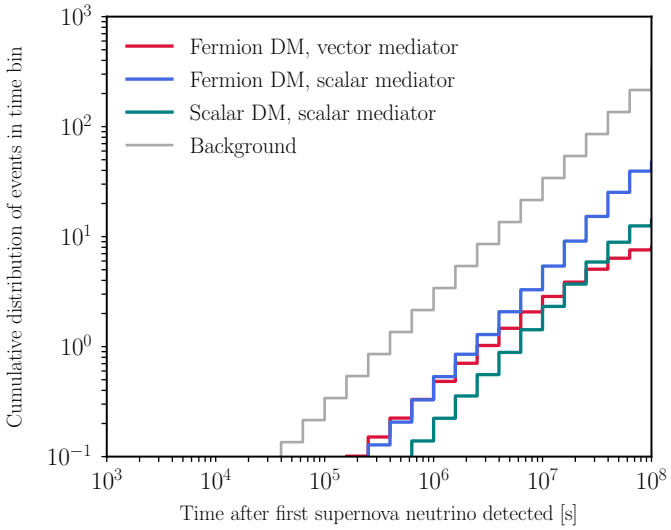

Figure 8.6. Cumulative number of delayed signal events in Hyper-Kamiokande, compared to the background, which has a rate of 3.41×10^{-6} Hz. Here, we show the three different models used for $m_\chi = 10\,\text{keV}, m_\text{V} = 10\,\text{MeV}, m_\phi = 10\,\text{MeV}$. Each distribution has a total number of events corresponding to the time windows used for our upper limits. In the case of the vector mediator, this corresponds to 10 events and $\Delta T = 1.7 \times 10^6$ s; for the scalar mediator with scalar (fermionic) DM, this is 17 (58) events and $\Delta T = 3.9 \times 10^6$ s (5.1×10^6 s).

8.3 Discussion

The presence of DM-neutrino interaction may affect the effective number of relativistic species, N_eff, which provides additional constraints. If DM particles are in equilibrium with the SM bath prior to the neutrino-photon decoupling, the dark matter mass is constrained to be $m_\chi > 1$ MeV [22]. However, it was shown that if the equilibrium between DM and the SM neutrinos occurs after the neutrino-photon decoupling, then N_eff constraints on the interactions can be significantly relaxed [264], allowing for sub-MeV DM.

We also point out that, contrary to the assumption in [22], the parameter space for the models presented also covers the region where DM is lighter than the mediator, in which case DM freeze-out through $\chi - \chi$ annihilation to two mediators is kinematically forbidden. Also, as we provide bounds on the effective coupling g, g_χ could be a lower value to be compliant with other constraints by increasing g_ν or vice versa. Note that, due to this interplay between both couplings, it is possible for our constraints to provide competitive or stronger bounds than clusters constraints.

If we relax the assumption of a homogenous DM density, we would need to perform

a column integral of $n_\chi \sigma_{\nu\chi}$ to get the optical depth. In this scenario, the neutrino is more likely to interact in the regions with the largest DM density. In particular, if the source is located such that the signal has to cross the Galactic Center, the optical depth would increase by a factor of ~ 20 compared to the assumption of constant DM density [265]. Since our number of scattered events is proportional to τ, we would expect our constraints on the coupling to be stronger by a factor $\sim 20^{1/4} \approx 2$. When $m_\phi > 1$ MeV and $m_\chi >$100 keV and the delays become larger than 10^8 s, the increased optical depth may not give a stronger constraint. The time delay also depends on where the scattering takes place. If a very dense DM region is located close to the source such that the scattering is likely to occur far away from Earth, the typical time delay will be longer. For heavier DM, longer delays would force us to adopt $\Delta T = 10^8$ s and would begin to lose signal events to this time cut, which in turn can weaken our constraints.

For the specific case of SN 1987A, neutrino-DM interaction constraints are discussed in Ref. [95]. For MeV DM, it was found that for a constant scattering cross section, cosmological data provide stronger bounds than SN1987A data. As the total number of neutrinos detected from this SN is relatively small, the bounds are obtained from the assumption that there was no significant neutrino absorption in the observed spectrum. Compared to the bound on the cross section $\sigma_{\nu\chi}/m_\chi < 10^{-25}$ cm^2 MeV^{-1} from SN1987A, our projected bound with HK is $\sigma_{\nu\chi}/m_\chi < 1.2 \times 10^{-27}$ cm^2 MeV^{-1} for fermionic DM and a scalar mediator case, with $m_\chi = 1$ keV and $m_\phi = 10$ MeV. For this projected bound we assumed a neutrino energy $E_\nu = 15$ MeV, but within 10 MeV and 25 MeV of neutrino energy, the cross section does not vary significantly for the chosen m_χ and m_ϕ. Also, for this choice of masses our forecasted bound is stronger than the cluster and laboratory constraints. In our case, the expected number of neutrino events in Hyper-Kamiokande in the detector is significantly larger, which allows us to reach unexplored parameter space with the echo method.

8.4 Conclusions

We have shown that in the event of the next Galactic SN, we can constrain neutrino-DM coupling by looking for the delayed neutrino signal from MeV neutrinos echoing off the local DM in the Galaxy. Depending on the model parameters, the signal can be spread out over a duration of $\mathcal{O}(10^8)$ s. For fermionic DM-neutrino interaction via a vector mediator, we can constrain the effective mediator coupling to $g \lesssim 1$ for $\sim 10 - 100$ keV DM and $\mathcal{O}(10)$ MeV mediators. In this model, the bounds from our work are more stringent

than those from cluster constraints for $m_\chi < 20$ keV. We lose the ability to constrain mediators masses, $m_V \lesssim 100$ eV, where most of the delayed signal is contained in a time window shorter than the duration of the neutrino burst. For fermionic DM and a scalar mediator, constraints for $m_\chi \lesssim 1$ keV are stronger than other bounds for m_ϕ between 1 and 20 MeV. Above this DM mass, cluster constraints are stronger for g_ν/g_χ ratios consistent with $g_\nu < 0.1$. For scalar DM and a scalar mediator, constraints can be better than cluster constraints for $\sim 10 - 100$ keV DM and $\mathcal{O}(10)$ MeV mediators, provided that we adjust the g_ν/g_χ ratio accordingly. In this model, however, the laboratory bound on g_ν becomes much stronger for the large $g_\nu/g_\chi \gtrsim 10^5 - 10^7$ ratios used, such that only $m_\phi \lesssim 2$ MeV can be explored for DM masses below 20 keV.

This study has presented a novel approach to probe DM-neutrino interaction with MeV neutrinos from SNe. The neutrino echo method may access the parameter space that have not been explored by DM direct detection searches due to their energy threshold or cosmology. Next-generation neutrino detectors such as Hyper-Kamiokande and DUNE as well as JUNO would be able to explore the keV-MeV DM region due to the large number of expected SN neutrino interactions in these detectors.

Chapter 9
Summary and Conclusions

In this dissertation we outlined the importance of neutrino physics to understand sources of UHECR and gamma-rays. We first provided a theoretical background to explain the basics of neutrino production in astrophysical environments, covered in chapters 2 and 3. We then looked at ways to use neutrinos in the context of IceCube and future detectors to look at source parameters in GRBs and magnetars. We then explored BSM neutrino interactions by using high-energy neutrino sources. Through multimessenger astrophysics, we looked at the potential of neutrino echoes to probe this kind of interactions. We summarize below the results from the published works that form this dissertation.

In chapter 4, we studied the production of high-energy neutrinos in stellar and merger ejecta. Considering particle acceleration at the collimation shock, neutrinos can be injected to energies above 100 TeV. As neutrinos propagate through the stellar progenitor, neutrino oscillations with matter effects can impact the observed flavor ratios on Earth. In particular, we saw that in the 10 TeV – 100 TeV energy range we get significant differences in the flavor ratio, compared to the case where only vacuum oscillations are applied. We looked at low-power choked jet GRB contributions to the diffuse neutrino flux, finding that some jet parameters can explain the 100 TeV scenario, using either strong neutrino attenuation from the progenitor or strong muon cooling via electromagnetic interactions.

Chapter 5 focused on the charmed hadron contributions to the neutrino spectrum in newborn magnetars. We found that most charmed particles are produced within the first few hours after spindown initiates, when protons are injected at very high energies and pions and kaons are too long lived to decay before cooling due to scatterings with ambient nucleons. This signal from charmed hadrons appears above EeV energies. For a source at ~ 3.5 Mpc, the neutrino flux can be detected in IceCube-Gen2, GRAND and POEMMA. The parameter choices for these sources can be consistent with the IceCube diffuse flux limits by tuning the local rate density of magnetar sources.

In chapter 6 we presented the neutrino BSM interaction models used in this work. This included neutrino self-interactions with a scalar mediator, as well as neutrino-DM scattering via a scalar and vector mediator. We discussed the cross sections and angular distributions associated with these processes.

We then showed the geometrical setup for neutrino echoes induced by neutrino self-interactions in chapter 7. Our Monte Carlo simulation proved that analytical estimates in the optically thick regime are insufficient to describe the typical neutrino delay. The difference is dependent on the assumed angular distribution, which in turn depends on the assumed particle physics model. In the case of an ε_ν^{-2} spectrum and a 10 MeV scalar mediator, neutrinos in the 100 TeV region are delayed by 10s – 1000s, depending on the coupling strength. The neutrino flavor composition was found to be largely unaffected by the presence of self-interactions.

As an application of the Monte Carlo code developed in chapter 7, we looked at neutrino-DM scattering with supernova neutrinos. Chapter 8 looks at the use of time-delay distributions to obtain time windows that encompass half of the delayed neutrino signal. If the signal does not produce excess neutrinos with respect to the expected background, then we can derive bounds on the neutrino-DM coupling strength. In our case, we are only sensitive to DM lighter than $\sim$ 1 MeV, as heavier DM would result in time delays longer than 1 year. The parameter space that can be probed with this approach can be more stringent than the ones derived from the BBN and cluster measurements.

Within the next decade, multiple next-generation neutrinos detectors will go online, such as IceCube-Gen2 and KM3NeT. The increased sensitivity to the diffuse neutrino flux will allow for even stronger statistics. Some experiments are aimed at looking for neutrinos above the PeV range, into EeV energies and beyond. These detectors include Trinity, GRAND and RNO-G. The neutrino flux at $\sim$ 1 EeV is not fully known, but we have an idea of this cosmic neutrino flux from cosmic ray observations. Observation of these neutrinos opens the window to neutrino physics at energy scales previously unexplored.

One of the exciting opportunities with IceCube-Gen2 is to look further into the most energetic neutrino sources. Currently, the measured flux above 1 PeV mostly consists of upper limits. Measuring the flux in this region provides a great opportunity to test the choked jet GRB scenarios discussed in chapter 4. On the other hand, the improved point source sensitivities in new detectors can be used to look for charmed hadron production, whose neutrino emission can be observed at the early times of the prompt phase.

Appendix
Charm production and decay into neutrinos

In this Appendix, we include some of the details of our evaluation of charm production. The spectrum of neutrinos from charm hadron decays begins with the energy distribution of these hadrons in pp collisions, $d\sigma/dx_E$ to evaluate $F_{pp\to h}$ in Eq. (3.3). The charm quark distribution is evaluated in NLO QCD collinear approach [224–226], and with the k_T factorization formalism [227–230].

In the latter case, calculation was based on the approach developed in [223, 266] and two scenarios were considered for the evolution of the unintegrated parton density, the linear case as well as the non-linear case which includes corrections due to the large parton density [267]. The unintegrated densities from [268] were used, which were fitted to the inclusive HERA data. The charm quark distribution is then fragmented using fragmentation functions D_c^h. In Eq. (5.10), the fragmentation function D_c^h used is that of Kniehl and Kramer [30],

$$D_c^h(z) = \frac{Nz(1-z)^2}{[(1-z)^2+\epsilon z]^2}\,, \tag{I.1}$$

with the fit parameters given in Table I.1. This parametrization of the fragmentation functions is also used in the evaluation of the prompt atmospheric neutrino flux from charm in Ref. [222, 223]. The constant N for each hadron H includes the fragmentation fractions f_H for each particle [31]: $f_{D^0} = 0.606$, $f_{D^+} = 0.244$, $f_{D_s^+} = 0.081$ and $f_{\Lambda_c^+} = 0.061$.

As a representative case, in Fig. I.1 the distribution $x_E d\sigma/dx_E$ for $x_E = E_{D^0}/E_p$ for three QCD approaches: linear and non-linear k_T factorization and NLO QCD collinear calculation for protons with energy $E_p = 10^{11}$ GeV incident on a fixed proton target. Also shown are the SIBYLL 2.3c x_E distributions for the D^0. The blue band shows a factor

Particle	N	ϵ
D^0	0.577	0.101
D^+	0.238	0.104
D_s^+	0.0327	0.0322
Λ_c^+	0.0067	0.00418

Table I.1. Parameters for the charm quark fragmentation function [30]. The factor N is scaled to reproduce the fragmentation fractions of Ref. [31].

of $1/3 - 3$ of the NLO QCD collinear result, representative of the range of theoretical uncertainties in the prediction for charm meson production. The band includes the predictions from the other three approaches, except at very large x_E. There, the predictions differ more, and the small parton-x extrapolation of the parton distribution functions in the collinear parton model show an effect. This very large x_E region does not make a significant contribution to the neutrino fluence. The blue uncertainty band in Fig. I.1 is translated to neutrino fluence calculations from charm production and decay.

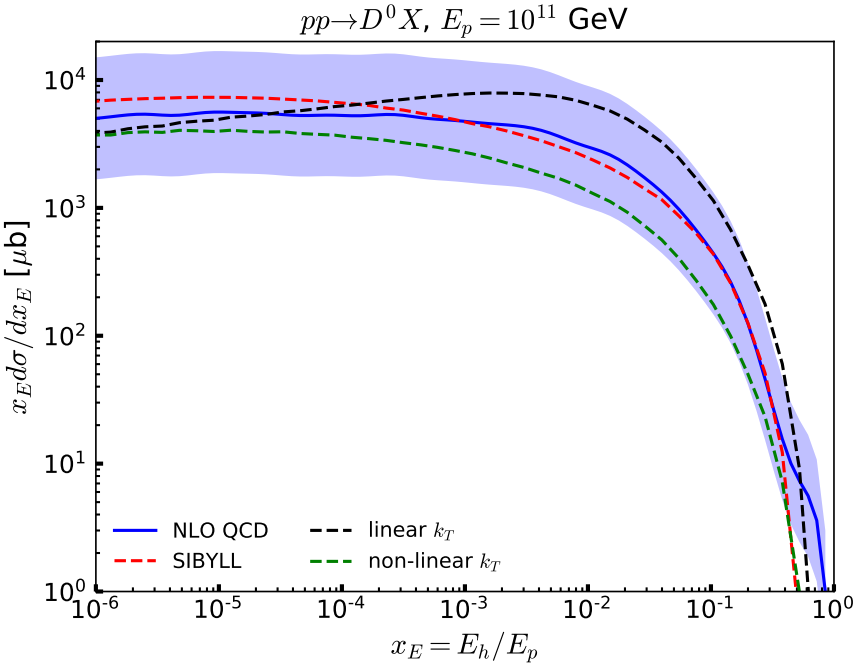

Figure I.1. As a function of $x_E = E_{D^0}/E_p$, the differential distribution of D^0 mesons produced in collisions of protons with E_p incident of fixed target protons for $E_p = 10^{11}$ GeV. The four curves show the evaluation using NLO QCD, the linear and non-linear k_T formulations and the SIBYLL result. The blue band spans a factor of $1/3 - 3$ times the NLO QCD result.

The charmed hadrons mentioned have semileptonic decay channels which include

neutrinos. The semileptonic decay distributions as a function of neutrino energy are approximated by three-body decay formulas [223, 269] with effective final state hadronic mass [32], derived from the pseudoscalar three-body semileptonic decay to a lighter pseudoscalar meson, such as $D \to Kl\nu_l$. Neglecting lepton masses, the distribution is of the form $F_{h\to\nu}(E_\nu, E_h) = \tilde{F}_{h\to\nu}(y)/E_h$ where $y = E_\nu/E_h$, with

$$\begin{aligned}\tilde{F}_{h\to\nu_l}(y) &= \frac{1}{D(\lambda_h)}\Big[6(1-2\lambda_h)(1-\lambda_h)^2 - 4(1-\lambda_h)^3 \\ &\quad -12\lambda_h^3(1-\lambda_h) + 12\lambda_h^2 y - 6(1-2\lambda_h)y^2 \\ &\quad +4y^3 + 12\lambda_h^2 \ln((1-y)/\lambda_h)\Big], \end{aligned} \tag{I.2}$$

and

$$D(\lambda_h) = 1 - 8\lambda_h - 12\lambda_h^2 \ln\lambda_h + 8\lambda_h^3 - \lambda_h^4. \tag{I.3}$$

The parameter $\lambda_h = s_h^{\rm eff}/m_h^2$ is defined in terms of an effective mass $\sqrt{s_h^{\rm eff}}$, shown for charm hadron decays in Table I.2. The kinematic limits on y are $0 < y < 1 - \lambda_h$.

Decay	$\sqrt{s_h^{\rm eff}}$ [GeV]
$D^0 \to \nu_l$	0.67
$D^+ \to \nu_l$	0.63
$D_s^+ \to \nu_l$	0.84
$\Lambda_c^+ \to \nu_l$	1.3

Table I.2. Effective masses $\sqrt{s_h^{\rm eff}}$ used to calculate the neutrino spectrum from charmed hadron decay [32].

Bibliography

[1] Aartsen, M. G. et al. (2020) "Characteristics of the diffuse astrophysical electron and tau neutrino flux with six years of IceCube high energy cascade data," *Phys. Rev. Lett.*, **125**(12), p. 121104, 2001.09520.

[2] Janka, H.-T., F. Hanke, L. Hüdepohl, A. Marek, B. Müller, and M. Obergaulinger (2012) "Core-collapse supernovae: Reflections and directions," *Progress of Theoretical and Experimental Physics*, **2012**(1), 01A309, https://academic.oup.com/ptep/article-pdf/2012/1/01A309/16825337/pts067.pdf. URL https://doi.org/10.1093/ptep/pts067

[3] Morejon, L., A. Fedynitch, D. Boncioli, D. Biehl, and W. Winter (2019) "Improved photomeson model for interactions of cosmic ray nuclei," *JCAP*, **11**, p. 007, 1904.07999.

[4] Ahlers, M., K. Helbing, and C. Pérez de los Heros (2018) "Probing Particle Physics with IceCube," *Eur. Phys. J. C*, **78**(11), p. 924, 1806.05696.

[5] Abbasi, R. et al. (2022) "Improved Characterization of the Astrophysical Muon–neutrino Flux with 9.5 Years of IceCube Data," *Astrophys. J.*, **928**(1), p. 50, 2111.10299.

[6] ——— (2021) "The IceCube high-energy starting event sample: Description and flux characterization with 7.5 years of data," *Phys. Rev. D*, **104**, p. 022002, 2011.03545.

[7] Aartsen, M. G. et al. (2019) "Measurements using the inelasticity distribution of multi-TeV neutrino interactions in IceCube," *Phys. Rev. D*, **99**(3), p. 032004, 1808.07629.

[8] Fusco, L. A. and F. Versari (2020) "Study of the high-energy neutrino diffuse flux with the ANTARES neutrino telescope," *PoS*, **ICRC2019**, p. 891.

[9] Ackermann, M. et al. (2022) "High-energy and ultra-high-energy neutrinos: A Snowmass white paper," *JHEAp*, **36**, pp. 55–110, 2203.08096.

[10] Abbasi, R. et al. (2020) "Measurement of the high-energy all-flavor neutrino-nucleon cross section with IceCube," 2011.03560.

[11] Mizuta, A. and K. Ioka (2013) "Opening Angles of Collapsar Jets," *Astrophys. J.*, **777**, p. 162, 1304.0163.

[12] Woosley, S. E., A. Heger, and T. A. Weaver (2002) "The evolution and explosion of massive stars," *Rev. Mod. Phys.*, **74**, pp. 1015–1071.
URL https://link.aps.org/doi/10.1103/RevModPhys.74.1015

[13] Kopper, C. (2017) "Observation of Astrophysical Neutrinos in Six Years of IceCube Data," *PoS*, **ICRC2017**, p. 981.

[14] Murase, K. and K. Ioka (2013) "TeV–PeV Neutrinos from Low-Power Gamma-Ray Burst Jets inside Stars," *Phys. Rev. Lett.*, **111**(12), p. 121102, 1306.2274.

[15] Aartsen, M. G. et al. (2019) "Neutrino astronomy with the next generation IceCube Neutrino Observatory," 1911.02561.

[16] Venters, T. M., M. H. Reno, J. F. Krizmanic, L. A. Anchordoqui, C. Guépin, and A. V. Olinto (2020) "POEMMA's Target of Opportunity Sensitivity to Cosmic Neutrino Transient Sources," *Phys. Rev. D*, **102**, p. 123013, 1906.07209.

[17] Álvarez Muñiz, J. et al. (2020) "The Giant Radio Array for Neutrino Detection (GRAND): Science and Design," *Sci. China Phys. Mech. Astron.*, **63**(1), p. 219501, 1810.09994.

[18] Haensel, P., J. P. Lasota, and J. L. Zdunik (1999) "On the minimum period of uniformly rotating meutron stars," astro-ph/9901118.

[19] Kopper, C. (2018) "Observation of Astrophysical Neutrinos in Six Years of IceCube Data," *PoS*, **ICRC2017**, p. 981.

[20] Aartsen, M. G. et al. (2018) "Differential limit on the extremely-high-energy cosmic neutrino flux in the presence of astrophysical background from nine years of IceCube data," *Phys. Rev. D*, **98**(6), p. 062003, 1807.01820.

[21] Archidiacono, M. and S. Hannestad (2014) "Updated constraints on non-standard neutrino interactions from Planck," *JCAP*, **07**, p. 046, 1311.3873.

[22] Blinov, N., K. J. Kelly, G. Z. Krnjaic, and S. D. McDermott (2019) "Constraining the Self-Interacting Neutrino Interpretation of the Hubble Tension," *Phys. Rev. Lett.*, **123**(19), p. 191102, 1905.02727.

[23] Berryman, J. M., A. De Gouvêa, K. J. Kelly, and Y. Zhang (2018) "Lepton-Number-Charged Scalars and Neutrino Beamstrahlung," *Phys. Rev. D*, **97**(7), p. 075030, 1802.00009.

[24] Kolb, E. W. and M. S. Turner (1987) "Supernova 1987A and the secret interactions of neutrinos," *Phys. Rev. D*, **36**, pp. 2895–2900.
URL https://link.aps.org/doi/10.1103/PhysRevD.36.2895

[25] Shalgar, S., I. Tamborra, and M. Bustamante (2021) "Core-collapse supernovae stymie secret neutrino interactions," *Phys. Rev. D*, **103**(12), p. 123008, 1912.09115.

[26] Kelly, K. J. and P. A. N. Machado (2018) "Multimessenger Astronomy and New Neutrino Physics," *JCAP*, **10**, p. 048, 1808.02889.

[27] Bustamante, M., C. Rosenstrøm, S. Shalgar, and I. Tamborra (2020) "Bounds on secret neutrino interactions from high-energy astrophysical neutrinos," *Phys. Rev. D*, **101**(12), p. 123024, 2001.04994.

[28] Escudero, M., D. Hooper, G. Krnjaic, and M. Pierre (2019) "Cosmology with A Very Light $L_\mu - L_\tau$ Gauge Boson," *JHEP*, **03**, p. 071, 1901.02010.

[29] Esteban, I., M. C. Gonzalez-Garcia, M. Maltoni, T. Schwetz, and A. Zhou (2020) "The fate of hints: updated global analysis of three-flavor neutrino oscillations," *JHEP*, **09**, p. 178, 2007.14792.

[30] Kniehl, B. A. and G. Kramer (2006) "Charmed-hadron fragmentation functions from CERN LEP1 revisited," *Phys. Rev. D*, **74**, p. 037502, hep-ph/0607306.

[31] Lisovyi, M., A. Verbytskyi, and O. Zenaiev (2016) "Combined analysis of charm-quark fragmentation-fraction measurements," *Eur. Phys. J.*, **C76**(7), p. 397, 1509.01061.

[32] Bugaev, E. V., A. Misaki, V. A. Naumov, T. S. Sinegovskaya, S. I. Sinegovsky, and N. Takahashi (1998) "Atmospheric muon flux at sea level, underground and underwater," *Phys. Rev.*, **D58**, p. 054001, hep-ph/9803488.

[33] Gell-Mann, M. and A. Pais (1955) "Behavior of Neutral Particles under Charge Conjugation," *Phys. Rev.*, **97**, pp. 1387–1389.
URL https://link.aps.org/doi/10.1103/PhysRev.97.1387

[34] Pontecorvo, B. (1967) "Neutrino Experiments and the Problem of Conservation of Leptonic Charge," *Zh. Eksp. Teor. Fiz.*, **53**, pp. 1717–1725.

[35] Fukuda, Y. et al. (1998) "Evidence for Oscillation of Atmospheric Neutrinos," *Phys. Rev. Lett.*, **81**, pp. 1562–1567.
URL https://link.aps.org/doi/10.1103/PhysRevLett.81.1562

[36] Ahmad, Q. R. et al. (2001) "Measurement of the rate of $\nu_e + d \to p + p + e^-$ interactions produced by ^{8}B solar neutrinos at the Sudbury Neutrino Observatory," *Phys. Rev. Lett.*, **87**, p. 071301, nucl-ex/0106015.

[37] Acciarri, R. et al. (2016) "Long-Baseline Neutrino Facility (LBNF) and Deep Underground Neutrino Experiment (DUNE): Conceptual Design Report, Volume 1: The LBNF and DUNE Projects," 1601.05471.

[38] Hirata, K. et al. (1987) "Observation of a Neutrino Burst from the Supernova SN 1987a," *Phys. Rev. Lett.*, **58**, pp. 1490–1493.

[39] Bionta, R. M., G. Blewitt, C. B. Bratton, D. Casper, A. Ciocio, R. Claus, B. Cortez, M. Crouch, S. T. Dye, S. Errede, G. W. Foster, W. Gajewski, K. S. Ganezer, M. Goldhaber, T. J. Haines, T. W. Jones, D. Kielczewska, W. R. Kropp, J. G. Learned, J. M. LoSecco, J. Matthews, R. Miller, M. S. Mudan, H. S. Park, L. R. Price, F. Reines, J. Schultz, S. Seidel, E. Shumard, D. Sinclair, H. W. Sobel, J. L. Stone, L. R. Sulak, R. Svoboda, G. Thornton, J. C. van der Velde, and C. Wuest (1987) "Observation of a neutrino burst in coincidence with supernova 1987A in the Large Magellanic Cloud," *Phys. Rev. Lett.*, **58**, pp. 1494–1496. URL https://link.aps.org/doi/10.1103/PhysRevLett.58.1494

[40] Aartsen, M. G. et al. (2013) "Evidence for High-Energy Extraterrestrial Neutrinos at the IceCube Detector," *Science*, **342**, p. 1242856, 1311.5238.

[41] ——— (2015) "Search for Astrophysical Tau Neutrinos in Three Years of IceCube Data," 1509.06212.

[42] Abbasi, R. et al. (2022) "Detection of astrophysical tau neutrino candidates in IceCube," *Eur. Phys. J. C*, **82**(11), p. 1031, 2011.03561.

[43] Aartsen, M. G. et al. (2021) "Detection of a particle shower at the Glashow resonance with IceCube," *Nature*, **591**(7849), pp. 220–224, [Erratum: Nature 592, E11 (2021)], 2110.15051.

[44] ——— (2018) "Multimessenger observations of a flaring blazar coincident with high-energy neutrino IceCube-170922A," *Science*, **361**(6398), p. eaat1378, 1807.08816.

[45] Keivani, A. et al. (2018) "A Multimessenger Picture of the Flaring Blazar TXS 0506+056: implications for High-Energy Neutrino Emission and Cosmic Ray Acceleration," *Astrophys. J.*, **864**(1), p. 84, 1807.04537.

[46] Aartsen, M. G. et al. (2020) "Time-Integrated Neutrino Source Searches with 10 Years of IceCube Data," *Phys. Rev. Lett.*, **124**(5), p. 051103, 1910.08488.

[47] Abbasi, R. et al. (2022) "Evidence for neutrino emission from the nearby active galaxy NGC 1068," *Science*, **378**(6619), pp. 538–543, 2211.09972.

[48] Murase, K. (2022) "Hidden Hearts of Neutrino Active Galaxies," *Astrophys. J. Lett.*, **941**(1), p. L17, 2211.04460.

[49] Adhikari, G. et al. (2022) "nEXO: neutrinoless double beta decay search beyond 10^{28} year half-life sensitivity," *J. Phys. G*, **49**(1), p. 015104, 2106.16243.

[50] Aguilar-Arevalo, A. et al. (2001) "Evidence for neutrino oscillations from the observation of $\bar{\nu}_e$ appearance in a $\bar{\nu}_\mu$ beam," *Phys. Rev. D*, **64**, p. 112007, hep-ex/0104049.

[51] Aguilar-Arevalo, A. A. et al. (2018) "Significant Excess of ElectronLike Events in the MiniBooNE Short-Baseline Neutrino Experiment," *Phys. Rev. Lett.*, **121**(22), p. 221801, 1805.12028.

[52] Asaadi, J., E. Church, R. Guenette, B. J. P. Jones, and A. M. Szelc (2018) "New light Higgs boson and short-baseline neutrino anomalies," *Phys. Rev. D*, **97**(7), p. 075021, 1712.08019.

[53] Dentler, M., I. Esteban, J. Kopp, and P. Machado (2020) "Decaying Sterile Neutrinos and the Short Baseline Oscillation Anomalies," *Phys. Rev. D*, **101**(11), p. 115013, 1911.01427.

[54] de Gouvêa, A., O. L. G. Peres, S. Prakash, and G. V. Stenico (2020) "On The Decaying-Sterile Neutrino Solution to the Electron (Anti)Neutrino Appearance Anomalies," *JHEP*, **07**, p. 141, 1911.01447.

[55] Araki, T., F. Kaneko, T. Ota, J. Sato, and T. Shimomura (2016) "MeV scale leptonic force for cosmic neutrino spectrum and muon anomalous magnetic moment," *Phys. Rev. D*, **93**(1), p. 013014, 1508.07471.

[56] He, X. G., G. C. Joshi, H. Lew, and R. R. Volkas (1991) "NEW Z-prime PHENOMENOLOGY," *Phys. Rev. D*, **43**, pp. 22–24.

[57] He, X.-G., G. C. Joshi, H. Lew, and R. R. Volkas (1991) "Simplest Z-prime model," *Phys. Rev. D*, **44**, pp. 2118–2132.

[58] Ma, E., D. P. Roy, and S. Roy (2002) "Gauged L(mu) - L(tau) with large muon anomalous magnetic moment and the bimaximal mixing of neutrinos," *Phys. Lett. B*, **525**, pp. 101–106, hep-ph/0110146.

[59] Heeck, J. and W. Rodejohann (2011) "Gauged $L_\mu - L_\tau$ Symmetry at the Electroweak Scale," *Phys. Rev. D*, **84**, p. 075007, 1107.5238.

[60] Forastieri, F., M. Lattanzi, and P. Natoli (2015) "Constraints on secret neutrino interactions after Planck," *JCAP*, **07**, p. 014, 1504.04999.

[61] ——— (2019) "Cosmological constraints on neutrino self-interactions with a light mediator," *Phys. Rev. D*, **100**(10), p. 103526, 1904.07810.

[62] Roy Choudhury, S., S. Hannestad, and T. Tram (2021) "Updated constraints on massive neutrino self-interactions from cosmology in light of the H_0 tension," *JCAP*, **03**, p. 084, 2012.07519.

[63] Blum, K., A. Hook, and K. Murase (2014) "High energy neutrino telescopes as a probe of the neutrino mass mechanism," 1408.3799.

[64] Ng, K. C. Y. and J. F. Beacom (2014) "Cosmic neutrino cascades from secret neutrino interactions," *Phys. Rev.*, **D90**(6), p. 065035, [Erratum: Phys. Rev.D90,no.8,089904(2014)], 1404.2288.

[65] Ioka, K. and K. Murase (2014) "IceCube PeV–EeV neutrinos and secret interactions of neutrinos," *PTEP*, **2014**(6), p. 061E01, 1404.2279.

[66] Esteban, I., S. Pandey, V. Brdar, and J. F. Beacom (2021) "Probing secret interactions of astrophysical neutrinos in the high-statistics era," *Phys. Rev. D*, **104**(12), p. 123014, 2107.13568.

[67] Carpio, J. A., K. Murase, I. M. Shoemaker, and Z. Tabrizi (2023) "High-energy cosmic neutrinos as a probe of the vector mediator scenario in light of the muon g-2 anomaly and Hubble tension," *Phys. Rev. D*, **107**(10), p. 103057, 2104.15136.

[68] Rubin, V. C., D. Burstein, W. K. Ford, Jr., and N. Thonnard (1985) "Rotation velocities of 16 SA galaxies and a comparison of Sa, Sb, and SC rotation properties," *Astrophys. J.*, **289**, p. 81.

[69] Begeman, K. G., A. H. Broeils, and R. H. Sanders (1991) "Extended rotation curves of spiral galaxies: Dark haloes and modified dynamics," *Mon. Not. Roy. Astron. Soc.*, **249**, p. 523.

[70] Bergmann, A. G., V. Petrosian, and R. Lynds (1990) "Gravitational Lens Models of Arcs in Clusters," *Astrophys. J.*, **350**, p. 23.

[71] Clowe, D., M. Bradac, A. H. Gonzalez, M. Markevitch, S. W. Randall, C. Jones, and D. Zaritsky (2006) "A direct empirical proof of the existence of dark matter," *Astrophys. J. Lett.*, **648**, pp. L109–L113, astro-ph/0608407.

[72] Jee, M. J. et al. (2007) "Discovery of a Ringlike Dark Matter Structure in the Core of the Galaxy Cluster Cl 0024+17," *Astrophys. J.*, **661**, pp. 728–749, 0705.2171.

[73] Bradac, M., S. W. Allen, T. Treu, H. Ebeling, R. Massey, R. G. Morris, A. von der Linden, and D. Applegate (2008) "Revealing the properties of dark matter in the merging cluster MACSJ0025.4-1222," *Astrophys. J.*, **687**, p. 959, 0806.2320.

[74] Bertone, G., D. Hooper, and J. Silk (2005) "Particle dark matter: Evidence, candidates and constraints," *Phys. Rept.*, **405**, pp. 279–390, hep-ph/0404175.

[75] Feng, J. L. (2010) "Dark Matter Candidates from Particle Physics and Methods of Detection," *Ann. Rev. Astron. Astrophys.*, **48**, pp. 495–545, 1003.0904.

[76] Aprile, E. et al. (2018) "Dark Matter Search Results from a One Ton-Year Exposure of XENON1T," *Phys. Rev. Lett.*, **121**(11), p. 111302, 1805.12562.

[77] Akerib, D. S. et al. (2017) "Results from a search for dark matter in the complete LUX exposure," *Phys. Rev. Lett.*, **118**(2), p. 021303, 1608.07648.

[78] Wang, Q. et al. (2020) "Results of dark matter search using the full PandaX-II exposure," *Chin. Phys. C*, **44**(12), p. 125001, 2007.15469.

[79] Abada, A. and M. Lucente (2014) "Looking for the minimal inverse seesaw realisation," *Nucl. Phys. B*, **885**, pp. 651–678, 1401.1507.

[80] Abada, A., G. Arcadi, and M. Lucente (2014) "Dark Matter in the minimal Inverse Seesaw mechanism," *JCAP*, **10**, p. 001, 1406.6556.

[81] Boulebnane, S., J. Heeck, A. Nguyen, and D. Teresi (2018) "Cold light dark matter in extended seesaw models," *JCAP*, **04**, p. 006, 1709.07283.

[82] Kouvaris, C., I. M. Shoemaker, and K. Tuominen (2015) "Self-Interacting Dark Matter through the Higgs Portal," *Phys. Rev. D*, **91**(4), p. 043519, 1411.3730.

[83] Bernal, N., X. Chu, C. Garcia-Cely, T. Hambye, and B. Zaldivar (2016) "Production Regimes for Self-Interacting Dark Matter," *JCAP*, **03**, p. 018, 1510.08063.

[84] Kainulainen, K., K. Tuominen, and V. Vaskonen (2016) "Self-interacting dark matter and cosmology of a light scalar mediator," *Phys. Rev. D*, **93**(1), p. 015016, [Erratum: Phys.Rev.D 95, 079901 (2017)], 1507.04931.

[85] Hambye, T. and L. Vanderheyden (2020) "Minimal self-interacting dark matter models with light mediator," *JCAP*, **05**, p. 001, 1912.11708.

[86] Cirelli, M., P. Panci, K. Petraki, F. Sala, and M. Taoso (2017) "Dark Matter's secret liaisons: phenomenology of a dark U(1) sector with bound states," *JCAP*, **05**, p. 036, 1612.07295.

[87] Kahlhoefer, F., K. Schmidt-Hoberg, and S. Wild (2017) "Dark matter self-interactions from a general spin-0 mediator," *JCAP*, **08**, p. 003, 1704.02149.

[88] Boylan-Kolchin, M., J. S. Bullock, and M. Kaplinghat (2011) "Too big to fail? The puzzling darkness of massive Milky Way subhaloes," *MNRAS*, **415**(1), pp. L40–L44, 1103.0007.

[89] Klypin, A. A., A. V. Kravtsov, O. Valenzuela, and F. Prada (1999) "Where are the missing Galactic satellites?" *Astrophys.J.*, **522**, pp. 82–92, astro-ph/9901240.

[90] Moore, B., S. Ghigna, F. Governato, G. Lake, T. R. Quinn, J. Stadel, and P. Tozzi (1999) "Dark matter substructure within galactic halos," *Astrophys. J. Lett.*, **524**, pp. L19–L22, astro-ph/9907411.

[91] Boehm, C., P. Fayet, and R. Schaeffer (2001) "Constraining dark matter candidates from structure formation," *Phys. Lett.*, **B518**, pp. 8–14, astro-ph/0012504.

[92] Boehm, C., A. Riazuelo, S. H. Hansen, and R. Schaeffer (2002) "Interacting dark matter disguised as warm dark matter," *Phys.Rev.*, **D66**, p. 083505, astro-ph/0112522.

[93] Boehm, C. and R. Schaeffer (2005) "Constraints on dark matter interactions from structure formation: Damping lengths," *A. & A.*, **438**, pp. 419–442, astro-ph/0410591.

[94] Bertschinger, E. (2006) "The Effects of Cold Dark Matter Decoupling and Pair Annihilation on Cosmological Perturbations," *Phys.Rev.*, **D74**, p. 063509, astro-ph/0607319.

[95] Mangano, G., A. Melchiorri, P. Serra, A. Cooray, and M. Kamionkowski (2006) "Cosmological bounds on dark matter-neutrino interactions," *Phys.Rev.*, **D74**, p. 043517, astro-ph/0606190.

[96] Serra, P., F. Zalamea, A. Cooray, G. Mangano, and A. Melchiorri (2010) "Constraints on neutrino – dark matter interactions from cosmic microwave background and large scale structure data," *Phys.Rev.*, **D81**, p. 043507, 0911.4411.

[97] Wilkinson, R. J., C. Boehm, and J. Lesgourgues (2014) "Constraining Dark Matter-Neutrino Interactions using the CMB and Large-Scale Structure," *JCAP*, **05**, p. 011, 1401.7597.

[98] van den Aarssen, L. G., T. Bringmann, and C. Pfrommer (2012) "Is dark matter with long-range interactions a solution to all small-scale problems of Lambda CDM cosmology?" *Phys. Rev. Lett.*, **109**, p. 231301, 1205.5809.

[99] Farzan, Y. and S. Palomares-Ruiz (2014) "Dips in the Diffuse Supernova Neutrino Background," *JCAP*, **1406**, p. 014, 1401.7019.

[100] Boehm, C., J. A. Schewtschenko, R. J. Wilkinson, C. M. Baugh, and S. Pascoli (2014) "Using the Milky Way satellites to study interactions between cold dark matter and radiation," *Mon. Not. Roy. Astron. Soc.*, **445**, pp. L31–L35, 1404.7012.

[101] Cherry, J. F., A. Friedland, and I. M. Shoemaker (2014) "Neutrino Portal Dark Matter: From Dwarf Galaxies to IceCube," 1411.1071.

[102] Bertoni, B., S. Ipek, D. McKeen, and A. E. Nelson (2015) "Constraints and consequences of reducing small scale structure via large dark matter-neutrino interactions," *JHEP*, **04**, p. 170, 1412.3113.

[103] Schewtschenko, J. A., R. J. Wilkinson, C. M. Baugh, C. Bœhm, and S. Pascoli (2015) "Dark matter–radiation interactions: the impact on dark matter haloes," *Mon. Not. Roy. Astron. Soc.*, **449**(4), pp. 3587–3596, 1412.4905.

[104] Argüelles, C. A., A. Kheirandish, and A. C. Vincent (2017) "Imaging Galactic Dark Matter with High-Energy Cosmic Neutrinos," *Phys. Rev. Lett.*, **119**(20), p. 201801, 1703.00451.

[105] Choi, K.-Y., J. Kim, and C. Rott (2019) "Constraining dark matter-neutrino interactions with IceCube-170922A," *Phys. Rev. D*, **99**(8), p. 083018, 1903.03302.

[106] Murase, K. and I. M. Shoemaker (2019) "Neutrino Echoes from Multimessenger Transient Sources," *Phys. Rev. Lett.*, **123**(24), p. 241102, 1903.08607.

[107] Aartsen, M. G. et al. (2018) "Neutrino emission from the direction of the blazar TXS 0506+056 prior to the IceCube-170922A alert," *Science*, **361**(6398), pp. 147–151, 1807.08794.

[108] Stein, R. et al. (2021) "A tidal disruption event coincident with a high-energy neutrino," *Nature Astron.*, **5**(5), pp. 510–518, 2005.05340.

[109] de Ugarte Postigo, A., L. Izzo, G. Pugliese, D. Xu, B. Schneider, J. P. U. Fynbo, N. R. Tanvir, D. B. Malesani, A. Saccardi, D. A. Kann, K. Wiersema, B. P. Gompertz, C. C. Thoene, A. J. Levan, and Stargate Collaboration (2022) "GRB 221009A: Redshift from X-shooter/VLT," *GRB Coordinates Network*, **32648**, p. 1.

[110] Brdar, V. and Y.-Y. Li (2023) "Neutrino origin of LHAASO's 18 TeV GRB221009A photon," *Phys. Lett. B*, **839**, p. 137763, 2211.02028.

[111] Cheung, K. (2022) "The Role of a Heavy Neutrino in the Gamma-Ray Burst GRB-221009A," 2210.14178.

[112] Smirnov, A. Y. and A. Trautner (2022) "GRB 221009A Gamma Rays from Radiative Decay of Heavy Neutrinos?" 2211.00634.

[113] Abbasi, R. et al. (2023) "Limits on Neutrino Emission from GRB 221009A from MeV to PeV Using the IceCube Neutrino Observatory," *Astrophys. J. Lett.*, **946**(1), p. L26, 2302.05459.

[114] Carpio, J. A. and K. Murase (2020) "Oscillation of high-energy neutrinos from choked jets in stellar and merger ejecta," *Phys. Rev. D*, **101**(12), p. 123002, 2002.10575.

[115] Carpio, J. A., K. Murase, M. H. Reno, I. Sarcevic, and A. Stasto (2020) "Charm contribution to ultrahigh-energy neutrinos from newborn magnetars," *Phys. Rev. D*, **102**(10), p. 103001, 2007.07945.

[116] Carpio, J. A. and K. Murase (2023) "Simulating neutrino echoes induced by secret neutrino interactions," *JCAP*, **02**, p. 042, 2204.09029.

[117] Carpio, J. A., A. Kheirandish, and K. Murase (2023) "Time-delayed neutrino emission from supernovae as a probe of dark matter-neutrino interactions," *JCAP*, **04**, p. 019, 2204.09650.

[118] Zyla, P. et al. (2020) "Review of Particle Physics," *PTEP*, **2020**(8), p. 083C01.

[119] Maki, Z., M. Nakagawa, and S. Sakata (1962) "Remarks on the Unified Model of Elementary Particles," *Progress of Theoretical Physics*, **28**(5), pp. 870–880, https://academic.oup.com/ptp/article-pdf/28/5/870/5258750/28-5-870.pdf.
URL https://doi.org/10.1143/PTP.28.870

[120] Giunti, C. (2004) "Coherence and wave packets in neutrino oscillations," *Found. Phys. Lett.*, **17**, pp. 103–124, hep-ph/0302026.

[121] Wolfenstein, L. (1978) "Neutrino oscillations in matter," *Phys. Rev. D*, **17**(9), pp. 2369–2374.

[122] Mikheyev, S. P. and A. Y. Smirnov (1985) "Resonance enhancement of oscillations in matter and solar neutrino spectroscopy," *Yadernaya Fizika*, **42**, pp. 1441–1448.

[123] Giunti, C. and C. W. Kim (2007) *Fundamentals of Neutrino Physics and Astrophysics*, Oxford University Press.
URL https://doi.org/10.1093/acprof:oso/9780198508717.001.0001

[124] Razzaque, S. and A. Y. Smirnov (2010) "Flavor conversion of cosmic neutrinos from hidden jets," *JHEP*, **03**, p. 031, 0912.4028.

[125] Carroll, S. M. "Lecture notes on general relativity," *arXiv:gr-qc/9712019*, gr-qc/9712019.

[126] Aghanim, N. et al. (2020) "Planck 2018 results. VI. Cosmological parameters," *Astron. Astrophys.*, **641**, p. A6, [Erratum: Astron.Astrophys. 652, C4 (2021)], 1807.06209.

[127] Filippenko, A. V. (1997) "OPTICAL SPECTRA OF SUPERNOVAE," *Annual Review of Astronomy and Astrophysics*, **35**(1), pp. 309–355.
URL https://doi.org/10.1146/annurev.astro.35.1.309

[128] Heger, A., C. L. Fryer, S. E. Woosley, N. Langer, and D. H. Hartmann (2003) "How massive single stars end their life," *Astrophys. J.*, **591**, pp. 288–300, astro-ph/0212469.

[129] Galama, T. J. et al. (1998) "Discovery of the peculiar supernova 1998bw in the error box of GRB 980425," *Nature*, **395**, p. 670, astro-ph/9806175.

[130] Woosley, S. E., R. G. Eastman, and B. P. Schmidt (1999) "Gamma-ray bursts and type Ic supernovae: SN 1998bw," *Astrophys. J.*, **516**, p. 788, astro-ph/9806299.

[131] Kaneko, Y., E. Ramirez-Ruiz, J. Granot, C. Kouveliotou, S. E. Woosley, S. K. Patel, E. Rol, J. J. M. in 't Zand, A. J. van der Horst, R. A. M. J. Wijers, and R. Strom (2007) "Prompt and Afterglow Emission Properties of Gamma-Ray Bursts with Spectroscopically Identified Supernovae," *The Astrophysical Journal*, **654**(1), p. 385.
URL https://dx.doi.org/10.1086/508324

[132] Izzo, L. et al. (2019) "Signatures of a jet cocoon in early spectra of a supernova associated with a γ-ray burst," *Nature*, **565**, p. 324, 1901.05500.

[133] Berger, E., S. R. Kulkarni, D. A. Frail, and A. M. Soderberg (2003) "A Radio Survey of Type Ib and Ic Supernovae: Searching for Engine-driven Supernovae," *The Astrophysical Journal*, **599**(1), p. 408.
URL https://dx.doi.org/10.1086/379214

[134] Guetta, D. and M. D. Valle (2007) "On the Rates of Gamma-Ray Bursts and Type Ib/c Supernovae," *The Astrophysical Journal*, **657**(2), p. L73.
URL https://dx.doi.org/10.1086/511417

[135] Margutti, R., A. M. Soderberg, M. H. Wieringa, P. G. Edwards, R. A. Chevalier, B. J. Morsony, R. Barniol Duran, L. Sironi, B. A. Zauderer, D. Milisavljevic, A. Kamble, and E. Pian (2013) "The Signature of the Central Engine in the Weakest Relativistic Explosions: GRB 100316D," *The Astrophysical Journal*, **778**(1), 18, 1308.1687.

[136] Margutti, R., D. Milisavljevic, A. M. Soderberg, C. Guidorzi, B. J. Morsony, N. Sanders, S. Chakraborti, A. Ray, A. Kamble, M. Drout, J. Parrent, A. Zauderer, and L. Chomiuk (2014) "Relativistic Supernovae have Shorter-lived Central Engines or More Extended Progenitors: The Case of SN 2012ap," *The Astrophysical Journal*, **797**(2), 107, 1402.6344.

[137] Nakar, E. (2015) "A unified picture for low-luminosity and long gamma-ray bursts based on the extended progenitor of llgrb 060218/SN 2006aj," *Astrophys. J.*, **807**(2), p. 172, 1503.00441.

[138] Colgate, S. A. and R. H. White (1966) "The Hydrodynamic Behavior of Supernovae Explosions," *Astrophys. J.*, **143**, p. 626.

[139] Bethe, H. A. and J. R. Wilson (1985) "Revival of a stalled supernova shock by neutrino heating," *Astrophys. J.*, **295**, pp. 14–23.

[140] Keil, M. T., G. G. Raffelt, and H.-T. Janka (2003) "Monte Carlo study of supernova neutrino spectra formation," *Astrophys. J.*, **590**, pp. 971–991, astro-ph/0208035.

[141] Tamborra, I., F. Hanke, H.-T. Janka, B. Müller, G. G. Raffelt, and A. Marek (2014) "Self-sustained asymmetry of lepton-number emission: A new phenomenon during the supernova shock-accretion phase in three dimensions," *Astrophys. J.*, **792**(2), p. 96, 1402.5418.

[142] Radice, D., A. Burrows, D. Vartanyan, M. A. Skinner, and J. C. Dolence (2017) "Electron-Capture and Low-Mass Iron-Core-Collapse Supernovae: New Neutrino-Radiation-Hydrodynamics Simulations," *Astrophys. J.*, **850**(1), p. 43, 1702.03927.

[143] Fermi, E. (1949) "On the Origin of the Cosmic Radiation," *Phys. Rev.*, **75**, pp. 1169–1174.
URL https://link.aps.org/doi/10.1103/PhysRev.75.1169

[144] Blandford, R. and D. Eichler (1987) "Particle acceleration at astrophysical shocks: A theory of cosmic ray origin," *Phys. Rep*, **154**(1), pp. 1–75.

[145] Waxman, E. and J. N. Bahcall (1997) "High-energy neutrinos from cosmological gamma-ray burst fireballs," *Phys. Rev. Lett.*, **78**, pp. 2292–2295, astro-ph/9701231.

[146] Ahn, E.-J., R. Engel, T. K. Gaisser, P. Lipari, and T. Stanev (2009) "Cosmic ray interaction event generator SIBYLL 2.1," *Phys. Rev.*, **D80**, p. 094003, 0906.4113.

[147] Riehn, F., H. P. Dembinski, R. Engel, A. Fedynitch, T. K. Gaisser, and T. Stanev (2018) "The hadronic interaction model SIBYLL 2.3c and Feynman scaling," *PoS*, **ICRC2017**, p. 301, [35,301(2017)], 1709.07227.

[148] Riehn, F., R. Engel, A. Fedynitch, T. K. Gaisser, and T. Stanev (2019) "The hadronic interaction model Sibyll 2.3c and muon production in extensive air-showers," *EPJ Web Conf.*, **208**, p. 11002.

[149] Lipari, P. (1993) "Lepton spectra in the earth's atmosphere," *Astropart. Phys.*, **1**, pp. 195–227.

[150] Barr, G., T. K. Gaisser, and T. Stanev (1989) "Flux of Atmospheric Neutrinos," *Phys. Rev.*, **D39**, pp. 3532–3534.

[151] Gaisser, T. K., R. Engel, and E. Resconi (2016) *Cosmic Rays and Particle Physics*, Cambridge University Press.

[152] Longair, M. S. (2011) *High Energy Astrophysics*, 3 ed., Cambridge University Press.

[153] Narayan, R., B. Paczynski, and T. Piran (1992) "Gamma-ray bursts as the death throes of massive binary stars," *Astrophys. J. Lett.*, **395**, pp. L83–L86, astro-ph/9204001.

[154] Rees, M. J. and P. Meszaros (1994) "Unsteady outflow models for cosmological gamma-ray bursts," *Astrophys. J. Lett.*, **430**, pp. L93–L96, astro-ph/9404038.

[155] Blandford, R. D. and M. J. Rees (1974) "A "twin-exhaust" model for double radio sources." *MNRAS*, **169**, pp. 395–415.

[156] Begelman, M. C. and D. F. Cioffi (1989) "Overpressured Cocoons in Extragalactic Radio Sources," *The Astrophysical Journall*, **345**, p. L21.

[157] Mészáros, P. and E. Waxman (2001) "TeV Neutrinos from Successful and Choked Gamma-Ray Bursts," *Phys. Rev. Lett.*, **87**(17), 171102, astro-ph/0103275.

[158] Matzner, C. D. (2003) "Supernova hosts for gamma-ray burst jets: dynamical constraints," *MNRAS*, **345**(2), pp. 575–589, astro-ph/0203085.

[159] Lazzati, D. and M. C. Begelman (2005) "Universal GRB Jets from Jet-Cocoon Interaction in Massive Stars," *The Astrophysical Journal*, **629**(2), pp. 903–907, astro-ph/0502084.

[160] Bromberg, O., E. Nakar, T. Piran, and R. Sari (2011) "THE PROPAGATION OF RELATIVISTIC JETS IN EXTERNAL MEDIA," *Astrophys. J.*, **740**(2), p. 100.
URL https://doi.org/10.1088/0004-637x/740/2/100

[161] Aloy, M. A., E. Müller, J. M. Ibáñez, J. M. Martí, and A. MacFadyen (2000) "Relativistic Jets from Collapsars," *The Astrophysical Journall*, **531**(2), pp. L119–L122, astro-ph/9911098.

[162] Zhang, W., S. E. Woosley, and A. Heger (2004) "The Propagation and Eruption of Relativistic Jets from the Stellar Progenitors of Gamma-Ray Bursts," *The Astrophysical Journal*, **608**(1), pp. 365–377, astro-ph/0308389.

[163] Lazzati, D., B. J. Morsony, and M. C. Begelman (2009) "Very High Efficiency Photospheric Emission in Long-Duration γ-Ray Bursts," *The Astrophysical Journall*, **700**(1), pp. L47–L50, 0904.2779.

[164] Mizuta, A. and M. A. Aloy (2009) "Angular Energy Distribution of Collapsar-Jets," *The Astrophysical Journal*, **699**(2), pp. 1261–1273, 0812.4813.

[165] Nagakura, H., H. Ito, K. Kiuchi, and S. Yamada (2011) "Jet Propagations, Breakouts, and Photospheric Emissions in Collapsing Massive Progenitors of Long-duration Gamma-ray Bursts," *The Astrophysical Journal*, **731**(2), 80, 1009.2326.

[166] Harrison, R., O. Gottlieb, and E. Nakar (2018) "Numerically calibrated model for propagation of a relativistic unmagnetized jet in dense media," *MNRAS*, **477**(2), pp. 2128–2140, 1707.06234.

[167] Gottlieb, O., A. Levinson, and E. Nakar (2019) "High efficiency photospheric emission entailed by formation of a collimation shock in gamma-ray bursts," *MNRAS*, **488**(1), pp. 1416–1426, 1904.07244.

[168] Toma, K., K. Ioka, T. Sakamoto, and T. Nakamura (2007) "Low-Luminosity GRB 060218: A Collapsar Jet from a Neutron Star, Leaving a Magnetar as a Remnant?" *Astrophys. J.*, **659**, pp. 1420–1430, astro-ph/0610867.

[169] Liang, E., B. Zhang, and Z. G. Dai (2007) "Low Luminosity Gamma-Ray Bursts as a Unique Population: Luminosity Function, Local Rate, and Beaming Factor," *Astrophys. J.*, **662**, pp. 1111–1118, astro-ph/0605200.

[170] Gendre, B., G. Stratta, J. L. Atteia, S. Basa, M. Boër, D. M. Coward, S. Cutini, V. D'Elia, E. J. Howell, A. Klotz, and L. Piro (2013) "THE ULTRA-LONG GAMMA-RAY BURST 111209A: THE COLLAPSE OF A BLUE SUPERGIANT?" *Astrophys. J.*, **766**(1), p. 30.
URL https://doi.org/10.1088/0004-637x/766/1/30

[171] Levan, A. J. et al. (2013) "A new population of ultra-long duration gamma-ray bursts," *Astrophys. J.*, **781**, p. 13, 1302.2352.

[172] Aartsen, M. G. et al. (2015) "Search for Prompt Neutrino Emission from Gamma-Ray Bursts with IceCube," *Astrophys. J. Lett.*, **805**(1), p. L5, 1412.6510.

[173] ——— (2016) "An All-Sky Search for Three Flavors of Neutrinos from Gamma-Ray Bursts with the IceCube Neutrino Observatory," *Astrophys. J.*, **824**(2), p. 115, 1601.06484.

[174] Meszaros, P. and E. Waxman (2001) "TeV neutrinos from successful and choked gamma-ray bursts," *Phys. Rev. Lett.*, **87**, p. 171102, astro-ph/0103275.

[175] Woosley, S. and A. Heger (2006) "The Progenitor stars of gamma-ray bursts," *Astrophys. J.*, **637**, pp. 914–921, astro-ph/0508175.

[176] Kimura, S. S., K. Murase, I. Bartos, K. Ioka, I. S. Heng, and P. Mészáros (2018) "Transejecta high-energy neutrino emission from binary neutron star mergers," *Phys. Rev. D*, **98**(4), p. 043020, 1805.11613.

[177] Hamidani, H., K. Kiuchi, and K. Ioka (2020) "Jet Propagation in Neutron Star Mergers and GW170817," *Mon. Not. Roy. Astron. Soc.*, **491**(3), pp. 3192–3216, 1909.05867.

[178] Blandford, R. D. and R. L. Znajek (1977) "Electromagnetic extraction of energy from Kerr black holes," *Monthly Notices of the Royal Astronomical Society*, **179**(3), pp. 433–456, https://academic.oup.com/mnras/article-pdf/179/3/433/9333653/mnras179-0433.pdf.
URL https://doi.org/10.1093/mnras/179.3.433

[179] Kelner, S. R., F. A. Aharonian, and V. V. Bugayov (2006) "Energy spectra of gamma-rays, electrons and neutrinos produced at proton-proton interactions in the very high energy regime," *Phys. Rev. D*, **74**, p. 034018, [Erratum: Phys.Rev.D 79, 039901 (2009)], astro-ph/0606058.

[180] "NuFIT 2021, http://www.nu-fit.org/," .
URL http://www.nu-fit.org/

[181] Blum, K., Y. Nir, and E. Waxman (2007) "Probing CP violation in neutrino oscillations with neutrino telescopes," 0706.2070.

[182] Esmaili, A. and Y. Farzan (2009) "An Analysis of Cosmic Neutrinos: Flavor Composition at Source and Neutrino Mixing Parameters," *Nucl. Phys. B*, **821**, pp. 197–214, 0905.0259.

[183] Abe, K. et al. (2018) "Search for CP Violation in Neutrino and Antineutrino Oscillations by the T2K Experiment with 2.2×10^{21} Protons on Target," *Phys. Rev. Lett.*, **121**(17), p. 171802, 1807.07891.

[184] Argüelles Delgado, C. A., J. Salvado, and C. N. Weaver (2015) "A Simple Quantum Integro-Differential Solver (SQuIDS)," *Comput. Phys. Commun.*, **196**, pp. 569–591, 1412.3832.

[185] Xiao, D. and Z. G. Dai (2014) "Neutrino Emission in the Jet Propagation Process," *Astrophys. J.*, **790**(1), p. 59, 1406.2792.

[186] Kashti, T. and E. Waxman (2005) "Flavoring astrophysical neutrinos: Flavor ratios depend on energy," *Phys. Rev. Lett.*, **95**, p. 181101, astro-ph/0507599.

[187] Gandhi, R., C. Quigg, M. H. Reno, and I. Sarcevic (1996) "Ultrahigh-energy neutrino interactions," *Astropart. Phys.*, **5**, pp. 81–110, hep-ph/9512364.

[188] Murase, K., D. Guetta, and M. Ahlers (2016) "Hidden Cosmic-Ray Accelerators as an Origin of TeV-PeV Cosmic Neutrinos," *Phys. Rev. Lett.*, **116**(7), p. 071101, 1509.00805.

[189] Capanema, A., A. Esmaili, and K. Murase (2020) "New constraints on the origin of medium-energy neutrinos observed by IceCube," *Phys. Rev. D*, **101**(10), p. 103012, 2002.07192.

[190] He, H.-N., A. Kusenko, S. Nagataki, Y.-Z. Fan, and D.-M. Wei (2018) "Neutrinos from Choked Jets Accompanied by Type-II Supernovae," *Astrophys. J.*, **856**(2), p. 119, 1803.07478.

[191] Murase, K., S. S. Kimura, and P. Meszaros (2020) "Hidden Cores of Active Galactic Nuclei as the Origin of Medium-Energy Neutrinos: Critical Tests with the MeV Gamma-Ray Connection," *Phys. Rev. Lett.*, **125**(1), p. 011101, 1904.04226.

[192] Kimura, S. S., K. Murase, and K. Toma (2015) "Neutrino and Cosmic-Ray Emission and Cumulative Background from Radiatively Inefficient Accretion Flows in Low-Luminosity Active Galactic Nuclei," *Astrophys. J.*, **806**, p. 159, 1411.3588.

[193] Waxman, E. and J. N. Bahcall (1999) "High-energy neutrinos from astrophysical sources: An Upper bound," *Phys. Rev. D*, **59**, p. 023002, hep-ph/9807282.

[194] Murase, K. and E. Waxman (2016) "Constraining High-Energy Cosmic Neutrino Sources: Implications and Prospects," *Phys. Rev. D*, **94**(10), p. 103006, 1607.01601.

[195] Senno, N., K. Murase, and P. Meszaros (2017) "High-energy Neutrino Flares from X-Ray Bright and Dark Tidal Disruption Events," *Astrophys. J.*, **838**(1), p. 3, 1612.00918.

[196] Esmaili, A. and K. Murase (2018) "Constraining high-energy neutrinos from choked-jet supernovae with IceCube high-energy starting events," *JCAP*, **12**, p. 008, 1809.09610.

[197] Aartsen, M. G. et al. (2019) "Constraints on minute-scale transient astrophysical neutrino sources," *Phys. Rev. Lett.*, **122**(5), p. 051102, 1807.11492.

[198] Denton, P. B. and I. Tamborra (2018) "The Bright and Choked Gamma-Ray Burst Contribution to the IceCube and ANTARES Low-Energy Excess," *JCAP*, **04**, p. 058, 1802.10098.

[199] Senno, N., K. Murase, and P. Mészáros (2018) "Constraining high-energy neutrino emission from choked jets in stripped-envelope supernovae," *JCAP*, **01**, p. 025, 1706.02175.

[200] Harding, A. K. and D. Lai (2006) "Physics of Strongly Magnetized Neutron Stars," *Rept. Prog. Phys.*, **69**, p. 2631, astro-ph/0606674.

[201] Mereghetti, S. (2008) "The strongest cosmic magnets: Soft Gamma-ray Repeaters and Anomalous X-ray Pulsars," *Astron. Astrophys. Rev.*, **15**, pp. 225–287, 0804.0250.

[202] Kaspi, V. M. and A. Beloborodov (2017) "Magnetars," *Ann. Rev. Astron. Astrophys.*, **55**, pp. 261–301, 1703.00068.

[203] Duncan, R. C. and C. Thompson (1992) "Formation of very strongly magnetized neutron stars - implications for gamma-ray bursts," *Astrophys. J.*, **392**, p. L9.

[204] Thompson, C. and R. C. Duncan (1993) "Neutron star dynamos and the origins of pulsar magnetism," *Astrophys. J.*, **408**, p. 194.

[205] Ferrario, L. and D. Wickramasinghe (2006) "Modelling of isolated radio pulsars and magnetars on the fossil field hypothesis," *Mon. Not. Roy. Astron. Soc.*, **367**, p. 1323, astro-ph/0601258.

[206] Arons, J. (2003) "Magnetars in the metagalaxy: an origin for ultrahigh-energy cosmic rays in the nearby universe," *Astrophys. J.*, **589**, pp. 871–892, astro-ph/0208444.

[207] Murase, K., P. Meszaros, and B. Zhang (2009) "Probing the birth of fast rotating magnetars through high-energy neutrinos," *Phys. Rev.*, **D79**, p. 103001, 0904.2509.

[208] Kotera, K. (2011) "Ultrahigh energy cosmic ray acceleration in newly born magnetars and their associated gravitational wave signatures," *Phys. Rev. D*, **84**, p. 023002, 1106.3060.

[209] Fang, K., K. Kotera, K. Murase, and A. V. Olinto (2014) "Testing the Newborn Pulsar Origin of Ultrahigh Energy Cosmic Rays with EeV Neutrinos," *Phys. Rev.*, **D90**(10), p. 103005, [Erratum: Phys. Rev.D92,no.12,129901(2015); Phys. Rev.D90,103005(2014)], 1311.2044.

[210] ——— (2016) "IceCube Constraints on Fast-Spinning Pulsars as High-Energy Neutrino Sources," *JCAP*, **1604**(04), p. 010, 1511.08518.

[211] Fang, K. and B. D. Metzger (2017) "High-Energy Neutrinos from Millisecond Magnetars formed from the Merger of Binary Neutron Stars," *Astrophys. J.*, **849**(2), p. 153, 1707.04263.

[212] Enberg, R., M. H. Reno, and I. Sarcevic (2009) "High energy neutrinos from charm in astrophysical sources," *Phys. Rev. D*, **79**, p. 053006, 0808.2807.

[213] Bhattacharya, A., R. Enberg, M. H. Reno, and I. Sarcevic (2015) "Charm decay in slow-jet supernovae as the origin of the IceCube ultra-high energy neutrino events," *JCAP*, **06**, p. 034, 1407.2985.

[214] Olinto, A. V. et al. (2018) "POEMMA: Probe Of Extreme Multi-Messenger Astrophysics," *PoS*, **ICRC2017**, p. 542, [35,542(2017)], 1708.07599.

[215] Gruzinov, A. (2005) "The Power of axisymmetric pulsar," *Phys. Rev. Lett.*, **94**, p. 021101, astro-ph/0407279.

[216] Spitkovsky, A. (2006) "Time-dependent force-free pulsar magnetospheres: axisymmetric and oblique rotators," *Astrophys. J.*, **648**, pp. L51–L54, astro-ph/0603147.

[217] Tchekhovskoy, A., A. Spitkovsky, and J. G. Li (2013) "Time-dependent 3D magnetohydrodynamic pulsar magnetospheres: oblique rotators," *Monthly Notices of the Royal Astronomical Society: Letters*, **435**(1), pp. L1–L5, https://academic.oup.com/mnrasl/article-pdf/435/1/L1/3823710/slt076.pdf. URL https://doi.org/10.1093/mnrasl/slt076

[218] Murase, K., K. Kashiyama, and P. Mészáros (2016) "A Burst in a Wind Bubble and the Impact on Baryonic Ejecta: High-Energy Gamma-Ray Flashes and Afterglows from Fast Radio Bursts and Pulsar-Driven Supernova Remnants," *Mon. Not. Roy. Astron. Soc.*, **461**(2), pp. 1498–1511, [Erratum: Mon.Not.Roy.Astron.Soc. 467, 3542–3543 (2017)], 1603.08875.

[219] Goldreich, P. and W. H. Julian (1969) "Pulsar electrodynamics," *Astrophys. J.*, **157**, p. 869.

[220] Heger, A., S. Woosley, and H. Spruit (2005) "Presupernova evolution of differentially rotating massive stars including magnetic fields," *Astrophys. J.*, **626**, pp. 350–363, astro-ph/0409422.

[221] Wu, M.-R., R. Fernández, G. Martínez-Pinedo, and B. D. Metzger (2016) "Production of the entire range of r-process nuclides by black hole accretion disc outflows from neutron star mergers," *Mon. Not. Roy. Astron. Soc.*, **463**(3), pp. 2323–2334, 1607.05290.

[222] Bhattacharya, A., R. Enberg, M. H. Reno, I. Sarcevic, and A. Stasto (2015) "Perturbative charm production and the prompt atmospheric neutrino flux in light of RHIC and LHC," *JHEP*, **06**, p. 110, 1502.01076.

[223] Bhattacharya, A., R. Enberg, Y. S. Jeong, C. S. Kim, M. H. Reno, I. Sarcevic, and A. Stasto (2016) "Prompt atmospheric neutrino fluxes: perturbative QCD models and nuclear effects," *JHEP*, **11**, p. 167, 1607.00193.

[224] Nason, P., S. Dawson, and R. K. Ellis (1988) "The Total Cross-Section for the Production of Heavy Quarks in Hadronic Collisions," *Nucl.Phys.*, **B303**, p. 607.

[225] ——— (1989) "The One Particle Inclusive Differential Cross-Section for Heavy Quark Production in Hadronic Collisions," *Nucl.Phys.*, **B327**, pp. 49–92.

[226] Mangano, M. L., P. Nason, and G. Ridolfi (1992) "Heavy quark correlations in hadron collisions at next-to-leading order," *Nucl.Phys.*, **B373**, pp. 295–345.

[227] Catani, S., M. Ciafaloni, and F. Hautmann (1991) "High-energy factorization and small x heavy flavor production," *Nucl. Phys.*, **B366**, pp. 135–188.

[228] Collins, J. C. and R. K. Ellis (1991) "Heavy quark production in very high-energy hadron collisions," *Nucl. Phys.*, **B360**, pp. 3–30.

[229] Levin, E. M., M. G. Ryskin, Yu. M. Shabelski, and A. G. Shuvaev (1991) "Heavy quark production in parton model and in QCD," *Sov. J. Nucl. Phys.*, **54**, pp. 867–871, [Yad. Fiz.54,1420(1991)].

[230] Ryskin, M. G., Yu. M. Shabelski, and A. G. Shuvaev (1996) "Heavy quark production in parton model and in QCD," *Z. Phys.*, **C69**, pp. 269–276, [Yad. Fiz.59,521(1996); Phys. Atom. Nucl.59,493(1996)], hep-ph/9506338.

[231] Gribov, L., E. Levin, and M. Ryskin (1983) "Semihard Processes in QCD," *Phys. Rept.*, **100**, pp. 1–150.

[232] Madau, P. and M. Dickinson (2014) "Cosmic Star Formation History," *Ann. Rev. Astron. Astrophys.*, **52**, pp. 415–486, 1403.0007.

[233] Kotera, K., E. S. Phinney, and A. V. Olinto (2013) "Signatures of pulsars in the light curves of newly formed supernova remnants," *Mon. Not. Roy. Astron. Soc.*, **432**, pp. 3228–3236, 1304.5326.

[234] Murase, K., K. Kashiyama, K. Kiuchi, and I. Bartos (2015) "Gamma-Ray and Hard X-Ray Emission from Pulsar-Aided Supernovae as a Probe of Particle Acceleration in Embryonic Pulsar Wind Nebulae," *Astrophys. J.*, **805**(1), p. 82, 1411.0619.

[235] Kashiyama, K., K. Murase, I. Bartos, K. Kiuchi, and R. Margutti (2016) "Multi-Messenger Tests for Fast-Spinning Newborn Pulsars Embedded in Stripped-Envelope Supernovae," *Astrophys. J.*, **818**(1), p. 94, 1508.04393.

[236] Murase, K., B. Dasgupta, and T. A. Thompson (2014) "Quasithermal Neutrinos from Rotating Protoneutron Stars Born during Core Collapse of Massive Stars," *Phys. Rev. D*, **89**(4), p. 043012, 1303.2612.

[237] Bartos, I., P. Brady, and S. Marka (2013) "How Gravitational-wave Observations Can Shape the Gamma-ray Burst Paradigm," *Class. Quant. Grav.*, **30**, p. 123001, 1212.2289.

[238] Riess, A. G. et al. (2022) "A Comprehensive Measurement of the Local Value of the Hubble Constant with 1 km/s/Mpc Uncertainty from the Hubble Space Telescope and the SH0ES Team," *Astrophys. J. Lett.*, **934**(1), p. L7, 2112.04510.

[239] Bashinsky, S. and U. Seljak (2004) "Neutrino perturbations in CMB anisotropy and matter clustering," *Phys. Rev. D*, **69**, p. 083002, astro-ph/0310198.

[240] Long, A. J., C. Lunardini, and E. Sabancilar (2014) "Detecting non-relativistic cosmic neutrinos by capture on tritium: phenomenology and physics potential," *JCAP*, **08**, p. 038, 1405.7654.

[241] Williamson, I. P. (1972) "Pulse Broadening due to Multiple Scattering in the Interstellar Medium," *Monthly Notices of the Royal Astronomical Society*, **157**(1), pp. 55–71, https://academic.oup.com/mnras/article-pdf/157/1/55/8079321/mnras157-0055.pdf.
URL https://doi.org/10.1093/mnras/157.1.55

[242] Alcock, C. and S. Hatchett (1978) "The effect of small-angle scattering on a pulse of radiation with an application of X-ray bursts and interstellar dust." *Ap. J.*, **222**, pp. 456–470.

[243] Eskenasy, R., A. Kheirandish, and K. Murase (2023) "Light curves of BSM-induced neutrino echoes in the optically thin limit," *Phys. Rev. D*, **107**(10), p. 103038, 2204.08924.

[244] Yoshida, S. (1994) "Propagation of ultrahigh energy neutrinos in the black-body neutrino field," *Astroparticle Physics*, **2**(2), pp. 187–198.
URL https://www.sciencedirect.com/science/article/pii/0927650594900418

[245] Koren, S. (2019) "Neutrino – Dark Matter Scattering and Coincident Detections of UHE Neutrinos with EM Sources," *JCAP*, **09**, p. 013, 1903.05096.

[246] Araki, T., F. Kaneko, Y. Konishi, T. Ota, J. Sato, and T. Shimomura (2015) "Cosmic neutrino spectrum and the muon anomalous magnetic moment in the gauged $L_\mu - L_\tau$ model," *Phys. Rev. D*, **91**(3), p. 037301, 1409.4180.

[247] Araki, T., K. Asai, K. Honda, R. Kasuya, J. Sato, T. Shimomura, and M. J. S. Yang (2021) "Resolving the Hubble tension in a $\mathrm{U}(1)_{L_\mu - L_\tau}$ model with the Majoron," *PTEP*, **2021**(10), p. 103B05, 2103.07167.

[248] Duerr, M., K. Schmidt-Hoberg, and S. Wild (2018) "Self-interacting dark matter with a stable vector mediator," *JCAP*, **09**, p. 033, 1804.10385.

[249] Arcadi, G., A. Djouadi, and M. Kado (2021) "The Higgs-portal for dark matter: effective field theories versus concrete realizations," *Eur. Phys. J. C*, **81**(7), p. 653, 2101.02507.

[250] Holz, D. E. and A. Zee (2001) "Collisional dark matter and scalar phantoms," *Phys. Lett. B*, **517**, pp. 239–242, hep-ph/0105284.

[251] Mirizzi, A., I. Tamborra, H.-T. Janka, N. Saviano, K. Scholberg, R. Bollig, L. Hudepohl, and S. Chakraborty (2016) "Supernova Neutrinos: Production, Oscillations and Detection," *Riv. Nuovo Cim.*, **39**(1-2), pp. 1–112, 1508.00785.

[252] Lunardini, C. (2015) "Theory and phenomenology of supernova neutrinos," *AIP Conference Proceedings*, **1666**(1), p. 070001, https://aip.scitation.org/doi/pdf/10.1063/1.4915560.
URL https://aip.scitation.org/doi/abs/10.1063/1.4915560

[253] Nakazato, K., K. Sumiyoshi, H. Suzuki, T. Totani, H. Umeda, and S. Yamada (2013) "Supernova Neutrino Light Curves and Spectra for Various Progenitor Stars: From Core Collapse to Proto-neutron Star Cooling," *Astrophys. J. Suppl.*, **205**, p. 2, 1210.6841.

[254] Tamborra, I., G. Raffelt, F. Hanke, H.-T. Janka, and B. Mueller (2014) "Neutrino emission characteristics and detection opportunities based on three-dimensional supernova simulations," *Phys. Rev. D*, **90**(4), p. 045032, 1406.0006.

[255] Blum, K. and D. Kushnir (2016) "Neutrino Signal of Collapse-induced Thermonuclear Supernovae: the Case for Prompt Black Hole Formation in SN1987A," *Astrophys. J.*, **828**(1), p. 31, 1601.03422.

[256] Perego, A., M. Hempel, K. Ebinger, M. Eichler, M. Liebendörfer, F. K. Thielemann, C. Fröhlich, and E.-m. c. Casanova, J. (2015) "Pushing core-collapse supernovae to explosions in spherical symmetry. I. The model and the case of SN 1987A," *Astrophysical Journal*, **806**(2).
URL https://www.osti.gov/biblio/22883000

[257] Suwa, Y., A. Harada, K. Nakazato, and K. Sumiyoshi (2021) "Analytic solutions for neutrino-light curves of core-collapse supernovae," *PTEP*, **2021**(1), p. 013E01, 2008.07070.

[258] Abe, K. et al. (2021) "Supernova Model Discrimination with Hyper-Kamiokande," *Astrophys. J.*, **916**(1), p. 15, 2101.05269.

[259] Dighe, A. S. and A. Y. Smirnov (2000) "Identifying the neutrino mass spectrum from the neutrino burst from a supernova," *Phys. Rev. D*, **62**, p. 033007, hep-ph/9907423.

[260] Feldman, G. J. and R. D. Cousins (1998) "A Unified approach to the classical statistical analysis of small signals," *Phys. Rev. D*, **57**, pp. 3873–3889, physics/9711021.

[261] Lin, Z. and C. Lunardini (2020) "Observing cosmological binary mergers with next generation neutrino and gravitational wave detectors," *Phys. Rev. D*, **101**(2), p. 023016, 1907.00034.

[262] Tulin, S., H.-B. Yu, and K. M. Zurek (2013) "Resonant Dark Forces and Small Scale Structure," *Phys. Rev. Lett.*, **110**(11), p. 111301, 1210.0900.

[263] ——— (2013) "Beyond Collisionless Dark Matter: Particle Physics Dynamics for Dark Matter Halo Structure," *Phys. Rev. D*, **87**(11), p. 115007, 1302.3898.

[264] Berlin, A. and N. Blinov (2018) "Thermal Dark Matter Below an MeV," *Phys. Rev. Lett.*, **120**(2), p. 021801, 1706.07046.

[265] Murase, K. and J. F. Beacom (2012) "Constraining Very Heavy Dark Matter Using Diffuse Backgrounds of Neutrinos and Cascaded Gamma Rays," *JCAP*, **10**, p. 043, 1206.2595.

[266] Martin, A. D., M. G. Ryskin, and A. M. Stasto (2003) "Prompt neutrinos from atmospheric $c\bar{c}$ and $b\bar{b}$ production and the gluon at very small x," *Acta Phys. Polon. B*, **34**, pp. 3273–3304, hep-ph/0302140.

[267] Kutak, K. and J. Kwiecinski (2003) "Screening effects in the ultrahigh-energy neutrino interactions," *Eur. Phys. J. C*, **29**, p. 521, hep-ph/0303209.

[268] Kutak, K. and S. Sapeta (2012) "Gluon saturation in dijet production in p-Pb collisions at Large Hadron Collider," *Phys. Rev. D*, **86**, p. 094043, 1205.5035.

[269] Pietschmann, H. (1984) *WEAK INTERACTIONS - FORMULAE, RESULTS AND DERIVATIONS*.

Vita

Jose Alonso Carpio Dumler

Education

- B. Sc. in Physics, 2013, Pontificia Universidad Católica del Perú
- M. Sc. in Physics, 2016, Pontificia Universidad Católica del Perú
- PhD in Physics, August 2023, The Pennsylvania State University

Selected Publications

- **J.A. Carpio** and K. Murase, Oscillation of high-energy neutrinos from choked jets in stellar and merger ejecta, Phys. Rev. D 101, 123002 (2020).
- **J.A. Carpio**, K. Murase, M.H. Reno, I. Sarcevic and A. Stasto, Charm contribution to ultrahigh-energy neutrinos from newborn magnetars, Phys. Rev. D 102, 103001 (2020).
- **J.A. Carpio**, K. Murase, I. Shoemaker and Z. Tabrizi, High-energy cosmic neutrinos as a probe of the vector mediator scenario in light of the muon g-2 anomaly and Hubble tension, Phys. Rev. D 107, 103057 (2023).
- **J.A. Carpio** and K. Murase, Simulating neutrino echoes induced by secret neutrino interactions, JCAP 02, 042 (2023).
- **J.A. Carpio**, A. Kheirandish and K. Murase, Time-delayed neutrino emission from supernovae as a probe of dark matter-neutrino interactions, JCAP 04, 019 (2023).
- S. Abbar, **J.A. Carpio** and K. Murase, Oscillations of high-energy cosmic neutrinos in the copious MeV background, arXiv:2205.10384.
- M. Bhattacharya, **J.A. Carpio**, K. Murase and S. Horiuchi, High-energy neutrino emission from magnetised jets of rapidly rotating protomagnetars, MNRAS 521, 2391 (2023).